Microscopic structure-property relationships in semiconductor devices

Correlative microscopy at the example of $Cu(In,Ga)Se_2$ thin-film solar cells

Dr. sc. nat. Daniel Abou-Ras

Habilitationsschrift an der
Fakultät II für Mathematik und Naturwissenschaften
der Technischen Universität Berlin

Lehrgebiet: Physik

Eröffnung des Verfahrens: 01.10.2014
Habilitationsvortrag: 28.04.2015
Verleihung der Lehrbefähigung: 19.05.2015

Gutachter:
Prof. Dr. Michael Lehmann
Prof. Christoph T. Koch, Ph.D.
Prof. Oded Millo, Ph.D.
Prof. Dr. Uwe Rau
Prof. Dr. Susanne Siebentritt

Berlin, 2015

für Cíntia, Rafael, Teresa und Gabriel

Acknowledgements

In the following, I would like to acknowledge all those persons who helped me to finish the present habilitation work successfully.
First of all, I would like to thank Prof. Dr. Michael Lehmann for accepting me as candidate for habilitation at the TU Berlin. Various discussions with him helped substantially to shape the present work and to clarify diverse scientific aspects. I am also indebted to Prof. Dr. Wolfgang Eberhardt, Prof. Dr. Birgit Kanngiesser, and Prof. Dr. Christian Boit, all TU Berlin, for supporting my candidateship.

I would like to thank also the following persons:

- Prof. Dr.-Ing. Hans-Werner Schock (HZB) for continuous support during many years, also with respect to the habilitation
- Prof. Dr. Silke Christiansen (MPL/HZB) for continuous support
- Dr. Thomas Unold (HZB) for continuous support as well as numerous discussions
- My colleagues from the former Department/Institute for Technology at HMI/HZB for solar-cell production, help with the experimental setups, and numerous discussions
- My colleagues from the Institute for Nanoarchitectures for Energy Conversion at HZB for help with the experimental setups, specimen preparation for electron microscopy, and numerous discussions
- Of these colleagues particularly my doctoral, diploma, and master students Nilay Baldaz, Jens Dietrich, Jaison Kavalakkatt, Melanie Nichterwitz, Norbert Schäfer, and Sebastian S. Schmidt, who contributed substantially to the content of the present work
- The collaborations with various colleagues from TU Berlin, FU Berlin, Paul-Drude Institute for Solid-State Electronics (Berlin), BAM Berlin, PTB Berlin, TU Darmstadt, ZSW Stuttgart, MPI for Intelligent Systems (Stuttgart), MPI for Iron Research (Düsseldorf), University of Magdeburg, University of Jena, University of Ulm, ESRF (Grenoble, France), SuperSTEM (Daresbury, UK), University of Oxford (UK), Hebrew University (Jerusalem, Israel), Weizmann Institute of Science (Rehovot, Israel), Tel Aviv Technical University (Israel), NREL (Golden, CO, USA), University of Toledo (OH, USA), AIST (Tsukuba, Japan), as well as the following industrial partners: HKL / Oxford Instruments, Carl Zeiss Microscopy, and BLG Productions
- The project ProGraB (financed by BMU/MOST) and the Helmholtz Virtual Institute "Microstructure Control for Thin-Film Solar Cells"

Finally, I would like to thank my parents for their support, and particularly my wife Cíntia as well as my children Rafael, Teresa, and Gabriel for everything they give to me.

Contents

Abbreviations and symbols

AES	Auger electron spectrometry
AFM	Atomic force microscopy
AM	Air mass
APT	Atom-probe tomography
b	Optical bowing factor
B	Material-specific radiation coefficient
BF	Bright field
c	Velocity of light
c-AFM	Conductive atomic force microscopy
C	Capacitance
CGI	[Cu]/([Ga]+[In]) ratio
CL	Cathodoluminescence
CPD	Contact-potential difference
CSL	Coincidence-site lattice
d_0	Interplanar distance for unstrained atomic lattice
d_{strain}	Interplanar distance for strained atomic lattice
D	Diffusion constant
DFT	Density-functional theory
e	Elemental charge
E	Energy
E_{b}	Electron-beam energy
E_{gap}	Band-gap energy
$\overline{E}_{\mathrm{gap}}$	average band-gap energy
E_{ph}	Photon energy
EBSD	Electron backscatter diffraction
EBIC	Electron-beam-induced current
EDX	Energy-dispersive X-ray spectrometry
EDXRD	Energy-dispersive X-ray diffraction
EDXRF	Energy-dispersive X-ray fluorescence analysis
EELS	Electron energy-loss spectrometry
ESRF	European Synchrotron Radiation Facility
$f_j^{\mathrm{el}}(0)$	Atomic and ionic scattering factors in forward direction
FIB	Focused-ion beam

FF	Fill factor
FT	Fourier transform
FWHM	Full width at half maximum
g	Generation profile
GGI	[Ga]/([Ga]+[In]) ratio
GB	Grain boundary
h	Planck's constant
HAADF	High-angle annular dark-field
HR	High-resolution
HZB	Helmholtz-Zentrum Berlin für Materialien und Energie
I	Intensity
I_b	Electron-beam current
I_EBIC	Electron-beam-induced current
j	Current density
j_MPP	Current density at maximum-power point
j_sc	Short-circuit current density
$j_\mathrm{sc,SQ}$	Short-circuit current density at the Shockley-Queisser limit
j_0	Dark saturation current density
$j_\mathrm{0,rad}$	Radiative part of dark saturation current density
$j_\mathrm{0,nrad}$	Nonradiative part of dark saturation current density
j_0	Dark saturation current density
k_B	Boltzmann constant
K	Thermal conductivity
K_0	Modified Bessel function
KPFM	Kelvin-probe force microscopy
L	Diffusion length
L_Debye	Debye length
LED	Light-emitting diode
m_e	Effective mass of electrons
MIP	Mean-inner potental
MPP	Maximum-power point
n	Density of electrons
n_i	Intrinsic charge-carrier density
n_j	Number of atoms or ions of type j
n_id	Diode-ideality factor
N_A	Acceptor density
NREL	National Renewable Energy Laboratory
p	Density of holes
p_in	Power density of incident light
q	Charge
q_L	Line charge of dislocation core
Q_e	External quantum efficiency
Q_i	Internal quantum efficiency
Q_LED	Quantum efficiency of a light-emitting diode
r	Space coordinate

r_b	Electron-beam radius
R	Reflectance
R_Auger	Auger recombination rate
R_rad	Radiative recombination rate
R_SRH	Shockley-Read-Hall recombination rate
S_GB	Recombination velocity at grain boundary
S_Mo	Recombination velocity at Mo back contact
S_SF	Recombination velocity at surface
SAEM	Scanning Auger electron microscopy
SCAPS	Solar Cell Capacitance Simulator
SCM	Scanning capacitance microscopy
SCR	Space-charge region
SE	Secondary electron
SEM	Scanning electron microscopy
SNOM	Scanning near-field optical microscopy
SPM	Scanning probe microscopy
SQ	Shockley-Queisser
SRH	Shockley-Read-Hall
SSPM	Scanning surface potential microscopy
STEM	Scanning transmission electron microscopy
STM	Scanning tunneling microscopy
STS	Scanning tunneling spectrosocpy
t	Thickness
T	Absolute temperature
TB	Twin boundary
TEM	Transmission electron microscopy
TU	Technische Universität (technical university)
V	Voltage, potental difference
V_a, V_av	Averaged, electrostatic potential
V_MPP	Voltage at maximum-power point
V_oc	Open-circuit voltage
$V_\mathrm{oc,rad}$	Radiative part open-circuit voltage
VBM	Valence-band maximum
x_Mo	Position of Mo back contact
x_SCR	Position of edge of space-charge region
Y	Young's modulus
ZSW	Zentrum für Sonnerenergie- und Wasserstoffforschung
Γ_n	Auger coefficient for electrons
Γ_p	Auger coefficient for holes
δ	Delta function
Δf	Defocus
ϵ, ϵ_{ij}	Tensor for mechanical strain
ϵ_0	Vacuum permittivity
ϵ_r	Relative permittivity
η	Power-conversion efficiency

λ_{inel}	Inelastic mean-free path
σ, σ_{ij}	Tensor for mechanical stress
$\sigma_{E_{\mathrm{el}}}$	Standard deviation of electrostatic fluctuation
$\sigma_{E_{\mathrm{gap}}}$	Standard deviation of band-gap fluctuation
$\sigma_{E_{\mathrm{total}}}$	Total fluctuations in semiconductor absorbers
σ_{U}	Interaction constant depending on aceleration voltage U
τ	Charge-carrier life time
ϕ	Phase; collection function
ϕ_{bb}	Photon flux from black body
ϕ_{el}	Electroluminescence
ϕ_{sun}	Photon flux from sun
Ω	Volume of unit cell

Chapter 1

Introduction

The issue of relating microstructural properties of materials to the functions of corresponding applications is a very old discipline in materials physics. Whenever designing materials for specific applications, it is essential to control the formation and properties of extended structural defects in the materials. In the investigation of such structure-property relationships, always microscopy techniques have been applied, in combination with mechanical or electrical characterization of the materials and corresponding devices. While in the beginning, rather optical microscopy was used, nowadays, also tunnelling, probe and electron microscopy techniques are employed.

The present work will deal with combinations of these microscope techniques in order to reveal structure-property relationships in optoelectronic devices such as solar cells as well as light-emitting and laser diodes based on inorganic semiconductor *p*-*n* junctions. More specifically, the focus will be put on the application of electron microscopy and its related methods. Since these methods are well suitable to study extended structural defects but not necessarily point defects, these zero-dimensional crystal defects will not be included in the characterization. However, it will be shown in the present work that point defects tend to segregate to extended structural defects. Therefore, it is not possible to separate point defects completely from extended structural defects.

Structure-property relationships in solar cells and light-emitting diodes have been studied by means of electron microscopy and its related techniques to large extent during the past decades (see various books as, e.g., Refs. [1–3], and also articles as, e.g., Refs. [4–10]), however, mostly in polycrystalline material systems with average grain sizes of several hundred micrometers. The present work deals with thin-film stacks, as applied for thin-film solar cells or light-emitting diodes, of only few micrometers in total thickness, in which the individual compound semiconductor layers exhibit average grain sizes of few hundred nanometers or even smaller. Such a situation requires not just the simple application of electron microscopy techniques described in the literature but their adaptation for the much smaller scales and the complex material systems, which also again make high demands on the specimen preparation for the analysis.

Extended structural defects have been investigated by numerous groups also down to the nanoscale or even at the subnanometer level. However, the key issue of revealing structure-property relationships in nanostructured material systems is the combined application of various microscopy techniques, probing microstructural, compositional, and optoelectronic properties of extended structural defects, on identical specimen positions. Such a work has not yet been performed to large extent, especially not

on nanostructured, optoelectric semiconductor devices. For such materials systems and devices, the present report intends to give a comprehensive overview and further development of corresponding approaches.

As an exemplary material system consisting of a thin-film stack, solar cells based on Cu(In,Ga)Se_2 absorber layers will be used. These solar cells are highly relevant since they exhibit the highest power-conversion efficiencies of all thin-film solar cells of up to 21% [11–14]. Note that thin-film solar cells are defined such that they are grown on just any substrate, without the necessity of epitaxial growth. Thus, all layers in the thin-film stack are polycrystalline. Currently, the research and development of Cu(In,Ga)Se_2 solar cells is based on trial-and-error approaches, aiming at achieving highest power-conversion efficiency without regarding the aspect of microstructure. The influences of extended structural defects in the polycrystalline Cu(In,Ga)Se_2 thin films on the device performances of the solar cells has not been fully understood. Indeed, only limited results are available in the literature, and knowledge on the microstructural development during film synthesis is insufficient for controlled and reproducible growth of the functional layers in the solar-cell stack. In view of the solar-cell performance limited mainly by the open-circuit voltage and thus by recombination of generated charge carriers, there is a great demand for enhanced understanding of structure-property relationships and thus for a basis of a controlled synthesis of Cu(In,Ga)Se_2 thin films for highest power-conversion efficiencies, towards 25% and larger.

In the present work, the direct link between extended structural defects and the macroscopic solar-cell performance can not yet be shown for both, the photocurrent and the photovoltage. While the microscropic behavior of the short-circuit current around these defects is consistent with a macroscopic photocurrent value close to the radiative limit of the solar cell, it remains a challenge to demonstrate a relationship between local recombination behaviors at extended structural defects and the limited open-circuit voltage, as a direct evidence that this limitation is mainly due to non-radiative recombination enhanced at the defects. Moreover, the local electrical and optoelectronic properties of these defects in Cu(In,Ga)Se_2 thin films differ substantially even within the same identical layer, as will be discussed in detail further below. From this complex ensemble of structural defects with different effects on current and voltage, it was not possible to derive consistent electronic band diagrams and to eventually propose an equally consistent device model including all structural defects. Thus, the issue of structure-property relationships has been considered mainly on the microscopic scale, and the present work gives a broad overview of these relationships for the various extended structural defects, as obtained by (mainly) electron microscopy techniques. The approaches detailed below can be used for the study of structure-property relationships also on other (complex) optoelectronic material systems and devices consisting of thin-film stacks built up by compound semiconductor layers.

The present work is organized in the following way. An introduction to optoelectronic semiconductor devices and structure-property relationships is provided in Chapter 2. Chapter 3 will give an overview of the different types of extended structural defects. An introduction into techniques used for the analysis of structure-property relationships in optoelectronic compound semiconductor devices can be found in Chapter 4. In the main Chapter 5 of the present work, the various properties of the different types of extended structural defects in Cu(In,Ga)Se_2 thin-film solar cells as well as their influences on the microscopic electrical and optoelectronic properties will be presented and discussed. Chapter 6 will conclude the work with an outlook.

Chapter 2

Structure-property relationships of optoelectronic semiconductor devices

In the present chapter, an overview on performance parameters of optoelectronic devices, i.e., solar cells and light-emitting diodes is given. Also, the limits of these devices are discussed, with an overview of the various factors reducing the device perfomance. Particularly, the relationship between recombination of generated charge carriers and extended structural defects is outlined.

2.1 Performance parameters of optoelectronic devices

A solar cell is a device that converts the power density of photons impinging on the device into electrical power density, i.e., into the product of a voltage and a current density. Fig. 2.1 gives a schematics of a solar cell as well as its current-voltage characteristics measured in darkness and under illumination.

The power conversion efficiency η of a solar cell is defined as $\eta = p_{\mathrm{max}}/p_{\mathrm{in}} = V_{\mathrm{MPP}} j_{\mathrm{MPP}}/p_{\mathrm{in}}$, where p_{max} is the maximum power density of the solar cells, V_{MPP} and j_{MPP} the voltage and current density at the maximum-power point, and p_{in} the power density of the impinging photon flux. Introducing the fill factor

$$FF = \frac{V_{\mathrm{MPP}} j_{\mathrm{MPP}}}{V_{\mathrm{oc}} j_{\mathrm{sc}}}, \tag{2.1}$$

where V_{oc} and j_{sc} are open-circuit voltage and short-circuit current density, the power-conversion efficiency can be written as

$$\eta = \frac{V_{\mathrm{oc}} j_{\mathrm{sc}} FF}{p_{\mathrm{in}}}. \tag{2.2}$$

The current-voltage dependence [16] of a solar cell with single p-n junction under illumination is expressed by

$$j(V) = j_0 \left[\exp\left(\frac{qV}{n_{\mathrm{id}} k_{\mathrm{B}} T} \right) - 1 \right] - j_{\mathrm{sc}}, \tag{2.3}$$

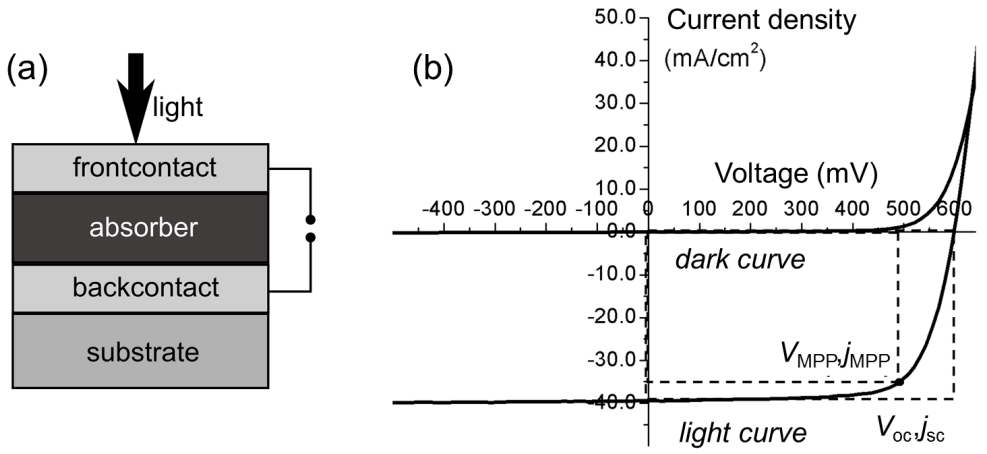

Figure 2.1: (a) Schematics of the layer sequences in a thin-film solar cell, adapted from Ref. [15]. (b) Current density-voltage characteristics of a high-efficient Cu(In,Ga)Se_2 solar cell, measured in darkness and under illumination. The dark and light characteristics overlap owing to a change in the saturation current under illumination. Various solar-cell parameters are given (see also the text for details).

where j_0 is the saturation current density, q is the charge, V the voltage, n_{id} the diode ideality factor (that corrects for small deviations of the exponential slope of $q/k_{\mathrm{B}}T$), k_{B} the Boltzmann constant, and T the absolute temperature. It is important to note that Eq. 2.3 represents an idealized description of the current density/voltage dependence of a solar cell since serial as well as shunt resistances are neglected. Also, the short-circuit current density j_{sc} is only equal to the photocurrent j_{ph} obtained by j-V measurements if j_{ph} is not voltage-dependent.

The current density introduced into the solar cell upon illumination is represented by the short-circuit current density j_{sc} (second part of Eq. 2.3). The dark current density of the solar cell (first part of Eq. 2.3) can be considered a recombination current density of charge carriers injected by applying a bias voltage. This recombination process may be radiative and also nonradiative. The saturation current density can therefore be regarded as the sum of radiative and nonradiative partial currents: $j_0 = j_{0,\mathrm{rad}} + j_{0,\mathrm{nrad}}$. The radiative part of the saturation current can be expressed in terms of Planck's radiation law, assuming the solar cell a black body (bb) emitting light, as a result of radiative recombination of generated charge-carriers by photons with energies of larger than the band-gap energy E_{gap}:

$$j_{0,\mathrm{rad}}(E_{\mathrm{gap}}) = q \int_{E_{\mathrm{gap}}}^{\infty} \phi_{\mathrm{bb}}(E)dE \tag{2.4}$$

with photon flux from a black body (per s and m^2) [17]

$$\phi_{\mathrm{bb}}(E_{\mathrm{ph}}) = \frac{2\pi}{h^3c^2} \frac{E_{\mathrm{ph}}^2}{\exp\left[E_{\mathrm{ph}}/(k_{\mathrm{B}}T)\right] - 1},$$

where h is Planck's constant and c the velocity of light. At $V \neq 0$, Eq. 2.4 changes

slightly to [18]

$$j_{0,\mathrm{rad}} = q\frac{2\pi}{h^3c^2}\int\limits_{E_{\mathrm{gap}}}^{\infty}\frac{E^2}{\exp\left[(E-eV)/(k_{\mathrm{B}}T)\right]-1}dE$$

For $V = V_{\mathrm{oc}}$, Eq. 2.3 can be written as:

$$V_{\mathrm{oc}} = \frac{n_{\mathrm{id}}k_{\mathrm{B}}T}{q}\ln\left(\frac{j_{\mathrm{sc}}}{j_0}+1\right). \tag{2.5}$$

This means, the saturation current density j_0, representing the recombination of injected charge carriers at bias voltage, is inversely proportional to the open-circuit voltage of the solar cell. The higher j_0, the lower V_{oc}.

The external quantum efficiency $Q_{\mathrm{e}}(E_{\mathrm{ph}})$ of a solar cell is defined as

$$Q_{\mathrm{e}}(E_{\mathrm{ph}}) = \frac{1}{q}\frac{\mathrm{d}j_{\mathrm{sc}}(E_{\mathrm{ph}})}{\mathrm{d}\phi_{\mathrm{sun}}(E_{\mathrm{ph}})}, \tag{2.6}$$

where E_{ph} is the photon energy, q the charge, and $\phi_{\mathrm{sun}}(E_{\mathrm{ph}})$ the flux of photons from the sun in $\mathrm{s}^{-1}\ \mathrm{m}^{-2}\ \mathrm{eV}^{-1}$. The internal quantum efficiency $Q_{\mathrm{i}}(E_{\mathrm{ph}})$ also takes into account the reflectance $R(E_{\mathrm{ph}})$:

$$Q_{\mathrm{i}}(E_{\mathrm{ph}}) = \frac{Q_{\mathrm{e}}(E_{\mathrm{ph}})}{(1-R(E_{\mathrm{ph}}))}.$$

Using Eq. 2.6, the short-circuit current density can be expressed as

$$j_{\mathrm{sc}} = q\int\limits_{E_{\mathrm{gap}}}^{\infty}Q_{\mathrm{e}}(E)\phi_{\mathrm{sun}}(E)dE \tag{2.7}$$

Solar cells are closely related to light-emitting diodes (LEDs) since the quantum efficiency Q_{e} of a solar cell is a process reciprocal to the electroluminescence ϕ_{el} of a LED [19]. The corresponding relationship can be written as [19]

$$\phi_{\mathrm{el}}(E_{\mathrm{ph}}) = Q_{\mathrm{e}}(E_{\mathrm{ph}})\phi_{\mathrm{bb}}(E_{\mathrm{ph}})\left[\exp\left(\frac{qV}{n_{\mathrm{id}}k_{\mathrm{B}}T}\right)-1\right]. \tag{2.8}$$

While ϕ_{el} and Q_{e} are spectrally reciprocal quantities, the corresponding scalar values are the open-circuit voltage V_{oc} and the quantum efficiency of the LED. The radiative part of the open-circuit voltage, $V_{\mathrm{oc,rad}}$ can be expressed using Eq. 2.5 as

$$V_{\mathrm{oc,rad}} = \frac{n_{\mathrm{id}}k_{\mathrm{B}}T}{q}\ln\left(\frac{j_{\mathrm{sc}}}{j_{0,\mathrm{rad}}}+1\right) \approx \frac{n_{\mathrm{id}}k_{\mathrm{B}}T}{q}\ln\left(\frac{j_{\mathrm{sc}}}{j_{0,\mathrm{rad}}}\right). \tag{2.9}$$

With $j_0 = j_{0,\mathrm{rad}} + j_{0,\mathrm{nrad}}$ in Eq. 2.5, the difference $\Delta V_{\mathrm{oc}} = V_{\mathrm{oc,rad}} - V_{\mathrm{oc}}$ results to

$$\Delta V_{\mathrm{oc}} = -\frac{n_{\mathrm{id}}k_{\mathrm{B}}T}{q}\ln\left(\frac{j_{0,\mathrm{rad}}}{j_{0,\mathrm{rad}}+j_{0,\mathrm{nrad}}}\right).$$

The quantum efficiency of the LED, Q_{LED}, is finally defined as the ratio $j_{0,\mathrm{rad}}/\left(j_{0,\mathrm{rad}}+j_{0,\mathrm{nrad}}\right)$ [19], and may be expressed in terms of

$$Q_{\mathrm{LED}} = \exp\left(\frac{-q\Delta V_{\mathrm{oc}}}{n_{\mathrm{id}}k_{\mathrm{B}}T}\right). \tag{2.10}$$

2.2 Limits of solar cells (and of light-emitting diodes)

When converting the power of incident illumination into electrical power, a large fraction of the incident power is lost. For the following discussion, we assume a single-junction solar cell based on an inorganic semiconductor *p*-*n* junction under unconcentrated illumination, with the inorganic semiconductor solar absorber sufficiently thick to absorb all the incident photons, exhibiting a band-gap energy E_{gap} and perfect collection of generated charge carriers. For such a case, photons with energies $E_{\mathrm{ph}} < E_{\mathrm{gap}}$ are not absorbed. If $E_{\mathrm{ph}} > E_{\mathrm{gap}}$, the electron-hole pair generated by the incident photon almost instantly thermalizes to the conduction and valence-band edges. Correspondingly, the power losses may be categorized as follows:

- Photons not absorbed for $E_{\mathrm{ph}} < E_{\mathrm{gap}}$
- For $E_{\mathrm{ph}} > E_{\mathrm{gap}}$, the excess energy E_{ph} - E_{gap} is lost due to thermalization (interactions with phonons) of excited electrons and holes

The residual power density can be used as electricity. In order to estimate the maximum photovoltaic energy conversion efficiency, the detailed balance theory by Shockley and Queisser (SQ) [20] accounts for all types of (single junction) solar cells as a limiting situation. These authors considered only the detailed balance pair light absorption and light emission. This restriction implies that all details of excitation, charge separation, and transport inside the device are neglected. All absorption of light leads to generation of charge carriers that, in addition, are all collected by the electrical terminals of the device. As consequence, the principle of detailed balance ensures that such a perfect solar cell is also a perfect LED, and that the balance between light absorption and emission defines the radiative efficiency limit [21].

The corresponding photovoltaic performances at the SQ limit can be calculated using Eqs. 2.1, 2.2, 2.9, as well as by using $j_{0,\mathrm{rad}}$ instead of j_0, and $n_{\mathrm{id}} = 1$ in the Shockley equation (Eq. 2.3), in order to calculate the maximum power density of $j_{\mathrm{rad}}(V)$. Also, we set the external quantum efficiency $Q_e(E_{\mathrm{ph}}) = 1$ for $E_{\mathrm{ph}} \geq 1$ and $Q_e(E_{\mathrm{ph}}) = 0$ elsewhere, leading to a larger short-circuit current density, $j_{\mathrm{sc,SQ}}$, as compared with j_{sc} in Eq. 2.7:

$$j_{\mathrm{sc,SQ}} = q \int_{E_{\mathrm{gap}}}^{\infty} \phi_{\mathrm{sun}}(E) dE. \tag{2.11}$$

As incident illumination power density, the AM1.5 spectrum provided by the National Renewable Energy Laboratory, Golden, CO, USA, was used [22]. (AM stands for air mass, while 1.5 is about $1/\cos(42°)$ at longitudes for which the surface normal of the earth points to the sun, at an elevation of 41.81° above the horizon.) Note that all quantities calculated at the SQ limit only depend on the band-gap energy E_{gap} and on the absolute temperature T (assumed to be 300 K) of the semiconductor used as solar-cell absorber. Plots of the power-conversion efficiency, the open-circuit voltage, the short-circuit current density, and the fill factor, as functions of the band-gap energy, are given in Fig. 2.2. Further below in chapter 5.1.4, we will see how close to this theoretical limit one can get using real solar-cell devices.

So far, idealized scenarios have been drawn for solar cells (and LEDs). In real devices, however, loss of power density is also due to the following causes:

1. Shading of collecting grids and due to reflection of illumination at the surface

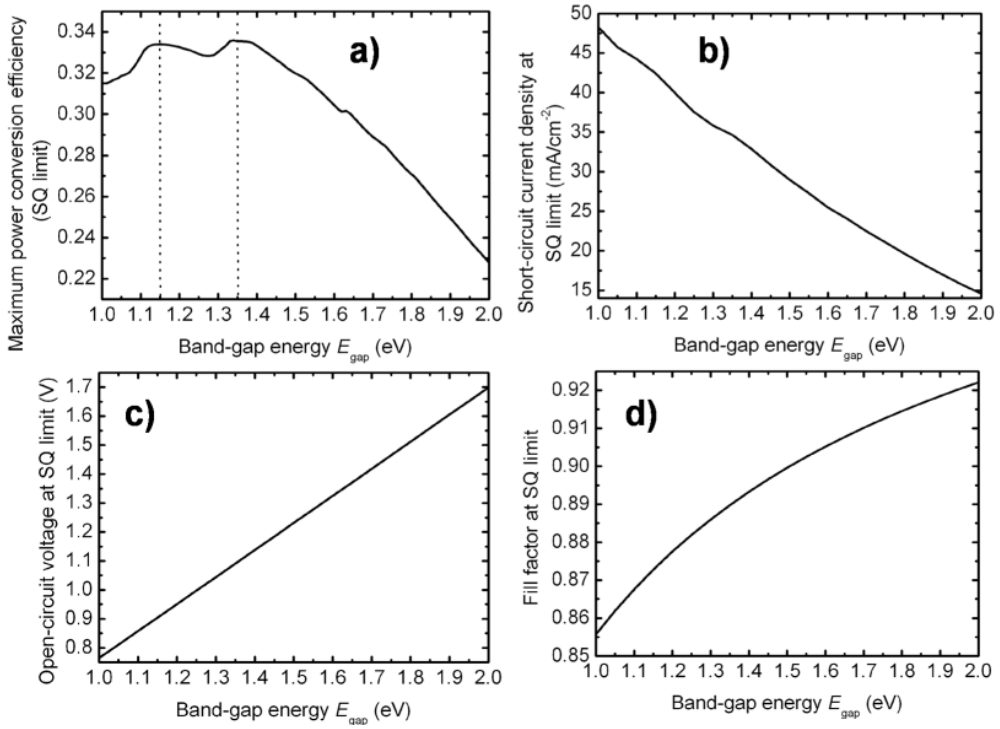

Figure 2.2: Power-conversion efficiency (a), short-circuit current density (b), open-circuit voltage (c), and fill factor (d), as functions of the band-gap energy, calculated using Eqs. 2.1, 2.2, 2.9, and 2.11. In (a), the two local maxima of the power-conversion efficiency at 1.15 and 1.35 eV are highlighted by dotted lines.

2. Absorption in window layers, through which the incident illumination has to travel to reach the absorbing semiconductor thin film

3. Photons with energies E_{ph} close to the absorption edge are weakly absorbed and thus are likely to be transmitted by the absorber

4. The thickness of the absorber, or, more generally, the effective absorption length of photons in the absorbing semiconductor, is not sufficient to absorb all incident photons

5. Series and shunt resistances contribute to further reduction of the power density

6. A further aspect is inhomogeneities in semiconductor absorbers, which may be divided into band-gap and electrostatic fluctuations. Band-gap fluctuations may be due to local variations of compositions (especially in case of compound semiconductors), leading to locally different energetic positions of the conduction and valence-band edges, and consequently to recombination paths with smaller effective band-gap energies. Rau and Werner [23] assumed the prerequisites of the radiative SQ limit (see above) as well as a Gaussian distribution for the band-gap energy E_{gap}, with average band-gap energy $\overline{E}_{\mathrm{gap}}$ and standard deviation $\sigma_{E_{\mathrm{gap}}}$.

These authors calculated that Eq. 2.4 may be expressed in the form of

$$j_{0,\mathrm{rad}} = j_{00} \exp\left(\frac{-\overline{E}_{\mathrm{gap}}}{k_{\mathrm{B}}T} + \frac{\sigma^2_{E_{\mathrm{gap}}}}{2(k_{\mathrm{B}}T)^2}\right),$$

which, inserted in Eq. 2.9, and with $n_{\mathrm{id}} = 1$, results in

$$V_{\mathrm{oc,rad}} = \frac{\overline{E}_{\mathrm{gap}}}{q} + \frac{k_{\mathrm{B}}T}{q} \ln\left(\frac{j_{\mathrm{sc}}}{j_{00}}\right) - \frac{\sigma^2_{E_{\mathrm{gap}}}}{2k_{\mathrm{B}}Tq}. \tag{2.12}$$

This is, the open-circuit voltage may be reduced substantially, even at the radiative limit, by band-gap fluctuations, which are expressed by the quantity $\sigma_{E_{\mathrm{gap}}}$. For the two maxima in Fig. 2.2a at 1.15 and 1.35 eV, Rau and Werner [23] calculated a reduction of the power-conversion efficiency (which is about 33.3% without any fluctuations) of about 2% absolute for $\sigma_{E_{\mathrm{gap}}}$=50 meV. For $\sigma_{E_{\mathrm{gap}}}$ < 25 meV, however, fluctuations do not affect the power-conversion efficiency considerably.

Electrostatic fluctuations are related to redistribution of (free) charge carrier densities, leading to fluctuations of electrostatic potentials $\phi(\overrightarrow{r})$, i.e., of the vacuum level $-e\phi(\overrightarrow{r})$. Thus, for electrostatic fluctuations, the band-gap energy does not change spatially. One may introduce also a standard deviation, σ_{el}, as in the case of band-gap fluctuations, with equal dependencies of the open-circuit voltage. The total fluctuations present in semiconductor absorbers, σ_{total}, are given by $\sigma_{\mathrm{total}} = \sqrt{\sigma^2_{E_{\mathrm{gap}}} + \sigma^2_{\mathrm{el}}}$.

2.3 Recombination mechanisms and extended structural defects

As has already been mentioned above, recombination occurs generally not only radiatively but also via nonradiative processes. Especially interfaces in semiconductor thin-film stacks, where layers of different materials or different phases within individual layers coincide, are resources of midgap states that lead to nonradiative recombination. The three basic recombination mechanisms for photogenerated excess carriers in a semiconductor are (see Fig. 2.3.):

- Radiative recombination: $R_{\mathrm{rad}} = B\left(np - n_i^2\right)$
- Meitner-Auger [24, 25] recombination (nonradiative):
  $R_{\mathrm{Auger}} = \Gamma_n n\left(np - n_i^2\right) + \Gamma_p p\left(np - n_i^2\right)$.
- Shockley-Read-Hall (SRH) recombination [26,27], assuming a trap level at midgap position (nonradiative): $R_{\mathrm{SRH}} = \left(np - n_i^2\right)\left[(n+p)\,\tau\right]$

In these equations, n and p are the electron and hole densities in the excited state, where $np = n_i^2 \exp(qV/k_{\mathrm{B}}T)$ under applied bias V. The quantity n_i^2 is the product of electron and hole densities in thermodynamic equilibrium, $n_0 p_0$. B defines a material-specific radiation coefficient [28], τ is the life time of electron and holes, which is assumed to be equal for the two particles for simplicity, while Γ_n and Γ_p are the Auger coefficients for electrons and holes. Especially in high efficiency solar cells with $\eta > 20\%$, the open-circuit voltage V_{oc} is limited by nonradiative recombination (either

Auger or SRH), which are generally connected to the presence of extended structural defects. Moreover, power-conversion efficiencies of these solar cells are limited mainly because of the limited V_{oc}, apart from further optical and collection losses [29].

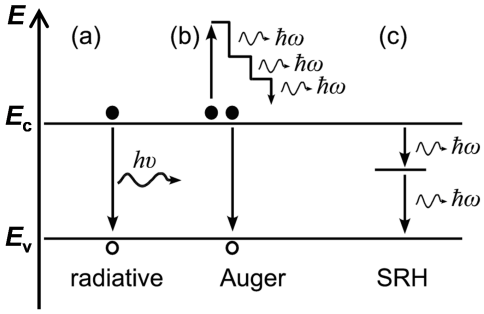

Figure 2.3: Overview of the three basic recombination mechanisms for photogenerated excess carriers in a semiconductor (with conduction-band minimum E_c and valence-band maximum E_v). The excess energy is either transferred to (a) a photon, (b) kinetic energy of an excess electron or hole, or (c) phonons. For case (b), the so-called Auger recombination, the kinetic energy of the electron is lost by collisions with the lattice, which heats up. In case (c), the emission of phonons becomes possible by the existence of states in the forbidden energy-band gap (SRH recombination). Adapted from Ref. [15].

Extended structural defects present in solar cells and LEDs are, similar to interfaces, generally assumed features of enhanced recombination of the generated or injected charge carriers, as compared with the surrounding bulk material. Thus, it is expected that the collection of charge carriers generated by the incident illumination and therefore the usable current density at the contacts of the device is reduced. However, recombination processes are closely linked not only to the current density but also to the open-circuit voltage, see Eq. 2.5. We see that always, the influences of extended structural defects on both, current density and voltage, have to be considered.

How exactly current density and voltage are influenced depends on how (radiative or nonradiative) and where in the solar cell (at interfaces or within the quasi-neutral region) charge carriers recombine. This is because the recombination rates for photogenerated excess carriers in a semiconductor (see list above) depend on the product of electron and hole densities, np. This product varies across a solar-cell stack from $n \ll p$ at one contact to $n \gg p$ at the other. Somewhere in the vicinity of the p-n junction, within the space-charge region, is the position of p equals n, which is where the recombination rates become maximum. At this position, the presence of extended structural defects considered as centers of enhanced recombination is highly detrimental for the power-conversion efficiency.

For dislocations in Si solar cells, various authors have reported direct relationships of densities of this linear defect to the electrical properties of these solar cells. Minority-charge carrier diffusion lengths $L = \sqrt{D\tau}$ [30](D is the diffusion constant of the minority-charge carriers) and also open-circuit voltages of these solar cells [31, 32] are reduced for increasing dislocation densities. Dislocations are also of concern in LEDs, since the thin-film stacks are based on epitaxial growth of Al-In-Ga-N-P-As on sapphire substrates, leading to threading dislocations [33]. Already in the early days of LED research, it was shown [34] that the brightness-current density of the LED

exhibits an inverse relationship to the dislocation density.

We see also by Eqs. 2.8 and 2.9 that relevant physical quantities of the optoelectronic devices solar cell and LED, which are connected to recombination processes, are related to each other. The question remains how these quantities can be improved by controlling the properties of extended structural defects. This question has, to date, not yet been answered. It is connected to the issue of controlling the formation and properties of extended structural defects during the growth of the solar cells or LEDs. Indeed, the growth of most high-efficiency devices is, in this respect, up to date rather a trial-and-error process. This situation may be improved substantially by obtaining better insight into how microstructure develops during the growth. For this task, correlative microscopy as proposed by the present work represents one important basis. It can be applied to, e.g., a series of samples from growth processes interrupted at different points of a specific process.

Furthermore, a thorough analysis of various properties of extended structural defects, as will be reported in the present work, is indispensable for multidimensional device simulations that include also such structural defects. Such simulations have been already performed on several devices (see, e.g., for Cu(In,Ga)Se_2 solar cells, Refs. [35–38]). However, the input for these simulations have been rather limited, in accordance with rather limited information available on extended structural defects and their properties.

Chapter 3

Overview of extended structural defects

The present chapter shall give a short introduction into the various extended structural defects present in a polycrystalline material. Structural defects in general exhibit various dimensions:

- Zero-dimensional defects, i.e., point defects
- One-dimensional, i.e., line defects, which are dislocations
- Planar defects, which are stacking faults, of which twin boundaries are special cases
- Three-dimensional defects, which comprise grain boundaries (in their general form, i.e., those apart from highly symmetrical twin boundaries), and also strain, which can be considered across the whole thin film (macrostrain) or also within individual grains (microstrain). Strain is connected to the formation of dislocations, which occurs upon plastic deformation of a thin film.

In the following, the basic issues on structural defects will be treated.

3.1 Point defects

Point defects in a periodical crystal are (foreign) atoms or vacancies which reside on or in between atomic sites in the crystal structure and disturb the periodicity of the lattice. Self-interstitials are atoms from the bulk of the crystal. Their density can be expected to be rather small in closely packed crystals since they distort the surrounding atomic lattice substantially.

Interstitial impurity atoms, especially if these atoms exhibit much smaller ionic radii than the bulk atoms of the crystal, can be included to much larger densities. If impurity atoms are of equal size as the bulk atoms or even larger, it is more likely that impurity atoms occupy lattice sites of the bulk atoms (substitutional impurity atoms). Finally, an atom may be missing on a specific lattice site (vacancy).

Diffusion of these point defects may occur by exchanging places with an neighboring atom in the crystal lattice via cooperative ringlike rotational movement (ring

mechanism), via vacant sites in the lattice (vacancy mechanism), by exchange of sites of intenstial atoms and point defects on lattice sites, and vice versa (interstitialcy mechanism, for cases where substitutional atoms (point defects) exhibit similar sizes as the atoms in the crystal lattice), and finally by migration of point defects (only) on interstitial sites (interstitial mechanism, only possible for small solute atoms) [39]. In face-centered cubic, body-centered cubic, and hexagonal close packed crystals, self-diffusion occurs predominantly via the vacancy mechanism [39].

If dealing with polycrystalline thin films, grain-boundary diffusion needs to be considered as well [40]. In general, the diffusion along extended structural defects can be assumed to be substantially faster (2-3 orders of magnitude) than the mechanisms for bulk diffusion described above. Thus, it is likely to find point defects segregated to these extended structural defects such as dislocations, stacking faults, as well as twin and (random) grain boundaries.

3.2 Dislocations

A dislocation is a line defect along which the lattice is locally distorted by misalignments of atoms. There are two basic types of dislocations: edge and screw (Fig. 3.1. The magnitude and direction of the lattice distortion is described by the Burgers vector ($\vec{b}$). For an edge (screw) dislocation, the Burgers vector is perpendicular (parallel) to the dislocation line. For dislocations in adamantine (diamond-type) crystal structures, also a mixture of edge and screw dislocations are found, so-called 60° dislocations (where 60° is the angle between dislocation line and Burgers vector).

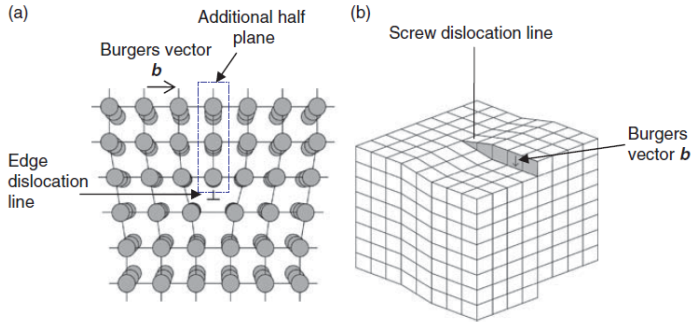

Figure 3.1: (a) An edge dislocation and (b) a screw dislocation in a simple cubic structure. From Ref. [41].

In close-packed and related structures, the shift which is represented by the Burgers vector may become dissociated into two steps. The passage of these partial dislocations involves the formation of stacking faults. Partial dislocations thus appear as boundaries of stacking faults [42]; see Figs. 3.2 and 3.3. In these figures, the dissociation of a 60° dislocation into a 30° and into a 90° partial dislocation is shown.

3.3 Stacking faults and twin boundaries

Extended structural defects that originate from irregularities in the stacking sequence can be divided into twin boundaries (Fig. 3.4a), also called growth stacking faults, and

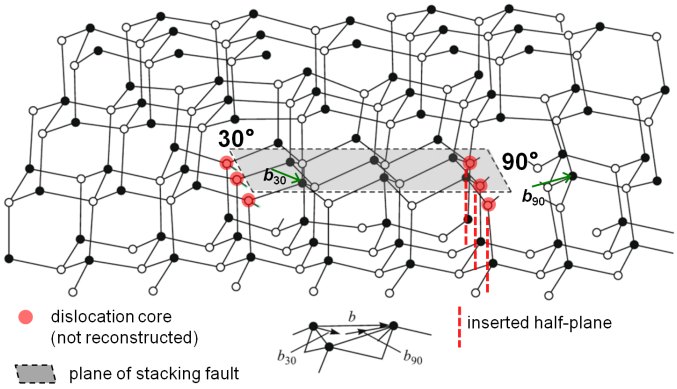

Figure 3.2: Model for dislocation dissociated into a 30° and into a 90° partial dislocation, with a stacking fault ribbon bound between them. The corresponding Burgers vectors are highlighted. By courtesy of Jens Dietrich, TU Berlin, reproduced from Ref. [43].

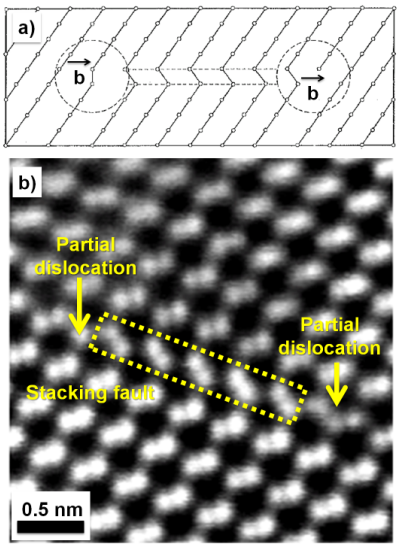

Figure 3.3: a) Schematics of partial dislocations, bound to a stacking fault. From Ref. [42]. b) Partial dislocations, bound to a stacking fault, in a CdTe crystal. By courtesy of Dr. Yanfa Yan, University of Toledo, Ohio, U.S.A. (see also Ref. [44]).

into deformation stacking faults, which are further divided into intrinsic (Fig. 3.4b) and extrinsic stacking faults (Fig. 3.4c). The H and K notations in Figs. 3.4a-c where introduced by Jagodzinski [45]. While at an intrinsic stacking fault, the crystal is undisturbed up to the boundary surface (also true for the twin boundary), an extrinsic stacking fault contains an intermediate layer which differs from the lattices on both sides of the stacking fault. To a first approximation, the energies of different kinds of stacking faults can be estimated as being proportional to the number of foreign sequences (i.e., hexagonal (H) sequences in a face-centered cubic (K) lattice) [42].

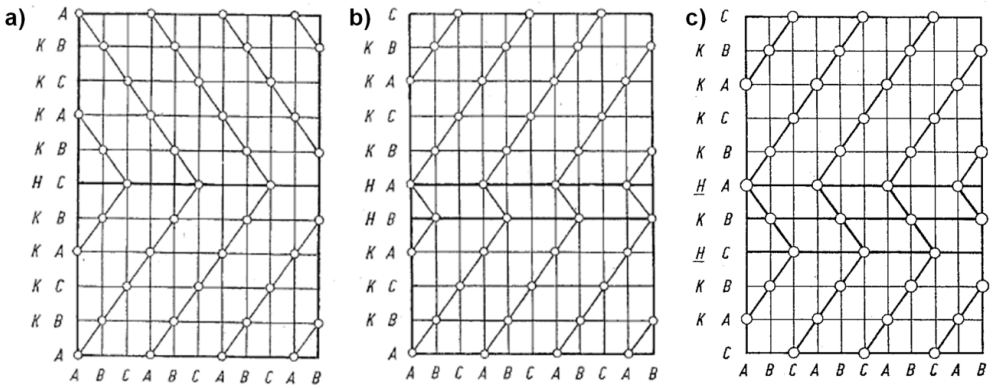

Figure 3.4: Structural models for stacking faults in a face-centered cubic lattice. Twin boundary or growth stacking fault (a), as well as intrinsic (b) and extrinsic deformation stacking faults (c). H and K mark atomic layers according to hexagonal (A,B) and cubic stacking (A,B,C). From Ref. [42].

Apart from structural considerations, stacking faults as well as twin boundaries have also been analyzed electrically. It has been reported in various publications since about 50-60 years (e.g., [46, 47]) that ($\Sigma 3$) twin boundaries in semiconductors do not exhibit strong electrical activities. Moreover, the recombination activities at grain boundaries and intergrain boundaries is dependent on the symmetry of the boundary [48]. On a similar line, also stacking faults were found to exhibit only weak contrasts in measurements of electron-beam-induced current [49]. This is probably since the densities of dangling bonds and correspondingly also sites for impurity atoms (point defects), possibly leading to enhanced recombination, are rather low for both, stacking faults and twin boundaries.

However, no or weak electrical activity may be found only for coherent twins (and stacking faults). For incoherent twins, the densities of dangling bonds are substantially higher. Depending on the reconstruction of the incoherent twin plane by impurities (point defects) and corresponding precipitates (see Ref. [50] for the example of $FeSi_2$ at a twin boundary in multicrystalline Si), deep-level defects may form, leading to enhanced recombination. This situation would be similar as for random grain boundaries (see next section).

3.4 Grain boundaries, macrostrain, and microstrain

3.4.1 Grain boundaries

A boundary surface between any two crystals will take up such a position that the crystals exhibit more or less optimum matching. A mathematical approach to formulate the notion of "matching" two periodic structures is the concept of the coincidence-site lattice (CSL) [42]. Before going into detail into this concept, it is essential to remind that a grain boundary (GB) in general exhibits 5 degrees of freedom in three dimensions: 3 for the misorientation between the point lattices of two neighboring grains, and 2 for the (relative) orientation of the GB plane. The concept of CSL considers only the misorientation and does not concern the orientation of the GB plane. Also, it has to be taken into account that depending on the crystal symmetry of the point lattices, various symmetrically equivalent misorientations exist.

We may now consider two point lattices of two arbitrary neigboring grains which exhibit a specific misorientation to each other (Fig. 3.5). The lattices shall interpenetrate in such a way that lattice points coincide. The resulting CSL exhibits a periodicity depending on that of the original point lattices (of the neighboring grains). In the case of Fig. 3.5, the volume of the unit cell of the CSL is 3 times larger than that of the volumes of the original point lattices. This factor of 3 is called the Σ value of the GB, which is used to classify GBs. Generally, the lower the Σ value, the higher the symmetry of the GB, and also the lower is its formation enthalpy (although not true for all Σ values).

In the example given in Fig. 3.5, the GB is in fact a twin boundary (Fig. 3.4a). However, only if the GB plane is identical to the mirror plane of the boundary, the twin boundary is called coherent, else incoherent. The overestimation of the impact of the Σ concept has also been discussed in the work "The coincidence site lattice and the 'sigma enigma'" by Randle [51].

Any misorientation may be parametrized by an orthogonal misorientation matrix $\underline{R}$ with rational matrix elements a_{ij} and

$$\underline{R} = \frac{1}{N} \begin{pmatrix} a_{11} & a_{12} & a_{13} \\ a_{21} & a_{22} & a_{23} \\ a_{31} & a_{32} & a_{33} \end{pmatrix}.$$

Here, there shall be not any integral factor common to the positive integer N and the nine integers a_{ij}. Grimmer et al. [52] showed that in this case $N = \Sigma$ for cubic crystal lattices. Thus, the misorientation matrix provides another way of determining the Σ value of a GB. Taking again the example of a twin boundary in a face-centered cubic lattice with $\Sigma = 3$, one of the representations of the misorientation matrix is

$$\underline{R} = \frac{1}{3} \begin{pmatrix} 2 & 2 & -1 \\ -1 & 2 & 2 \\ 2 & -1 & 2 \end{pmatrix}.$$

Randomly oriented GBs can be considered all those which do not exhibit a symmetrical constellation of the atomic lattices of the neighboring grains (as is the case for twins). Their Σ values is substantially larger than high-symmetry twins (more than 50 according to Ref. [50]). Random GBs can be classed into small-angle (misorientation less than 10-15 degrees) and large-angle GBs. While small-angle GBs can be resolved

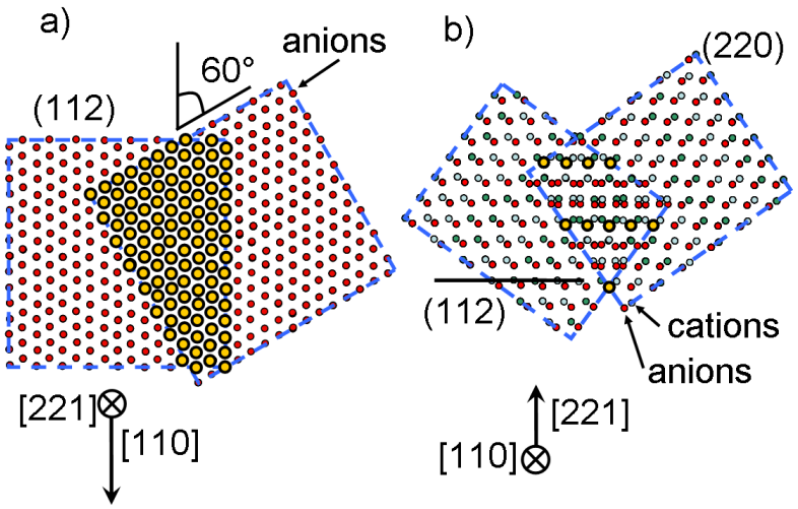

Figure 3.5: a) When superimposing two atomic lattices of $CuInSe_2$, the atoms of these lattices coincide at various sites, forming an atomic lattice with a new periodicity (CSL). This is shown in two dimensions for 112 planes. b) Perpendicular to the 112 planes, the CSL exhibits a lattice constant three times larger than that of the original lattices.

into walls of dislocations, large-angle GBs can either be described by the CSL [42] or by Hornstra's ball-and-wire model [53].

Overviews on structural and electrical properties of (random) GBs in semiconductors can be found in various textbooks and proceedings volumes (e.g., Refs. [3,54–58]). In general, point defects tend to diffuse to GBs, which may lead to deep-level traps acting as centers for enhanced (non-radiative) recombination (see, e.g., chapter 6 in Ref. [54]). Reduced charge-carrier collection is found at small-angle GBs in multicrystalline Si by means of combined electron-beam-induced current (EBIC) and electron backscatter diffraction measurements [7]. This study also shows that the lower the symmetry of the GB, the larger is the reduction of the EBIC signal.

This enhanced recombination of charge carriers at GBs in Si can be explained well by the model proposed by Seto [59]. Based on the temperature dependence of the measured resistivity and Hall mobility across GBs in multicrystalline Si, this author proposed electronic states within the band gap at the GBs due to imperfections of the lattice. These electronic states are occupied by holes and result in a positive excess charge at the GBs which is screened by a negatively charged space-charge region on both adjacent sides. For the current transport through GBs, this means that the majority carriers (holes in *p*-type Si) have to overcome a potential barrier. This process can be described by thermionic emission theory.

As we will see further below when discussing the properties of random GBs in $Cu(In,Ga)Se_2$ thin films, the Seto model working very well for random GBs in Si can not be transferred easily to multiatomic material systems with a large variety of (compensating) point defects.

3.4.2 Macrostrain and microstrain

The terms "macro" and "micro" refer to different length scales. Hereby, "macrostrain" occurs at several to a few hundred micrometers. "Microstrain" refers to a distortion of the atomic lattice within a grain, typically at a scale in the order of 1 μm. This distortion is in strong relation to other extended structural defects such as dislocations, stacking faults, and twin boundaries. Balluffi provides an overview of the elastic theory for crystal defects [60]. The strain field around dislocations can be calculated by the equations provided by Steeds [61].

A good introduction into the topic of strain is given by Krill et al. [62]. We may consider an atomic lattice and a specific lattice-plane family with interplanar distance d. When stress is applied to this lattice, the corresponding, local strain (microstrain) at the position $\mathbf{r}$ can be written as

$$\epsilon(\mathbf{r}) = (d(\mathbf{r}) - d_0)/d_0, \tag{3.1}$$

with the interplanar distance d_0 for the unstrained atomic lattice. Note that the microstrain $\epsilon(\mathbf{r})$ is a tensor with components $\epsilon_{ij}(\mathbf{r})$. The corresponding macrostrain can be regarded as average of $\epsilon(\mathbf{r})$ over the entire sample, while also influences by extended structural defects on this average value have to be considered. The average of $\epsilon(\mathbf{r})$ can be written as

$$\langle\epsilon(\mathbf{r})\rangle = (\langle d(\mathbf{r})\rangle - d_0)/d_0. \tag{3.2}$$

Eq. 3.1 can be expressed in a different way using Eq. 3.2:

$$\epsilon(\mathbf{r}) = \langle\epsilon(\mathbf{r})\rangle + (d(\mathbf{r}) - \langle d(\mathbf{r})\rangle)/d_0.$$

The first term of the sum, $\langle\epsilon(\mathbf{r})\rangle$, is independent of the position $\mathbf{r}$, represents homogeneous deformations of the lattice, and can be identified as the macrostrain. The second term of the sum, $(d(\mathbf{r}) - \langle d(\mathbf{r})\rangle)/d_0$, exhibits an inhomogeneous nature, since the average value $\langle(d(\mathbf{r}) - \langle d(\mathbf{r})\rangle)/d_0\rangle = 0$, and represents the microstrain.

The reader is referred to Refs. [63–67] for approaches to strain analysis by scanning and transmission electron microscopy, as well as by X-ray diffraction.

Chapter 4

Microscopy techniques applied for analyses of structure-property relationships

In the present chapter, an overview of techniques will be given that are used for the analyses of extended structural defects and their influences on performances of corresponding optoelectronic devices. It is not the intention of the author to give a detailed description of all techniques. For this information, the reader is referred to various textbooks (see, e.g., Ref. [68] for a comprehensive overview of several techniques applied also for structure-property relationships in thin-film solar cells). Rather, important aspects of the application of specific techniques with the aim of revealing structure-property relationships in optoelectronic semiconductor devices will be discussed. The chapter starts with the most important step for microscopy analysis, the specimen preparation.

4.1 Specimen preparation for various analysis configurations

The key issue of specimen preparation (not only) for electron microscopy comprises always the optimization of the surface quality of the specimen. Whatever approach may be chosen, the aim is to reduce mechanical defects such as scratches, oxidation, impurities, and similar features to a minimum. A good overview is given in Ref. [69]. In the following, various techniques for specimen preparation are discussed, taking the example of a thin-film solar cell stack.

4.1.1 Plan-view specimens for scanning electron microscopy

The most simplest way of accessing a layer deposited on any substrate is to look at its surface, which may be Ar-ion polished or chemically etched in order to optimize it for imaging and further analyses. However, a layer may also not be accessible easily,

e.g., when sandwiched in between two layers. Then, cross-sectional specimen have to be prepared.

4.1.2 Cross-sections: Fractioning of specimens for scanning electron microscopy

A very simple cross-section preparation for thin-film solar cells on glass substrates, but also for those on foils, is to fracture or cut the cell, which normally takes only seconds. However, since these solar cells in general consists of rather brittle materials, the result may be disappointing, yet justified when aiming for a quick glance on the sample or when surface roughness on the cross-section is not a severe issue. Further more elaborated (and also more time-consuming) methods are described in the following.

4.1.3 Cross-sections: mechanical and ion-beam polishing

Specimens for scanning electron microscopy

Stripes of the solar cell are cut, which then are glued face-to-face together, best by use of epoxy glue which is suitable for high vacuum. From the resulting stack, slices are cut, of which the cross-sections are mechanically polished. Care is advised not to apply too much pressure during the polishing, and that the scratches remaining on the cross-section surface are in the range of 100 nm or smaller in depth. Then, this cross-section sample is introduced in an ion-polishing machine, equipped with, e.g., Ar-ion beams. In order to obtain rather flat cross-section surfaces, small incident angles of about 4° should be chosen. A thin layer of graphite (of about 5 nm in thickness) reduces drift during the measurement and also preserves the cross-section surface, often for several weeks. The graphite seems also to enhance the signal intensities for electron-beam-induced current and cathodoluminescence measurements, probably since it reduces the surface recombination substantially.

Producing cross-sectional specimens for high-resolution transmission electron microscopy analyses

- Combining mechanical and ion polishing. An approach applied frequently for preparing cross-section specimens from thin-film stacks is the combination of mechanical and ion polishing. There are various ways to the final specimen for transmission electron microscopy (TEM):
  - Stripes of the solar cell are cut, which then are glued face-to-face together by use of epoxy glue (similar as for the preparation of scanning electron microscopy (SEM) specimens). One may also glue a piece of Si single crystal to the sample stripe. The resulting stack is introduced into a small tube of about 3 mm in diameter, filled with epoxy glue. From the tube, disks are cut, which are polished on both sides down to thicknesses of about 100 μm. A dimple-grinder introduces a circular deepening in the sample, so that the resulting minimum specimen thickness is about 20-30 μm. Finally, Ar-ion milling at rather small angles (3.5-6°) is performed until a hole forms, preferably at the interface between the two stripes of the solar cell (i.e., the fringe of the hole intersects the thin-film stacks, see Fig. 4.1a).
  - From the stack formed by gluing to stripes of solar cells together face-to-face, also directly disks may be cut. These disks are polished on both sides

until they exhibit thicknesses of about 10 μm. Rings made of Mo or Ni are glued on these very thin cross-section specimens, which will then support them. The Ar-ion milling process is somewhat shorter than in the procedure described above, due to the reduced thickness of the specimen (Fig. 4.1b). Also for this approach, the result is a specimen with a hole at the interface between the solar-cell stripes. I.e., in side view, the specimen has the shape of a wedge, with decreasing thickness towards the hole (Fig. 4.1c).

- Tripod polishing. The stack form by gluing two stripes of solar cells face-to-face together may also be polished by use of a so-called Tripod [69], where the polishing plane is defined by three points. Two points are given by teflon legs, which are kept coplanar, while on the third point at a corresponding leg, the sample is mounted. The pod heights are adjustable by micrometer screws. By use of a Tripod, either plan-parallel specimens may be polished, which are then glued to supporting rings (as described above), or wedge-shaped specimens may be produced (see Fig. 4.1d). Often, specimens prepared by use of a Tripod are post-treated in an Ar-ion polishing machine, in order to further reduce the thicknesses and to optimize the surface qualities.

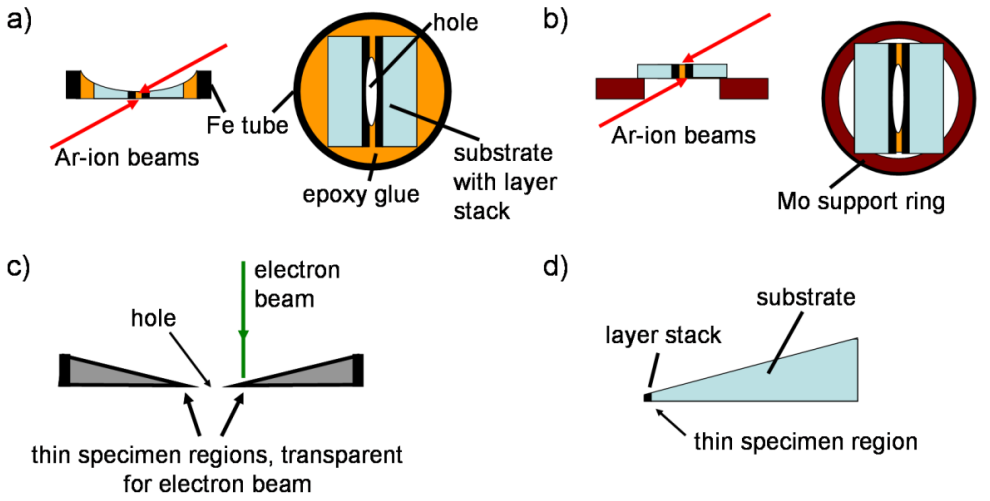

Figure 4.1: Schematics for conventional TEM preparation methods for cross-section specimens. a) Forming a stack by gluing to two stripes of solar cells face-to-face together, and embedding the stack in a Fe tube (cross-section and plan views). b) Polishing the stack and gluing it to a Mo support ring (cross-section and plan views). c) Cross-section view of the geometry of the final TEM specimen with respect to the incident electron beam. d) Preparation of a wedge-shaped specimen by means of a Tripod. At the tip of the wedge, the specimen is transparent for the electron beam. From Ref. [70].

4.1.4 Cross-sections: focused ion beam

Procedures for scanning electron microscopy

A focused Ga-ion beam can be used to sputter trenches into specimens, exposing cross-sections at positions of interest. In a scanning electron microscope, the progress of the sputtering can be monitored by corresponding electron detectors. Also, by alternately FIB slicing and SEM imaging, a 3D image of the specimen may be reconstructed. Similarly, alsoelectron backscatter diffraction and energy-dispersive/wavelength-dispersive X-ray spectrometry may be combined with FIB slicing. It is of advantage to be able to prepare cross-sections specimens and perform imaging and analyses on these specimens without breaking the vacuum, i.e., reducing the effects of surface contaminations substantially. It should be pointed out that by means of FIB, cross-section specimens from thin-film solar cells may be prepared independent of the substrate, which should be particularly helpful when working with, e.g., sensitive foils as substrates.

Producing cross-sectional specimens for high-resolution transmission electron microscopy analyses

Similarly as for SEM specimen preparation, trenches may be formed on two sides of a specific region of interest (Fig. 4.2). The residual specimen lamella between the two trenches can be thinned further, until it is transparent for the electron beam. This lamella is then extracted by use of a micromanipulator needle, and usually put on a TEM grid or welded (e.g., by use of Pt gas) to an appropriate TEM holder. Surface contamination layers formed as consequences of the ion-beam bombardment can be reduced substantially by decreasing the voltage and current of the impinging ion beam. FIB preparation may be also combined with polishing of the specimen in order to reduce the FIB milling duration. Further information of specimen preparation for TEM by use of a FIB can be found in, e.g., Refs. [71–74].

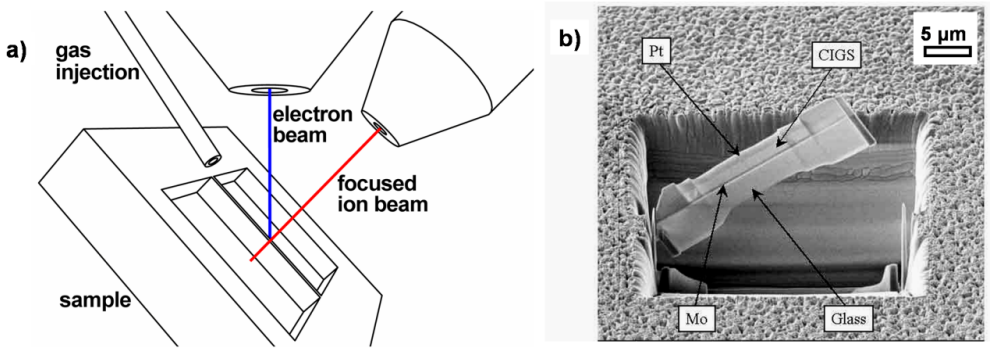

Figure 4.2: a) Schematics of the configuration of the electron and Ga ion sources as well as of the gas injection in a focused-ion beam system within a scanning electron microscope. The preparation of a TEM lamella is indicated. b) SEM image of a TEM lamella prepared by FIB from a CdS/Cu(In,Ga)Se_2/Mo/glass stack. From Ref. [70].

4.1.5 Cross-sections: Plasma etching in a glow-discharge apparatus

Apart from polishing or slicing cross-sections by means of ion beams, also plasmas may be used for this purpose [75]. Particularly, instruments used for glow-discharge optical emission or mass spectrometry may be employed. The specimen functions as cathode in the glow-discharge set-up, and the Ar plasma ignited sputters the specimen atoms. Few seconds sputtering is sufficient for reducing surface roughnesses substantially.

4.1.6 Back surfaces of solar-cell stacks: lift-off approach

The basic concept of lifting-off individual layers in a thin-film solar cell stack is given in Ref. [76]. The following description gives details on preparation of back surfaces for electron-beam-induced current measurements.
After deposition of a graphite layer (serving as diffusion barrier for Ag in the epoxy glue) on the ZnO/ZnO:Al front contact, the solar-cell stack is glued by use of Ag epoxy glue to an Al sample holder (Fig. 4.3). The backside of the Cu(In,Ga)Se_2 absorber layer is exposed by lifting off the Mo-coated glass substrate. In order to passivate the Cu(In,Ga)Se_2 (back)surface and to enhance the conductivity, a graphite layer is evaporated on top.

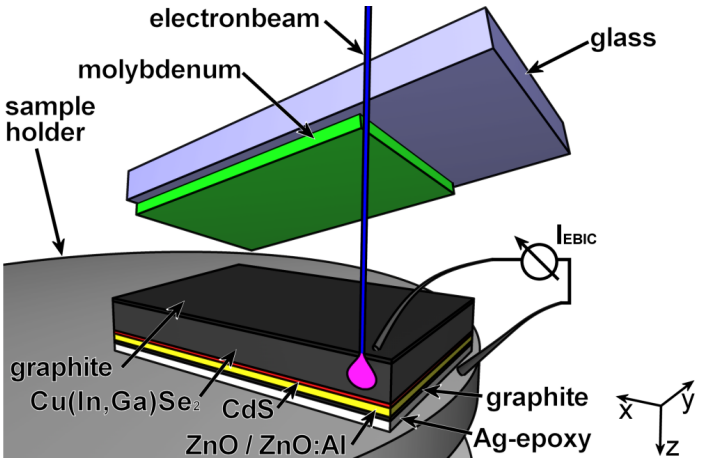

Figure 4.3: Preparation and measuring geometry for electron-beam-induced current measurements on Cu(In,Ga)Se_2 back surfaces. From Ref. [77].

4.2 Considerations for analyses of semiconductors by use of scanning electron beam techniques

When analyzing a semiconductor by use of an electron beam, it has to be taken into account that charge carriers are generated upon electron-beam irradiation, which may be significantly different compared with the generation by sunlight. In the following different scenarios are discussed.

- Injection conditions
  The different spatial distribution of charge carrier generation as compared to

sunlight generation might influence the charge distribution in the solar cell and therefore collection properties, as for example shown in Ref. [78] . The injection level, i.e., the density of excess charge carriers compared with the equilibrium doping level of the semiconductor irradiated, plays an important role. When the density of excess charge carriers is close to or higher than the doping density, the charge distribution within the device is influenced by these excess charge carriers, which also changes the collection properties [79–81]. This effect can be used to estimate the doping density with a good spatial resolution, which can be used, e.g., to detect differences in the doping level of grain boundaries [82].

- Temperature
  When using high electron beam intensities, it is possible that the sample heats up during the measurements, which may result in a modified charge-carrier collection behavior of the device. An estimate of the maximum temperature change due to electron beam irradiation is given by $\Delta T = E_\mathrm{b} I_\mathrm{b} r_\mathrm{b} / K$ [83], where K is the thermal conductivity of the material irradiated, r_b is the beam radius (in our case in the order of the extension of the generation volume), E_b the electron-beam energy and I_b the electron-beam current. A more precise equation for a thin-film substrate structure is also given in Ref. [83].

- Interactions of sample and electron beam
  Generally, the electrons penetrating into the sample have much higher energies compared with light of the solar spectrum. There might also be reactions taking place which are not possible under standard conditions but might influence charge-carrier collection properties. As an example, it was found that the electron beam works as a reducing agent and breaks oxygen bondings passivating compensating donors in a Cu(In,Ga)Se_2 layer, thereby changing its doping density [84].

- Additional interfaces/surfaces
  The experimental setup might lead to additional surfaces or interfaces present in the charge-carrie-collecting device, which are not present under standard conditions using sunlight as excitation source. At these interfaces, there might be enhanced recombination due to an accumulation of defect states as mentioned above. A second effect might also be a different charge equilibrium due to structural reconstruction at the interface (dangling bonds etc.). This results in band bending at the surface and therefore modified collection properties. As an example, it was shown that on InP an oxide causes band bending which assists charge carrier collection [85].

4.3 Combination of various scanning electron and scanning probe microscopy techniques on identical positions

In order to analyze structure-property relationships of semiconductor devices at the nanoscale, it is helpful to investigate various materials and device properties on identical regions of interest. Combining scanning electron and scanning probe microscopy techniques on same identical positions provides the means to correlate microstructural, compositional, electrical, and optoelectronic properties, with spatial resolutions

of about 10-100 nm. On overview is given in Ref. [70].

Examples for a secondary electron (SE) image, electron backscatter diffraction (EBSD) pattern-quality and orientation-distribution maps, monochromatic cathodoluminescence (CL) images, an electron-beam-induced current (EBIC) image, and energy-dispersive X-ray spectrometry (EDX) elemental distribution maps, all acquired on the identical position on a ZnO/CdS/$CuInS_2$/Mo/glass cross-section specimen, are given in Fig. 4.4. By combination of, e.g., the EBSD maps and the CL images, it is possible to relate the local orientations to the local recombination behavior. The EDX maps suggest that the strongly varying local CL intensities are not due to a change in composition, and it is apparent that the EBIC intensities are high where the CL signals are rather low.

There are also reports (e.g., [70]) about platforms integrating scanning electron (SEM), scanning tunneling (STM), atomic force (AFM), and scanning near-field optical microscopy (SNOM). There are obvious benefits from this approach: (a) the tips for STM and AFM can be manipulated with high precision under constant observation in the SEM; (b) the tip and the electron beam are two independent probes that can be controlled simultaneously: one acting as excitation probe, the other acting as sensing probe, depending on the experimental configuration; (c) SEM-based and SPM-based measurements can be performed at the same identical region of interest simultaneously (see [70] for details).

4.4 Combination of electron energy-loss spectroscopy and holography on identical positions

Also in transmission electron microscopy (TEM), it is possible to combine structural/compositional characterization and electrical analyses on the same identical positions, in order to study structure-property relationships in semiconductor devices. One example is the combination of high-resolution imaging, electron energy-loss spectroscopy (EELS) and in-line electron holography, which were performed on the positions of grain boundaries (GBs) in Cu(In,Ga)Se_2 solar cells.

4.4.1 Introduction into inline electron holography

In order to analyze the change in electrostatic potential at the positions of dislocations and GBs in Cu(In,Ga)Se_2 thin films, in-line electron holography in a transmission electron microscope was employed [86, 87]. This technique uses the dependency of the transfer function between object and image wave function on the defocus of the objective lens in a transmission electron microscope. It is based on the acquisition of images with varying defocus value (i.e., changing the objective lens current), keeping all other microscope parameters constant. For the reconstruction of the wave function, the object wave is at the same time its own reference wave. In Figs. 4.5a-c, schematics of the inline electron holography is given. The resulting intensity $I(\overrightarrow{r}, \Delta f) = |\Psi_I(\Delta f, \overrightarrow{r})|^2$ of the image wave of a phase object (constant amplitude and small shifts in phase) is considered at defocus Δf=0 (a), as well as at small (b) and large Δf (c).
For image waves in the focus plane at $\Delta f = 0$ (Fig. 4.5a), the intensity of the image is constant in spite of spatial phase shifts, because of zero interference. For increased defocus Δf (Figs. 4.5b and c), different wave function with varying phase of the object waves interfere, influencing the image intensity $I(\overrightarrow{r}, \Delta f)$. A small defocus (Fig. 4.5b) leads to interference of near regions (equivalent to large frequencies in the Fourier

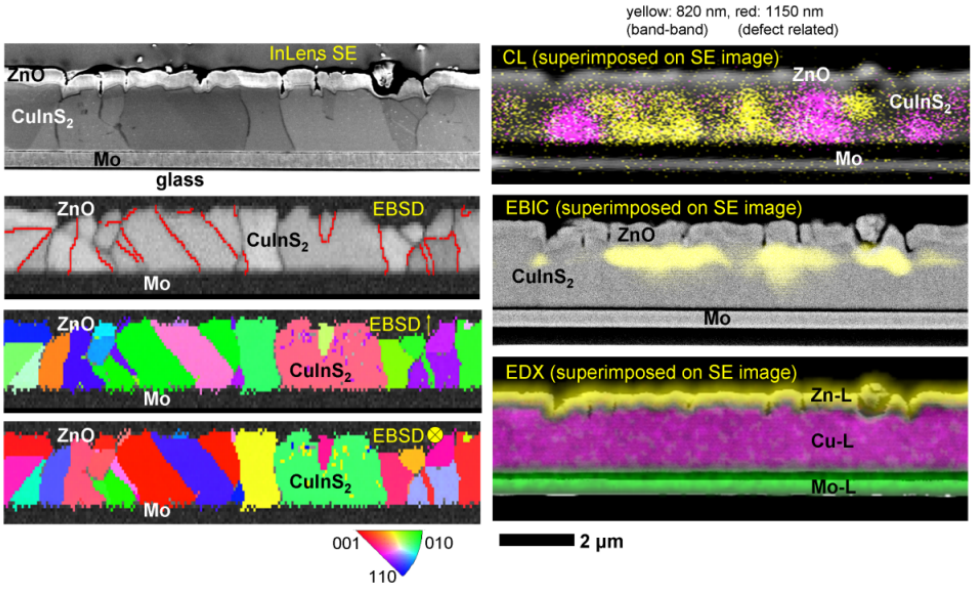

Figure 4.4: SE image (at 3 keV), EBSD pattern quality (with Σ3 grain boundaries highlighted by red lines) and orientation distribution maps (at 20 keV), monochromatic CL images at 10 keV, 8 K, and at 820 (yellow, band-band-transitions) and 1150 nm (pink, defect-related transitions), superimposed on an SE image, an EBIC image (8 keV) and EDX elemental distribution maps (7 keV) from Zn-L (yellow), Cu-L (pink) and Mo-L (green) signals. All images and maps were acquired on the identical position of a ZnO/CdS/$CuInS_2$/Mo/glass stack (provided by courtesy of Dr. B. Marsen, HZB, Berlin, Germany; CL images in collaboration with Dr. U. Jahn, Paul-Drude Institute Berlin, Germany). From Ref. [70].

space), a large defocus would transfer information from small spatial frequencies. This phase contrast by using interference fringes in the image is used to reconstruct the phase of the object wave function, $\phi(\overrightarrow{r})$. Fig. 4.5 also shows TEM images acquired at dislocations in Cu(In,Ga)Se_2 thin films with defocus Δf increased from a-c, resulting in interference fringes in the defocused image plane at the positions of the dislocations.

More precisely, inline electron holography records the lateral variations of the amplitude and phase of the exit-plane electron wave function, after the interaction of the incident electron beam with the specimen (i.e., images containing amplitude and phase information as grey values).

In the framework of the phase object approximation [89], the two-dimensional electrostatic potential $V_\mathrm{a}(x, y)$ within the specimen, which is obtained by averaging the three-dimensional electrostatic potential $V(x, y, z)$ along the path of the electrons through the specimen (here: z axis, corresponding to the optical axis), is linked to the phase of the object wave function by [89]

$$\varphi(x, y) = \sigma(U) \int_{\mathrm{path}} V(x, y, z)\,\mathrm{d}z \approx \sigma(U) t(x, y) V_\mathrm{a}(x, y), \tag{4.1}$$

where $t(x, y)$ is the local specimen thickness and $\sigma(U)$ is an acceleration voltage dependent interaction constant ($\sigma(200\,\mathrm{kV}) \approx 7.3 \times 10^6\,\mathrm{V^{-1}m^{-1}}$). The x and y axes

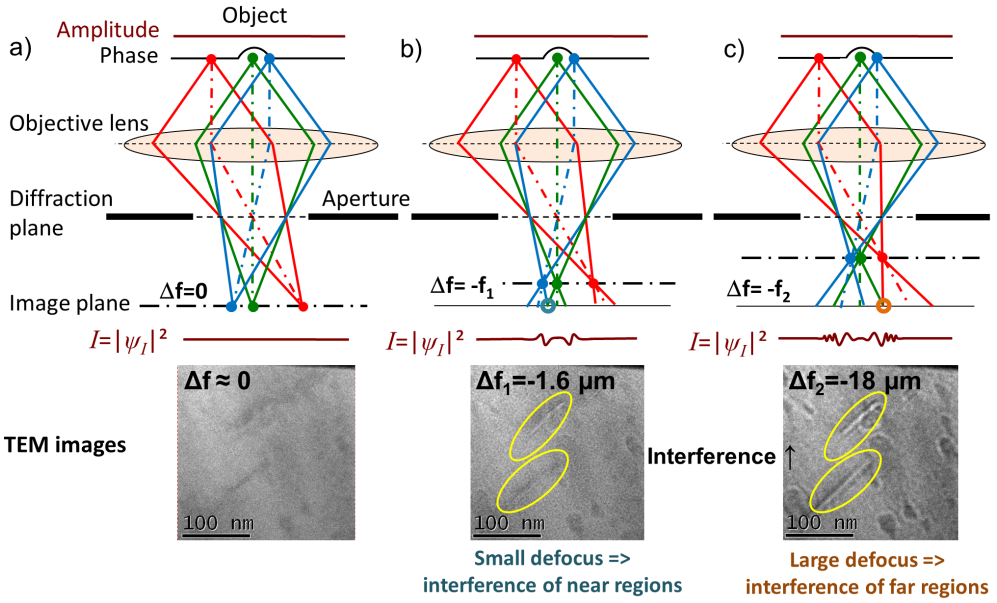

Figure 4.5: Schematics of inline electron holography with the object wave function of a phase object. On the focus plane $\Delta f = 0$, the intensity of the image wave $I(\overrightarrow{r}, \Delta f) = |\Psi_I(\Delta f, \overrightarrow{r})|^2$ is constant. At increased Δf (b and c), different object waves, which exhibit a phase shift to one another, interfere and influence the image intensity correspondingly. A small defocus (b) leads to interference of near regions (highlighted by blue circle), a larger defocus (c) of far regions (orange circle). TEM images are given to illustrate the effect of the defocus Δf on the interference fringes in the image. Adapted from Ref. [88].

in Eq. 4.1 are both chosen perpendicular to the z axis. Maps of the local specimen thickness were obtained by [90]

$$t(x, y) = \lambda_{\text{mean}} \ln(I_t(x, y)/I_0(x, y)), \tag{4.2}$$

where λ_{mean} is the inelastic mean free path of beam electrons within the specimen, $I_t(x, y)$ is the intensity distribution of an unfiltered TEM image, and $I_0(x, y)$ is the intensity distribution of a zero-loss filtered TEM image. The inelastic mean free path λ_{mean} was estimated by use of an algorithm given in Ref. [90].

The local variation of the phase $\varphi(x, y)$ is proportional to the variation in the projected electrostatic potential that an electron experiences when it travels through the specimen [91]. The average potential can then be calculated using

$$\Delta V_{\text{av}}(x, y) = \frac{\varphi(x, y)}{\sigma\, t(x, y)}. \tag{4.3}$$

The local variation of the averaged electrostatic potential (not to be confused with potential energy) can be considered as the sum of variations related to a lateral redistribution of free charge carriers, ΔV_{charge}, and to the mean-inner potential (MIP):

$$\Delta V_{\text{av}} = \Delta\text{MIP} + \Delta V_{\text{charge}}. \tag{4.4}$$

The MIP is due to the distribution of all charges within the neutral solid, i.e., protons and electrons, and is - because of the higher localization of positive charges - a positive quantity. Changes in MIP can be caused by variations in the (local) composition, in crystal structure and/or in the (local) density. The MIP of a crystalline material can be roughly estimated by use of [92]

$$MIP = \frac{h^2}{2\pi m_e e \Omega} \sum_j n_j f_j^{el}(0), \tag{4.5}$$

where m_e is the effective mass of electrons, e the elemental charge, Ω is the volume of the unit cell, n_j is the number of atoms or ions of type j within the unit cell, and $f_j^{el}(0)$ are the corresponding atomic or ionic scattering factors in forward direction. An approximation of the MIP by use of Eq. 4.5 neglects any charge redistributions of electrons due to bonding between atoms or ions.
Fig. 4.6 shows, as an example, distributions of the relative phase shift and the specimen thickness around a random GB in a Cu(In,Ga)Se_2 thin-film as well as of the resulting profile across the GB, which was extracted from the distribution of the average electrostatic potential, calculated by use of Eq. 4.3. For these types of thin films, always potential wells are measured. One fundamental question is whether contributions from ΔV_{charge} or from the MIP dominate these local minima in average electrostatic potential.

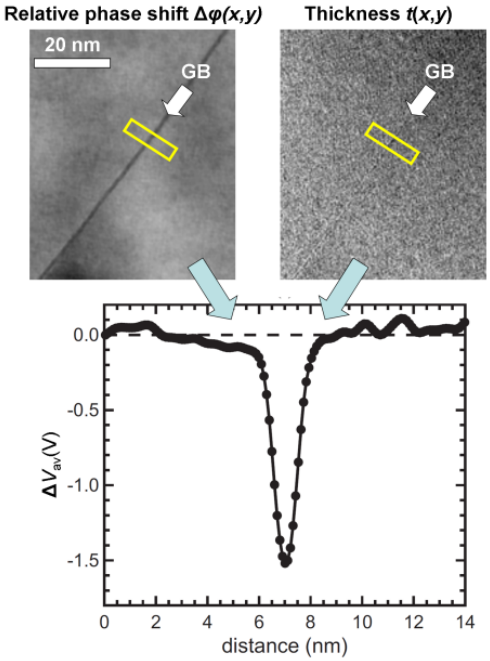

Figure 4.6: Relative phase shift $\phi(x, y)$ and specimen thickness $t(x, y)$ of the identical area on a Cu(In,Ga)Se_2 thin-film in a completed solar cell. From the regions highlighted by yellow frames, profiles were extracted, and the shown profile of the spatial distribution of the averaged electrostatic potential, $\Delta V_{\text{av}}(V)$, across the GB was calculated by use of Eq. 4.3. From Ref. [93].

4.4.2 Electron energy-loss spectroscopy

Recording the inelastically scattered electrons in a TEM specimen, which is termed electron energy-loss spectroscopy (EELS) when spectrally resolved, provides a large range of material properties at the subnanometer scale. The EEL spectrum can be divided into several sections (corresponding to different causes for energy loss):

- The zero-loss peak (at 0 eV)
- The low-loss region (0 - 50 eV), which gives information on phonon scattering, intraband excitation, plasmons (and thus on dielectrical constants), and interband transitions (and thus also on local band-gap energies)
- The ionization edges (50 eV - few keV) providing information on local composition, the binding state and the density of states (via the near-edge structure), as well as on the distance of neighboring atoms (via the extended energy-loss fine structure).

Further details on the EELS technique can be found in Ref. [90].

4.4.3 Correlative analysis of electron energy-loss spectroscopy and electron holography

Although EELS (e.g., [94–97]) and electron holography (e.g., [98–103]) have been separately applied for analysis of extended structural defects, correlative applications on same identical positions have been, so far, very rare [93]. This is, however, the only approach at scales of few nanometers or lower (also considering nanodiffraction methods in TEM [104]) to study the influences of charge accumulations and atomic reconstructions at extended structural defects. Moreover, especially in combination with high-resolution imaging of the atomic lattice, it may be explored whether changes in the atomic density (strain fields around dislocations, spacings in the atomic structure, atomic reconstruction) or redistribution of free charge carriers dominate the potential distributions around an extended structural defect. This is an important contribution also in revealing parameters used as input for multidimensional device modelling. In Chapter 5.5.6 below, an example of such correlative analysis will be given on GBs in $Cu(In,Ga)Se_2$ thin films.

4.5 Information depths of techniques

An important issue of analyses of extended structural defects, which also affects the comparability of results on properties of these defects obtained by various characterization techniques, is the information limit of a specific method. One is often tempted to combine information obtained by different methods, ignoring the different information depths. However, it is obvious that a property of an extended structural defect at the surface of a thin film may not be the same identical as the one present within the volume of the thin film. One only needs to consider, e.g., the densities of dangling bonds.
An overview of various techniques applied for grain-boundary analysis and their information depths is given in Table 4.1. The different information depths are also depicted in Fig. 4.7

Table 4.1: Overview of various techniques applied for grain-boundary analysis and their information depths.

Technique	Type of information	Information depth
Imaging in electron microscopy (SEM and TEM)	Distribution of crystal defects	few nm to few 100 nm
Imaging in atom force microscopy (AFM)	Distribution of crystal defects	1 nm
Imaging in scanning tunneling microscopy (STM)	Distribution of crystal defects	1 nm
Electron backscatter diffraction (EBSD)	Local crystal symmetry and orientation; classification of grain boundaries	5-100 nm
Electron diffraction in TEM	Local crystal structure and lattice contants	few 10 to few 100 nm
Energy-dispersive X-ray (EDX) and electron energy-loss sepctroscopy (EELS) in aberration-corrected TEM	Local composition	few 10 nm
Auger electron spectroscopy (AES)	Local composition	1 nm
Atom-probe tomography (APT)	Local composition (3D)	1 nm
conductive atom force microscopy (c-AFM)	Local transport	depending on distance between contacts; surface sensitive
Kelvin-probe force microscopy (KPFM)	Local electrical work function; distribution of electrical potential	< 1 nm
Scanning capacitance microscopy (SCM)	Local capacitance; local doping concentrations	depending on distance between contacts; surface sensitive
Scanning tunneling spectroscopy (STS)	Local j/V characteristics; density of states	< 1 nm
Electron-beam-induced current (EBIC)	Local short-circuit current	few 100 nm to few μm (depending on diffusion length)
Cathodoluminescence (CL)	Distribution of radiative recombination	few 100 nm to few μm (depending on diffusion length)
Electron holography in TEM	Local electrostatic (scattering) potential	few 100 nm

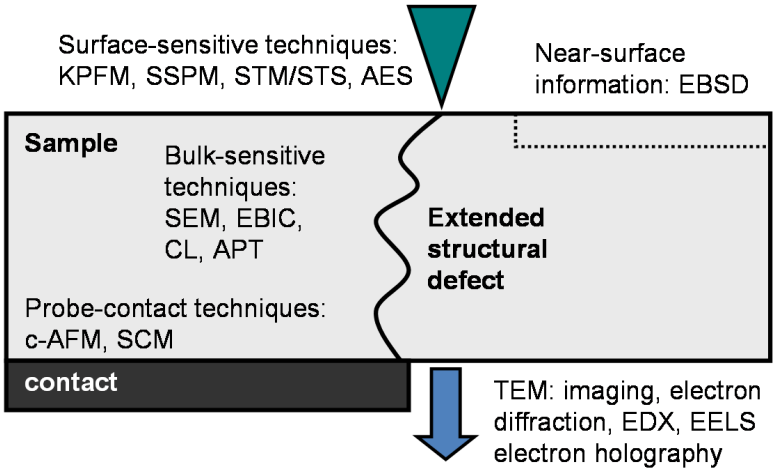

Figure 4.7: Various techniques for the analysis of extended structural defects in a thin film, and their information depths. For the abbreviations, see Table 4.1.

Chapter 5

Structure-property relationships in Cu(In,Ga)Se_2 thin-film solar cells

The present chapter gives first an introduction into Cu(In,Ga)Se_2 thin-film solar cells, with an emphasis on their limitations. Also, an overview of various extended structural defects in Cu(In,Ga)Se_2 thin films is presented. In detail, their structural, compositional, electrical and optoelectronic properties are discussed. Particularly, correlative microscopy approaches are described in order to access these properties on various length scales from subnanometers to several hundred micrometers. It should be noted that the structure-property relationships discussed in the present chapter are related to microscopic properties as revealed by microscopy techniques.

5.1 Introduction into Cu(In,Ga)Se_2 thin-film solar cells

Thin-film solar cells have reached highest solar-conversion efficiencies of more than 20% by use of Cu(In,Ga)Se_2 absorber layers. Regarding the microstructure, Cu(In,Ga)Se_2 solar cells with typical ZnO/CdS/Cu(In,Ga)Se_2/Mo stacks on glass substrates (Fig. 5.1) and more than 19% efficiency have been achieved with rather small (< 1 μm [11, 105, 106]) and also with large average grain sizes (> 1 μm [107]). An overview of corresponding scanning electron micrographs and a electron backscatter diffraction (EBSD) map is given in Fig. 5.2.

Apparently, at least for 19-20% efficiencies, the average grain size may vary within a considerably large range of about 0.5 to 1.5 μm, with the grain-boundary (GB) density differing correspondingly. This fact can be explained by the presence of various extended structural defects, which may impact to the solar-cell performance. Layers with larger grains exhibit a smaller density of GBs but probably a larger density of structural defects as dislocations and stacking faults within individual grains. Before an overview of these various defects in Cu(In,Ga)Se_2 thin films will be given, the material system Cu(In,Ga)Se_2 will be introduced in the following section.

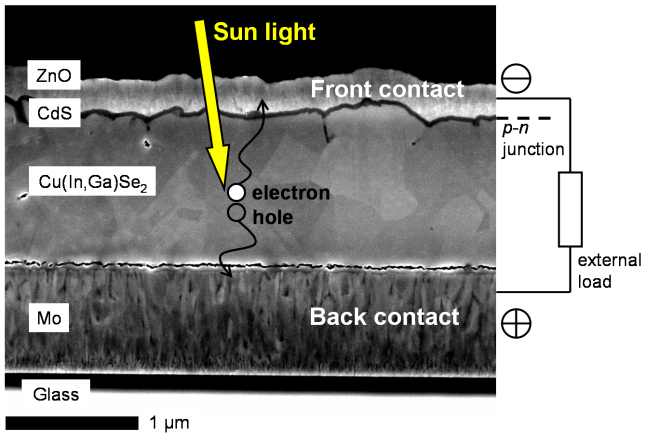

Figure 5.1: Scanning electron micrograph of a ZnO/CdS/Cu(In,Ga)Se_2/Mo solar-cell stack. The cell is illuminated through the ZnO/CdS window layer. Impinging photons generate electron-hole pairs throughout the ZnO/CdS/Cu(In,Ga)Se_2 stack, which are separated by the space-charge region and collected at the ZnO and Mo contacts. The corresponding photocurrent may be used via an external load.

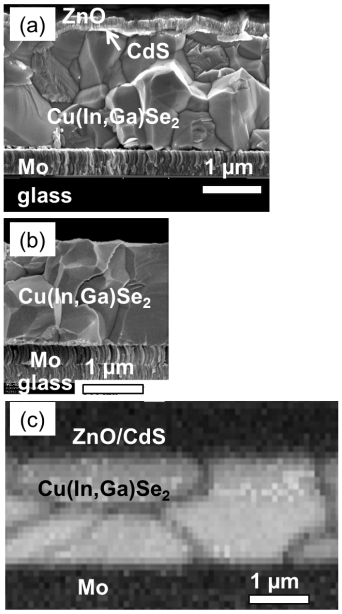

Figure 5.2: Cross-sectional, scanning electron micrographs of a) a 20.3% Cu(In,Ga)Se_2 cell produced at the Center for Solar Energy and Hydrogen Research (ZSW), Stuttgart, Germany (courtesy Dr. T. Magorian Friedlmayer), and of b) a 20.0% Cu(In,Ga)Se_2 cell from the National Renewable Energy Laboratory (NREL), Golden, CO, U.S.A. (reproduced from Ref. [11]), as well as c) a cross-sectional, electron backscatter diffraction map of a 19.4% Cu(In,Ga)Se_2 solar cell from Helmholtz-Zentrum Berlin, Germany (sample courtesy of Dr. T. Rissom).

5.1.1 Growth of Cu(In,Ga)Se_2 thin films

All Cu(In,Ga)Se_2 thin films for high solar-conversion efficiencies of more than 19% have been grown by so-called three-stage processes [108–110], which involve diffusion of elements in the growing thin films with phase formations at elevated temperatures (typically 300-600°C). In the present work, only solar cells with Cu(In,Ga)Se_2 layers from such processes will be discussed. Basically, a three-stage process consists of a first stage, during which an In-Ga-Se layer is deposited at lower substrate temperatures of about 300-330°C, a second stage, during which the substrate temperature is increased to about 520-600°C, as well as Cu and Se are coevaporated until a film composition with [Cu]/([Ga]+[In]) > 1 is reached, and a third stage, during which In, Ga, and Se are coevaporated until [Cu]/([Ga]+[In]) < 1 (see also Fig. 5.3). For achieving the goal of conversion efficiencies of 21% and beyond, it would be essential to have decent knowledge about formation mechanisms of structural defects during the growth of Cu(In,Ga)Se_2 thin films. Unfortunately, the current status is still far away from such a situation.

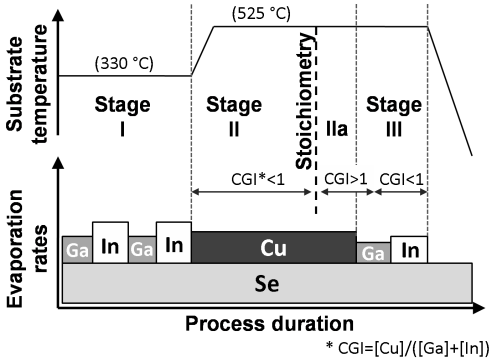

Figure 5.3: The three stages of a typical three-stage process, in dependence of the Cu, In, Ga, and Se evaporation rates as well as of the substrate temperatures. At the point of time during the process indicated by stoichiometry and a dashed line, the [Cu]/([In]+[Ga]) ratio becomes 1. Adapted from Ref. [88].

Equally little knowledge is available about the impact of extended structural defects on the photovoltaic performances of Cu(In,Ga)Se_2 thin-film solar cells. As will be detailed further below, extended structural defects reduce only slightly the short-circuit current density of the solar cells. Indeed, Cu(In,Ga)Se_2 thin-film solar cells are limited in their open-circuit voltage [29, 111, 112], to which probably enhanced nonradiative recombination at extended structural defects contribute substantially.

5.1.2 Crystallography, elemental distributions and optical band gap

Cu(In,Ga)Se_2 is a solid solution of $CuInSe_2$ and $CuGaSe_2$. These compounds are substoichiometric with a considerable concentration of Cu vacancies of few at.% [113]. The crystal structure of Cu(In,Ga)Se_2 is of chalcopyrite-type, i.e., tetragonal (Fig. 5.4), while the ratio of the lattice constants c/a exhibits a linear relationship to the integral Ga concentration (Vegard's law of solid solutions [114]). Note that In and

Ga are generally distributed homogeneously parallel to the substrate but not perpendicular to it, i.e., these elements exhibit gradients along the growth direction of the Cu(In,Ga)Se_2 thin film. In contrast, Cu and Se are homogeneously distributed throughout the Cu(In,Ga)Se_2 thin film. The integral Ga concentration may be expressed by the compositional ratio x=[Ga]/([Ga]+[In]) [115].

Since $CuInSe_2$ and $CuGaSe_2$ exhibit different band-gap energies at room temperature of 1.04 and 1.68 eV [116], the local [Ga]/([Ga]+[In]) ratio also determines the local band-gap energy via [117]

$$E_{\mathrm{gap}}(x) = (1-x)E_{\mathrm{gap}}(\mathrm{CuInSe_2}) + xE_{\mathrm{gap}}(\mathrm{CuGaSe_2}) - bx(1-x), \qquad (5.1)$$

where $0.15 \geq b \geq 0.24$ is an optical bowing factor.

For highest power-conversion efficiencies of more than 19%, Cu(In,Ga)Se_2 thin films with $0.22 < x < 0.38$ are used [118]. Within this compositional range, the c/a ratios are very close to 2. It is an interesting fact that for Cu(In,Ga)Se_2 thin films with x values for which $c/a = 2$ (pseudocubic crystal structure), i.e., x about 0.23, also largest average grain sizes have been reported [119]. Hence, the c/a ratio of the tetragonal crystal structure has a substantial influence on the microstructure of a Cu(In,Ga)Se_2 layer. It should be mentioned that the larger average grain sizes for $CuInSe_2$ than for $CuGaSe_2$ (when grown using identical recipes) can also be attributed to the larger formation enthalpy for $CuGaSe_2$ than for $CuInSe_2$ [120], leaving less energy for the crystal growth during the three-stage process.

Moreover, for Cu(In,Ga)Se_2 crystals with x values of around 0.23, symmetrically nonequivalent crystal orientations in the tetragonal structure (e.g., <110> and <201>, corresponding to the lattice planes {110} and {102}) may not be distinguished in diffraction experiments [121]. In this case, the crystal structure is generally considered quasi-cubic.

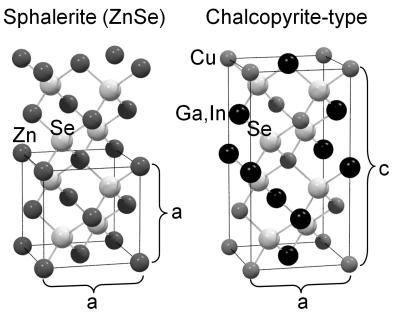

Figure 5.4: Representations of the sphalerite (ZnSe) and the chalcopyrite-type (Cu(In,Ga)Se_2) structures.

5.1.3 Impurities in Cu(In,Ga)Se_2 thin films

An important issue in the research and development of Cu(In,Ga)Se_2 solar cells is the diffusion of impurities from the substrates into the active layers. When using for the first time soda-lime glass instead of borosilicate glass substrates in 1993, Hedström et al. [122] obtained substantially higher power-conversion efficiencies of 16.9%. This meant an increase of several absolute percentages at that time, which was attributed mainly to the indiffusion of Na from the soda-lime glass substrate through the Mo

back contact into the Cu(In,Ga)Se_2 layer (this glass type contains a substantially higher concentration of Na_2O than borosilicate glass). The diffusion through Mo is facilitated by oxides present at the grain boundaries in the polycrystalline Mo thin film, where the crystal structure of these oxides is a layered, planar one (similar to that of graphite).

The influences of Na on Cu(In,Ga)Se_2 growth as well as on structural and electrical properties of these thin films and solar cells are summarized in the comprehensive work of Rudmann [123]. In short terms, Na tends to occupy Cu vacancies and also In and Ga sites in Cu(In,Ga)Se_2 layers, impeding In and Ga interdiffusion during film growth. Moreover, Na has a substantial effect on the net doping by forming Na_{Cu} point defects. Indeed, the net doping has been shown to increase substantially when using soda-lime glass substrates (containing Na), as compared with Na-free substrates. As we will see further below, Na also tends to segregate to extended structural defects. Apart from Na_2O, also other oxides (CaO, and also Al_2O_3, MgO, K_2O to a smaller concentration, apart from SiO_2) are present in soda-lime glass substrates. The effects of the cations of these oxides on the electrical properties of the Cu(In,Ga)Se_2 thin films have not yet been studied in detail. Whenever substrates are used for Cu(In,Ga)Se_2 solar cells that do not contain any Na, this element has to introduced, generally by means of NaF, in order to achieve highest power-conversion efficiencies.

5.1.4 Limitations of Cu(In,Ga)Se_2 solar cells

As pointed out in the introduction of the present chapter, Section 5.1, Cu(In,Ga)Se_2 solar cells have reached the highest power-conversion efficiencies of all thin-film photovoltaic devices, of up to more than 20%. For research and development of these solar cells, it is indispensable to determine which the limitations of the Cu(In,Ga)Se_2 solar cells are. As starting point, the SQ limit introduced in Section 2.2 may be considered. The maximum power-conversion efficiency at the radiative limit (Fig. 2.2a) exhibits two local maxima at band-gap energies of 1.15 and 1.35 eV. Using a band-gap energy E_{gap} of 1.15 eV and a bowing factor $b = 0.2$ in Eq. 5.1, the corresponding integral compositional ratio x=[Ga]/([Ga]+[In]) in the Cu(In,Ga)Se_2 thin film can be calculated to about 0.23 (it would be about 0.56 for $E_{gap} = 1.35$ eV).
The maximum power-conversion efficiency, the short-circuit current density, the fill factor, the open-circuit voltage and the saturation current at the radiative limit for E_{gap} = 1.15 eV and T=300 K are given in Table 5.1. Also listed are the best corresponding values of various Cu(In,Ga)Se_2 record cells available in the literature [11, 105, 124] (it should be noted that these record cells exhibit [Ga]/([Ga]+[In]) ratios deviated from the value of 0.23). It is apparent that the Cu(In,Ga)Se_2 solar cells are limited mainly by their open-circuit voltage, while also fill factor and short-circuit current density are decreased with respect to the SQ limit.

In the following, limitations of Cu(In,Ga)Se_2 solar cells will be discussed with respect to the publication by Siebentritt [29] and according to the loss mechanisms depicted in Section 2.2:

The following issues affect mainly the short-circuit current density.

- Shading of collecting grids and reflection of illumination at the surface. These losses may be reduced by an enhanced grid design and also by improved anti-reflection coating of the Cu(In,Ga)Se_2 solar-cell stack.

- Absorption in window layers, through which the incident illumination has to

Table 5.1: Maximum power-conversion efficiency η, the short-circuit current density j_{sc}, the fill factor FF, the open-circuit voltage V_{oc}, and the saturation current j_0 at the radiative limit for E_{gap} = 1.15 eV and T=300 K, as well as the corresponding best values for various Cu(In,Ga)Se_2 record cells [11, 105, 124, 125]. Also given is the ratio of the photovoltaic parameters for Cu(In,Ga)Se_2 record cells, divided by the values at the SQ limit.

Photovoltaic parameter	SQ limit	Cu(In,Ga)Se_2 solar cell	Cu(In,Ga)Se_2/SQ ratio
η (%)	33.3	20.9 [14]	0.63
j_{sc} (mA/cm^{-2})	42.4	39.9 [14]	0.94
FF (%)	87	81 [11]	0.93
V_{oc} (mV)	904	757 [13]	0.84
j_0 (mA/cm^2)	2.7×10^{-14}	2.1×10^{-12}	78

travel to reach the absorbing semiconductor thin film. This loss can be improved by choosing window and buffer layers with larger band-gap energies. For example, Zn(O,S) buffer layers exhibit larger band-gap energies (up to 3.8 eV) than the usually employed CdS (2.4-2.5 eV).

- The effective absorption length of photons in the absorbing semiconductor is not sufficient to absorb all incident photons. This issue is negligible for absorbers with thicknesses of 2-3 μm, also in view of that Cu(In,Ga)Se_2 exhibits high absorption coefficients of about 10^5 cm^{-1}. In addition, also a shorter collection length, i.e., the width of the space charge region plus the diffusion length of the minority charge carriers, contributes to a further reduction of the short-circuit current density. This loss can be reduced by adjusting the width of the space-charge region via the net doping density of the Cu(In,Ga)Se_2 absorber, and by a reduced degree of doping compensation (as present in the compound semiconductor Cu(In,Ga)Se_2 with a large number of point defects) [29].

- Photons with energies E_{ph} close to the absorption edge are weakly absorbed and thus are likely to be transmitted by the absorber. The corresponding reduction in short-circuit current density were estimated to about 3 rel.% by device simulations using the absorption spectrum published by Malmström et al. [126] and the software SCAPS [127].

- For high-efficiency Cu(In,Ga)Se_2 solar cells, the collected current density at the contacts is reduced mainly by recombination in the quasi-neutral region of the Cu(In,Ga)Se_2 absorber layer [15].

The next items are related mainly to losses in fill factor.

- In recent Cu(In,Ga)Se_2 record cells, series resistances of as low as 0.4 Ω cm^{-2} and shunt resistances of as high as 5000 Ω cm^{-2} have been reported [11,105]. According to Siebentritt [29], the corresponding reductions of the power-conversion efficiency with respect to a Cu(In,Ga)Se_2 solar cell exhibiting zero series and infinite shunt resistances are only 0.5 and less than 0.01% absolute. Thus, they are negligible.

- Voltage-dependent photocurrent density $j_{\mathrm{ph}}(V)$, which is normally evaluated by comparing current density / voltage characteristics acquired in the dark and under illumination. According to Scheer and Schock [128], $j_{\mathrm{ph}}(V)$ is linked to the short-circuit current density j_{sc} via the external collection efficiency $\eta(V)$ by $j_{\mathrm{ph}}(V) = j_{\mathrm{sc}}\eta(V)$. Moreover, the external collection efficiency is related to the fill factor FF via [129]

$$FF = \eta(V_{\mathrm{MPP}}) \left[1 - n_{\mathrm{id}} \ln\left(qV_{\mathrm{oc}}/k_{\mathrm{B}}T\right) / \left(qV_{\mathrm{oc}}/k_{\mathrm{B}}T\right)\right]. \tag{5.2}$$

  Using the photovoltaic parameters for Cu(In,Ga)Se_2 solar cells with power-conversion efficiencies above 20% [11, 105], the external collection efficiency at the maximum power point, $\eta(V_{\mathrm{MPP}})$, is calculated to about 93-94%. This is, the fill factor FF would be reduced by about 6-7 rel.%, which agrees well with the limitation given in Table 5.1.
  It should be noted that according to Eq. 5.2, the fill factor also depends on the diode ideality factor n_{id}, which again is related to recombination paths of charge carriers [15].

Another issue is inhomogeneities in Cu(In,Ga)Se_2 thin films, reducing mainly the open-circuit voltage (see Eq. 2.12).

- These inhomogeneities can be divided into band-gap and electrostatic fluctuations. Band-gap fluctuations are mainly due to variations of the local [Ga]/([Ga]+[In]) ratio. In order to result in a substantial reduction of the open-circuit voltage (Eq. 2.12), the standard deviation $\sigma_{E_{\mathrm{gap}}}$ should be in the range of 50 meV, i.e., the variation of the Ga concentration [Ga] in the Cu(In,Ga)Se_2 layer has to be about 2 at.%. Such large compositional variations within few tens of nanometers have, to date, never been reported (except for In/Ga gradients, which are extended over much larger distances and only perpendicular and not parallel to the substrate). Indeed, the band-gap fluctuations measured by means of spatially-resolved photoluminescence [130] and cathodoluminescence spectrometry [131, 132] on Cu(In,Ga)Se_2 layers for high-efficiency devices have been reported to be in the range of 8-10 meV. Thus, this kind of inhomogeneities can be neglected as source for reduction of the open-circuit voltage.
  Electrostatic fluctuations at grain boundaries on surfaces in Cu(In,Ga)Se_2 thin films have been characterized by means of various scanning probe microscopy measurements [133–141]. Overall, the reported values for variations in electrostatic potentials at grain boundaries are in the range of several 100 meV. Such strong electrostatic fluctuations have been proposed as causes for enhanced recombination and thus for limitations of open-circuit voltages and power-conversion efficiencies of Cu(In,Ga)Se_2 thin-film solar cells [29, 142]. However, it should be noted that all scanning probe microscopy measurements probe the grain boundaries and their surrounding materials only at the first monolayers of the Cu(In,Ga)Se_2 thin films. This is, scanning probe microscopy techniques are highly surface sensitive, also when applied on fractured cross-sections of Cu(In,Ga)Se_2 solar-cell stacks [143]. This issue will be treated again further below in the present chapter, when discussing the electrical properties of various extended structural defects in Cu(In,Ga)Se_2 thin films.

The remaining issue is nonradiative recombination, reducing the open-circuit voltage but also influencing the short-circuit current and the fill factor (see the corresponding items above). In the compound semiconductor Cu(In,Ga)Se_2, with rather

low net doping of $10^{15} - 10^{16}$ cm^{-3} and thus rather small contribution of Auger recombination, the SRH recombination has been identified as dominant nonradiative recombination process [15], which occurs via defect states in the band gap. Regarding the energy-band diagram, the closer the defect state is to the midgap position, the higher is the recombination rate R_{SRH}. According to Siebentritt [29], up to 7% absolute in power-conversion efficiency may be gained when shifting the nonradiative recombination further to radiative recombination in the quasi-neutral region of the solar cell, with a diode-ideality factor n_{id}=1 and a saturation current density closer to $j_{0,\mathrm{rad}}$ (Eq. 2.4). Thus, reducing nonradiative recombination in Cu(In,Ga)Se_2 solar cells represents a great potential of improving the power-conversion efficiencies towards 25% and beyond.

Nonradiative (SRH) recombination is generally connected to corresponding processes at interfaces within or between individual layers, especially at the interface between the p and the n layer forming the junction of the solar cell (since there, n equals p, thus, the recombination rate is maximum), as well as at extended structural defects. While nonradiative recombination at interfaces between individual layers can be reduced by designing chemically these interfaces (i.e., by adjusting the growth parameters of the corresponding thin films), the structural quality of the solar absorber and corresponding contributions to nonradiative recombination is often taken for granted. Therefore, there is a substantial necessity of enhanced understanding of not only which properties extended structural defects in Cu(In,Ga)Se_2 thin films exhibit and how they (possibly) influence the device performance, but also how these structural defects form during growth and how the microstructure can be controlled by choosing an appropriate set of growth parameters during the Cu(In,Ga)Se_2 thin-film growth.

5.2 Point defects

Since the present work focuses on linear, planar, and three-dimensional defects, the section on point defects in Cu(In,Ga)Se_2 will be kept rather short. Overviews on this topic were provided by Cahen [144], Burgelman et al. [145], Zunger [146], Rau and Schock [147], Rockett [148], and Siebentritt et al. [149].

Doping of Cu(In,Ga)Se_2 is due to intrinsic defects, while it is a highly compensated compound semiconductor. Cu(In,Ga)Se_2 with p-type conductivity is obtained if grown with [Cu]/([In]+[Ga])<1 and under high Se vapour pressure [150, 151]. In p-type Cu(In,Ga)Se_2 applied for high-efficient solar cells, the Cu vacancy V_{Cu}^{-} is considered the dominant acceptor, and the Se vacancy V_{Se}^{2+} the main, compensating donor [152]. Antisite In_{Cu}^{2+} and Ga_{Cu}^{2+} as well as Cu_{In}^{2-} and Cu_{Ga}^{2-} are further native donors and acceptors in Cu(In,Ga)Se_2. Impurity diffusion from diffusion across the heterojunction interface between Cu(In,Ga)Se_2 and various buffer layers such as CdS and Zn(O,S) may lead to the formation of further donors Cd_{Cu}^{+} and Zn_{Cu}^{+}. The point defects Na_{Cu}, K_{Cu}, S_{Se}, and O_{Se}, induced by impurity diffusion from the buffer layers given above or also from the soda-lime glass substrate, are quasi-neutral but result in the formation of weak donors and weak acceptors because of the different electronegativities of S, O, and Se as well as of Na, K, and Cu [153].

5.3 Line defects: dislocations

The present section gives an overview about the microstructural, compositional, and electrical properties of dislocations in Cu(In,Ga)Se_2 thin films for solar cells. At the end of this section, a structural model for these dislocation is proposed. The results given below are based on the following publications:
- J. Dietrich, D. Abou-Ras, T. Rissom, T. Unold, H.-W. Schock, C. Boit, "Compositional gradients in Cu(In,Ga)Se_2 thin films for solar cells and their effects on structural defects", J. Photovolt. 2 (2012) 364-370, doi: 10.1109/JPHOTOV.2012.2190584.
- J. Dietrich, D. Abou-Ras, S.S. Schmidt, T. Rissom, T. Unold, O. Cojocaru-Mirédin, T. Niermann, M. Lehmann, C.T. Koch, C. Boit, "Origins of electrostatic potential wells at dislocations in polycrystalline Cu(In,Ga)Se_2 thin films" J. Appl. Phys. 115 (2014) 103507-1-12; doi: 10.1063/1.4867398.

5.3.1 Structural properties

While dislocations are recognized in transmission electron microscopy images acquired on Cu(In,Ga)Se_2 thin films, only very few systematic reports are available on the properties of these line defects formed in Cu(In,Ga)Se_2 (bulk) crystals. Various reports on dislocations in strained chalcopyrite-type single crystals [154–159] and in Xe-ion-implanted $CuInSe_2$ thin films [160] do not give a clear picture on Burgers and dislocation line vectors in chalcopyrite-type crystal lattices. Overall, various values have been published.

The currently only available detailed dislocation analysis on polycrystalline Cu(In,Ga)Se_2 thin films in high-efficient solar cells [161] reports 60° configurations for dislocations in Cu(In,Ga)Se_2 thin films, as evidenced by high-resolution transmission electron micrographs (Fig. 5.5), with Burgers vectors of $\overrightarrow{b}_{60°} = \frac{1}{4}[201]$ and [110] dislocation lines (the notation is due to a (nearly) 60° angle between [201] and [110] vectors in tetragonal Cu(In,Ga)Se_2 crystal structures. This is, the dislocations in Cu(In,Ga)Se_2 thin films exhibit both, edge and screw contributions, with an introduced $\{11\bar{2}\}$ half-plane, similar to dislocations found in deformed Si crystals [162].

For the dislocation core in a Cu(In,Ga)Se_2 crystal, two different configurations are expected (see Fig. 5.6). Either the dislocation core consists of an atomic column of Cu, In, and Ga, or one containing only Se. Since the cations (Fig. 5.6a) and anions (Fig. 5.6b) in the dislocation core are not compensated, a residual charge resides at the atomic lattice sites. This situation is not stable, and we will see further below which mechanisms are available in the $CuInSe_2$ crystal to lower the total energy and thus to achieve a stable equilibrium condition.

As in Si crystals, it may be energetically favorable for a dislocation in a Cu(In,Ga)Se_2 thin film to dissociate (see Section 3.2), resulting in a 30° and in a 90° partial dislocation, with a corresponding stacking fault bound between them (see Fig. 5.7 for a corresponding transmission electron micrograph):

$$\overrightarrow{b}_{60°} = \overrightarrow{b}_{30°} + \overrightarrow{b}_{90°}$$
$$\frac{1}{4}[201] = \frac{1}{12}[421] + \frac{1}{6}[1\bar{1}1]$$

Again, the notation is due to 30° and 90° angles between [421] / $[1\bar{1}1]$ and the [110] dislocation core. An overview of possible partial dislocations in chalcopyrite-type crystals is given in Ref. [158]. The enthalpy of the dissociation of dislocations, also

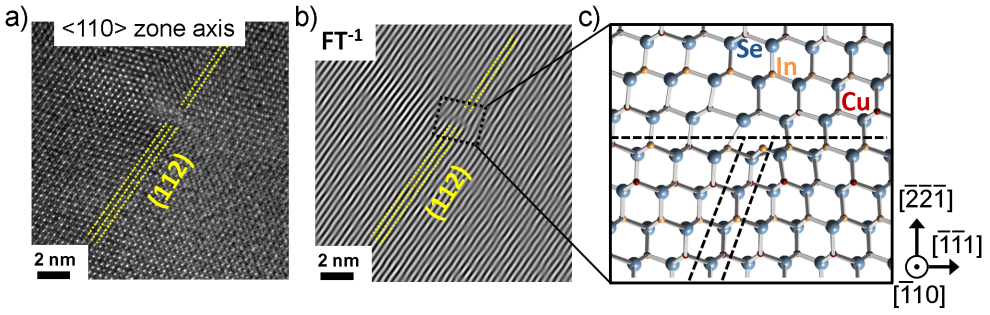

Figure 5.5: (a) High-resolution transmission electron micrograph of a Cu(In,Ga)Se_2 crystal oriented in [110] orientation, exhibiting a dislocation. The corresponding {112} lattice planes are highlighted by yellow lines. (b) Improved visibility of the dislocation is provided by allowing only electrons diffracted at (112) and at ($\bar{1}\bar{1}2$) lattice planes to contribute to the micrograph (by masking of corresponding reflections in the Fourier transform (FT) of the micrograph). (c) Model for 60° dislocation, with inserted {11$\bar{2}$} half-plane. From Ref. [161], TEM image acquired by Dr. Tore Niermann, TU Berlin.

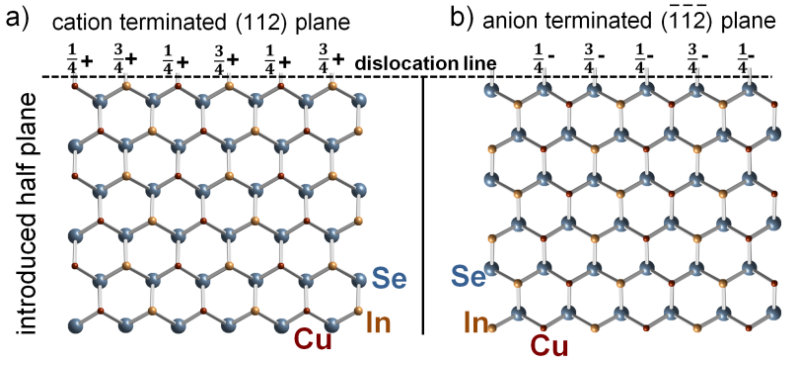

Figure 5.6: Structural representations for dislocation cores in a $CuInSe_2$ crystal. Either the dislocation core consists of an atomic column of Cu and In (a), or one containing only Se (b). The residual charges at the sites of the various atomic columns in the lattice are indicated. From Ref. [161].

identified with that of the formation of a stacking fault, is larger for $Cu(In,Ga)Se_2$ (about 0.8-3 J/m^2 [163]) than for Si crystals (about 50 mJ/m^2 [162]). To our experience, the frequency of dissociated dislocations in $Cu(In,Ga)Se_2$ thin films and also that of stacking faults is therefore rather low, in contrast to Si crystals, in which such dissociations are found more frequently.

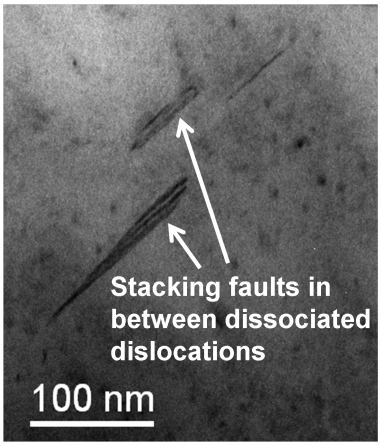

Figure 5.7: Bright-field transmission electron micrograph of a $Cu(In,Ga)Se_2$ crystal containing two dissociated dislocations (not visible), which are bound to stacking faults.

5.3.2 Spatial distributions of dislocations and correlation with compositional gradients

Generally, no homogeneous distributions of dislocation densities in $Cu(In,Ga)Se_2$ thin films have been found. While in some grains, not any dislocations can be identified in transmission electron micrographs, in other grains, these line defects exhibit densities of as high as $10^{10} - 10^{11}cm^{-2}$ [164].

High densities of dislocations within individual grains in a $Cu(In,Ga)Se_2$ thin film has recently been correlated directly to large spatial changes of the [Ga]/([Ga]+[In]) compositional ratio [164]. Fig. 5.8 shows a bright-field transmission electron microscopy (BF-TEM) image with a highlighted single large grain and energy-dispersive X-ray spectrometry (EDX) elemental distribution maps of Cu, Ga and In of the identical area. By means of dark-field TEM images (not shown here), it was evidenced that the highlighted area is one contiguous grain. The highlighted grain in Fig. 5.8a shows a dislocation distribution that consists of a part with a high dislocation density close to the Mo back contact (visible by dark lines) and a part with a significantly lower dislocation density in the middle part of the $Cu(In,Ga)Se_2$ layer. In the part close to the Mo back contact, the dislocation density was estimated to about $10^{10}cm^{-2}$, by a method introduced by Steeds [165]. Within the accuracy of the EDX measurement (approximately 1 at.%), the $Cu(In,Ga)Se_2$ thin films do not show any compositional inhomogeneities parallel to the substrate, neither inside the grains nor in the vicinity of the grain boundaries. In contrast, the Ga and In distribution maps in Fig. 5.8b-d indicate that the Ga and In concentrations vary perpendicular to the glass substrate, also within this individual grain. Such a scenario was found equally for various other

large grains (with diameters of more than 1 μm). In smaller grains, the presence of dislocations is less likely due to the high densities of grain boundaries, which may compensate for strain.

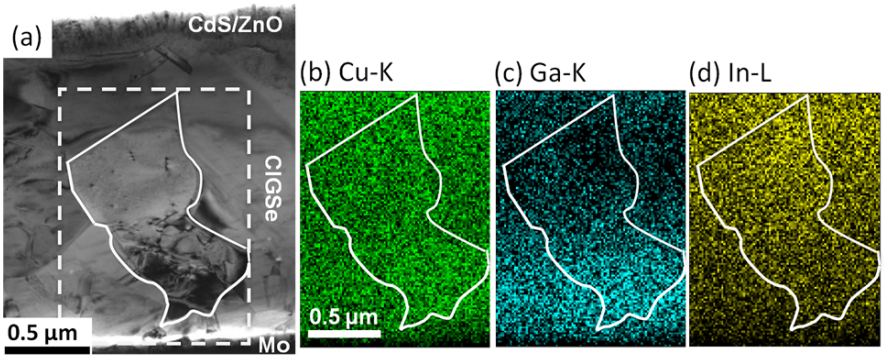

Figure 5.8: Cross-sectional, bright-field TEM image of a ZnO/Cd/Cu(In,Ga)Se_2/Mo/glass stack (a). A single, large grain is highlighted by a solid white line, and the area of the EDX mapping by a dashed white line. EDX elemental distribution maps are composed of Cu-K (b), Ga-K (c), In-L signals (d). From Ref. [164]

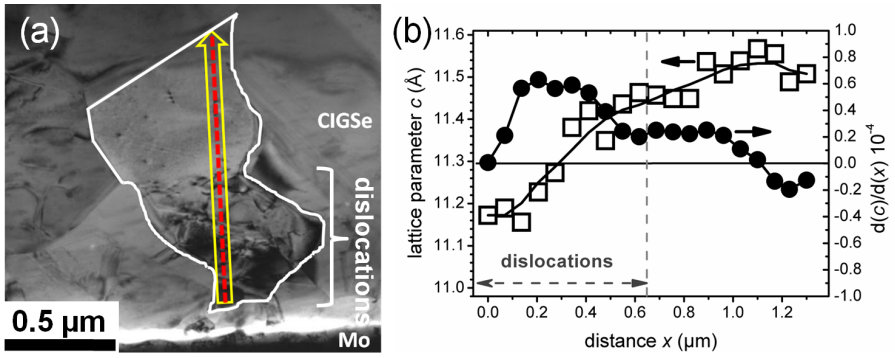

Figure 5.9: Bright-field TEM image of the large grain displayed in Fig. 5.8a. The yellow arrow with the red dashes represents the extracted linescan of a TEM-EDX mapping with 20 data points. The lattice parameter c with the first derivative $\mathrm{d}c/\mathrm{d}x$ are plotted (b) over the distance x. Reproduced from Ref. [164]

A linescan (yellow arrow in Fig. 5.9a) perpendicular to the substrate inside the grain displayed in Fig. 5.8a was extracted from the EDX elemental-distribution maps (Figs. 5.8b-d). Assuming that the microstrain is negligible, the Ga concentrations from this linescan and the lattice parameters for polycrystalline Cu(In,Ga)Se_2 thin films with various integral Ga concentrations, given in the literature [166], were used to calculate the spatial distributions of the lattice parameters c and a. In order to obtain a value for the gradient of the change in lattice parameters, the first derivative $\mathrm{d}c/\mathrm{d}x$ was calculated. The lattice parameter c and $\mathrm{d}c/\mathrm{d}x$ were plotted over the distance x of the linescan in Fig. 5.9b. The area where dislocations are identified in the TEM

image is highlighted by grey dashed lines in Fig. 5.9b. It is apparent that the large dislocation densities are present in the region around the maximum of $\mathrm{d}c/\mathrm{d}x$.

Based also on results from similar analyses on various Cu(In,Ga)Se_2 thin films, a threshold value of $\mathrm{d}c/\mathrm{d}x$ of 3x10^{-5} was estimated for the presence of high densities of dislocations ($10^{10} - 10^{11}\mathrm{cm}^{-2}$), which separates corresponding regions in large grains from those areas free of apparent lattice defects. This value can also be considered as threshold between the elastic and the plastic deformation regime for the Cu(In,Ga)Se_2 crystal structure. The value of $\mathrm{d}c/\mathrm{d}x$=3x10^{-5} can be transformed into changes of 12-13 at.%/μm in Ga concentration or into a strain of about 1.4 %/μm as corresponding threshold values.

5.3.3 Origin of electrostatic potential wells at dislocations

Distributions of average electrostatic potential around dislocations

Potential wells were obtained at various dislocations located within the studied Cu(In,Ga)Se_2 layer. The minimum values of the average electrical potential within the well, $\Delta V_{\mathrm{av}}^{\mathrm{min}}$, did not exhibit dependencies on the positions of the dislocations in the Cu(In,Ga)Se_2 layer (close to the interface with the CdS buffer layer or close to the Mo back contact). Examples are given in Fig. 5.10. It is apparent that the values for the local minima of the potential wells $\Delta V_{\mathrm{av}}^{\mathrm{min}}$ in Figs. 5.10b and d are different.

In order to evaluate the potential distributions around the line of a dislocation correctly, few issues need to be considered. Other than a grain boundary, which is still visible when oriented edge-on for inline electron holography, the dislocation line is not detectable easily any more in a focused, medium-resolution TEM image when tilted to end-on orientation, i.e., parallel to the electron beam. For such an orientation, identification of dislocations is difficult. Therefore, various dislocations with different orientations of dislocation cores relative to the surface normal of the TEM lamella were investigated.

In order to compare various analyzed dislocations, the changes of the potential ΔV_{av} are modeled to stem from a cylinder of radius R with a constant potential V (Fig. 5.11). This is a simplified model (concept adepted from Ref. [167]), which we only use to compare the dislocations independent from their individual orientation. The dislocation cylinder depends on the orientation of the dislocation core in the TEM lamella. The total thickness of this lamella is given by $t(x, y)$. The diameter $2R$ of the dislocation cylinder can be determined from the width of the measured potential wells.

The measured phase shift $\Delta\phi(x, y)$ is then composed of the difference in average electrostatic potential $\Delta V_{\mathrm{av}}^{0}(x, y)$ within the defect-free layer with thickness $t - 2R$ (where t is here an average thickness of $t(x, y)$ over all x and y values) and of the difference in electrostatic potential at the dislocation core, $\Delta V_{\mathrm{disloc}}$ with extension $2R$:

$$\begin{aligned}\Delta\phi(x, y) &= \sigma t(x, y)\Delta V_{\mathrm{av}}(x, y) \\ &= \sigma\left[\left(t(x, y) - 2R\right)\Delta V_{\mathrm{av}}^{0}(x, y)\right] + 2R\Delta V_{\mathrm{disloc}}(x, y).\end{aligned} \tag{5.3}$$

Since the difference in average electrostatic potential $\Delta V_{\mathrm{av}}^{0}(x, y)$ within the defect-free layer can be considered zero, Eq. 5.3 simplifies to, when solved for $\Delta V_{\mathrm{disloc}}(x, y)$:

$$\Delta V_{\mathrm{disloc}}(x, y) = \frac{1}{\sigma}\frac{\Delta\phi(x, y)}{2R}. \tag{5.4}$$

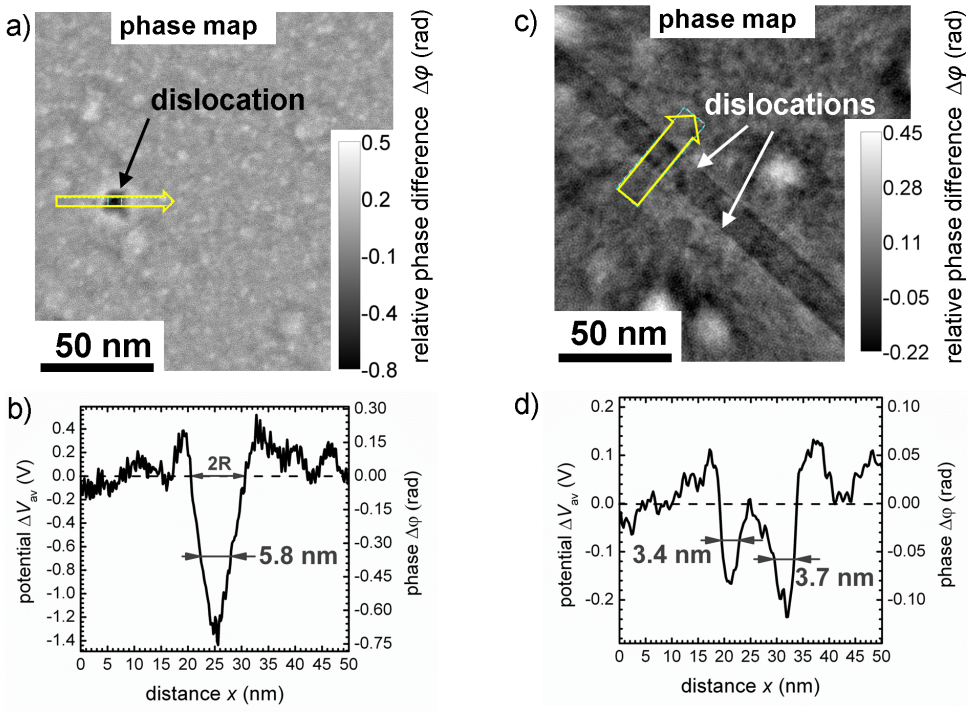

Figure 5.10: a) Spatial variations of the phase of the reconstructed exit-plane electron wave function around a dislocation in Cu(In,Ga)Se_2 oriented parallel to the incident electron beam. The yellow arrow indicates the extracted profile of variations in phase and average electrostatic potential given in (b). c) Spatial variations of the phase of the reconstructed exit-plane electron wave function around a dissociated dislocation orientated perpendicular with respect to the electron beam and d) the corresponding extracted line scan with the plotted phase and electrostatic potential. The value $\Delta V_{\mathrm{av}} = 0$ V was set within the volume of the grain.

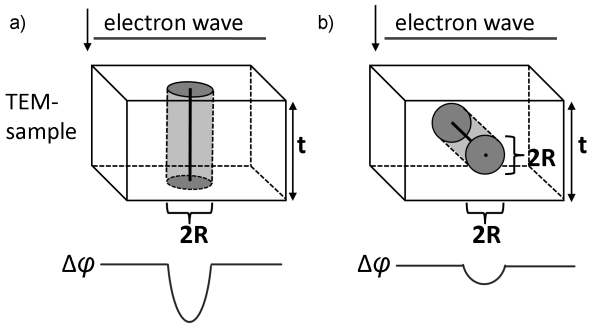

Figure 5.11: Schematics of dislocations oriented a) parallel and b) perpendicular with respect to the incident electron beam. The phase of exit-plane electron wave, $\Delta\phi(x, y)$, varies around the dislocation. The diameter $2R$ of the dislocation cylinder is determined by the width of the well in the phase profile $\Delta\phi(x, y)$ across the dislocation.

In the following, we will consider only undissociated dislocations. Out of 18 investigated dislocations in the Cu(In,Ga)Se_2 layer, 10 exhibited potential wells, which are summarized in Table 5.2. Interestingly, at the other 8 dislocations, no considerable change above noise level was detected in the phase distributions. This results will be discussed further below in section 5.3.3.
The average value and the standard deviation for the local minimum $\Delta V_{\mathrm{disloc}}^{\mathrm{min}}$ results to (-1.4±0.2) V. It is remarkable that the variations of $\Delta V_{\mathrm{disloc}}^{\mathrm{min}}$ between the individual dislocations are quite small. This fact indicates similar origins for the potential wells measured at the different dislocations. The full widths at half maximum of the potential wells are between 2-8 nm.

Table 5.2: The minimum values of the variations in the phase, $\Delta\phi^{\mathrm{min}}$, and in the average electrostatic potential $\Delta V_{\mathrm{av}}^{\mathrm{min}}$, the full width at half maximum (FWHM), the diameter $2R$ of the dislocation cylinder, the thickness t of the TEM lamella, and the spatial variations in averaged electrostatic potential at the dislocation core, $\Delta V_{\mathrm{disloc}}^{\mathrm{min}}$, for 10 undissociated dislocations. Also given are the orientations of the dislocations with respect to the lamella surface (|: perpendicular, -: parallel, /: intermediate inclination between parallel/perpendicular.

Dislocation number	$\Delta\phi^{\mathrm{min}}$ (rad)	$\Delta V_{\mathrm{av}}^{\mathrm{min}}$ (V)	FWHM (nm)	$2R$ (nm)	t (nm)	$\Delta V_{\mathrm{disloc}}^{\mathrm{min}}$ (V)	Orientation
1	-0.64	-1.3	5.8	10	70	-1.3	|
2	-0.10	-0.29	3.3	8	48	-1.7	/
3	-0.11	-0.21	4.0	11.5	76	-1.3	/
4	-0.13	-0.24	6.0	11.5	76	-1.6	/
5	-0.10	-0.18	7.8	11.5	76	-1.2	/
6	-0.08	-0.14	4.5	8.5	76	-1.3	/
7	-0.08	-0.15	7.5	10	76	-1.1	/
8	-0.08	-0.11	4.3	8	108	-1.4	/
9	-0.11	-0.21	2.8	12	72	-1.3	/
10	-0.15	-0.26	4.1	11	80	-1.9	-

In the following, various possible origins for the potential wells obtained by inline electron holography will be discussed.

Possible origins of potential wells at dislocations

Strain field around dislocation Strain fields may influence the average electrostatic potential according to Eqs. 4.5 and 4.4 since the MIP depends on the local volume of the unit cell, Ω. In order to investigate the influence of strain fields around dislocations, the displacement field of atomic positions in a $CuInSe_2$ lattice around a dislocation was determined using the anisotropic, elastic description provided by Steeds [61]. Details on the exact procedure can be found in Ref. [88]. The resulting $CuInSe_2$ lattice in [110] orientation with a 60 ° dislocation and the dislocation core perpendicular to the image plane is given in Fig. 5.12a.

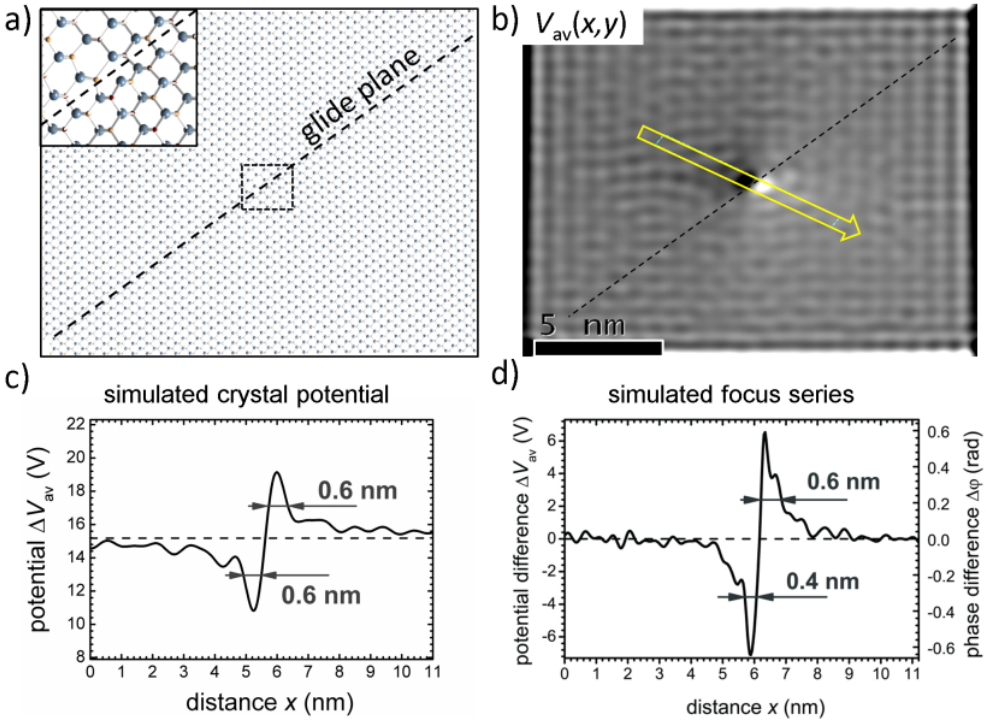

Figure 5.12: (a) Calculated $CuInSe_2$ lattice in [110] orientation around a 60 ° dislocation with inserted $(11\bar{2})$ half plane, determined using the anisotropic, elastic description provided by Steeds [61]. The total lattice exhibits a volume of 17.7 x 12.5 x 13.8 nm^3 and about 120'000 atoms. (b) The average electrostatic potential V_{av} is simulated by the software QSTEM [168] for a crystal tilt of 1°. The yellow arrow gives the position of the extracted linescan shown in c). At the borders of the potential distribution, boundary effects are visible. d) Profile of the variations in phase $\Delta\phi$ and ΔV_{av} across the dislocation, obtained by a through-focus series (inline electron holography) of the $CuInSe_2$ lattice in (a), performed by use of the software QSTEM.

Using this $CuInSe_2$ lattice, the spatial distributions of phase and amplitude around the dislocation for an electron wave travelling through this lattice was calculated using the software QSTEM [168], which applies a multislice algorithm. In order to reduce dynamical effects, the crystal was tilted to 1 ° for the simulation. From the phase distribution, the distribution of the average electrostatic potential was determined using Eq. 4.1. The corresponding spatial distribution is given in Fig. 5.12b, and an extracted linescan (along the arrow in b) in Fig. 5.12c.
Moreover, a through-focus series of TEM images was simulated using the QSTEM software and the lattice in Fig. 5.12a. This series contains 15 individual images with varying defocus between ± 490 nm (step size 70 nm). This maximum defocus is limited by the size of the $CuInSe_2$ lattice used. For larger defocus values, boundary effects of the crystal model dominate the simulated TEM image. Experimentally, a much larger defocus step of about 800 nm was used.
From this through-focus series, the spatial variations in phase and amplitude around the dislocation were calculated, as performed in inline electron holography with experimentally obtained focus series. A corresponding distribution of spatial variations in the average electrostatic potential were determined using Eq. 4.1. A linescan across the dislocation extracted from this distribution is given in Fig. 5.12d. Apparently, this linescan is similar to the one of the average electrostatic potential in Fig. 5.12c. These linescans reflect the strain field around the dislocation core due to the change in atomic density. Due to locally larger/smaller atomic densities in the lattice, local maxima/minima in the potential distributions at the dislocation core are visible in the simulations. Both distributions in Figs. 5.12c and d exhibit rather small full widths at half maxima/minima of only about 0.6 nm, which is substantially smaller than the corresponding values of about 2-8 nm for the potential wells obtained experimentally. It should be noted that these local maxima/minima are present only in the simulated linescans and not in the experimental results since in general, the dislocation core may be oriented with respect to the incident electron beam in such a way that the local maxima and minima cancel each other (at least in part). In conclusion, the results given in Figs. 5.12c and d show that strain fields may contribute to a small extent to the measured potential wells but are not sufficient to explain fully their presence.
We note that in contrast to the dislocations analyzed in the present work, the lower atomic density at a twin boundary containing a dislocation core, owing to corresponding "gaps" in the atomic structure, has indeed been shown to explain (in part) a local minimum in the average electrostatic potential [169].

Charge density at dislocations Since the dislocation core in a $Cu(In,Ga)Se_2$ crystal contains either only Se^{2-} ions (also Se atoms) or cations (Cu^+, In^{3+}, and Ga^{3+}, also Cu, In, and Ga atoms), see Fig. 5.6, it can be expected to exhibit a negative or a positive charge density. This charge density and possible compensating charges contribute to the average electrostatic potential via $\Delta V_{\mathrm{charge}}(x,y)$ in Eq. 4.4, which is connected to the spatial distribution of charges $\rho(x,y)$ via Poisson's equation $\overrightarrow{\nabla}^2 V_{\mathrm{charge}}(x,y) = -\rho(x,y)/\epsilon_0\epsilon_r$, where ϵ_0 and ϵ_r are the vacuum and relative permittivity. In the following, the cases of positive and negative excess charge at dislocation cores will be treated separately.

1. Negative line-charge density screened by free holes in *p*-type $Cu(In,Ga)Se_2$:
   This case would lead indeed to potential wells as measured by means of inline electron holography in the present work. Poisson's equation can be solved, using cylinder coordinates and assuming charge compensation only by the majority

charge carriers in the p-type Cu(In,Ga)Se_2 layer, to [88]

$$V_{\mathrm{charge}}(x,y) = \frac{q_{\mathrm{L}}}{2\pi\epsilon_0\epsilon_r} K_0\left(\frac{|\overrightarrow{r}|}{L_{\mathrm{Debye}}}\right). \tag{5.5}$$

Here, q_{L} is the line charge along the dislocation core, $K_0(\xi)$ the modified Bessel function of second kind and of zero order of the argument ξ, and $\overrightarrow{r} = (x,y)$. It is assumed that $\Delta V_{\mathrm{charge}}(x,y) < k_{\mathrm{B}}T$. The Debye screening length L_{Debye} can be written as

$$L_{\mathrm{Debye}} = \sqrt{\frac{k_{\mathrm{B}}T\epsilon_0\epsilon_r}{e^2 N_{\mathrm{A}}}},$$

where N_{A} is the acceptor density and also the effective net doping in Cu(In,Ga)Se_2, assuming that all acceptor states are ionized at room temperature. For Cu(In,Ga)Se_2, typically values of about $10^{15} - 10^{16}$ cm^{-3} have been reported [170, 171].

For the calculation of V_{charge} in Eq. 5.5, N_{A} was set to 1×10^{16} cm^{-3}, and ϵ_r to 11.3 for $CuInSe_2$ [172], resulting in $L_{\mathrm{Debye}} = 40$ nm. The contribution of a negative charge density at the dislocation core to the average electrostatic potential, V_{charge}, was plotted in Fig. 5.13 for $q_{\mathrm{L}} = -1$ and -5 e/nm. In order to get comparable results for the experimental data and the simulated potential distribution, a band-pass filter was applied to both curves. The upper cut-off frequency is the size of the objective aperture (1.2 1/nm). The lower cut-off frequency is related to various sources, as, e.g., the noise in the acquired image, or to the accuracy of the focal spacings within the through-focus series [173]. This lower value of the band filter can not be determined precisely but was estimated from the measured phase information to 0.01 1/nm. As lower detection limit, a value of $q_{\mathrm{L}} = 0.1$ e/nm can be estimated, assuming the noise level for the measured potential distributions of about 0.1 V and $N_{\mathrm{A}} = 1 \times 10^{16}$ cm^{-3}.

There is a good agreement of the calculated, filtered potential distribution and the potential well obtained experimentally only for $q_{\mathrm{L}} = $ -5 e/nm. Considering a p-type Cu(In,Ga)Se_2 layer with a band-gap energy $E_{\mathrm{g}} = 1.2$ eV, for which the Fermi level is below the midgap position, a line charge density of $q_{\mathrm{L}} = $ -5 e/nm would result in a band bending of $-e\ V_{\mathrm{charge}} = 1.4$ eV, which is in the order of the band-gap energy. The valence band would be bent to more than $E_{\mathrm{g}}/2 = 0.6$ eV above the Fermi level, charging the semiconductor way up into the band, leading to very large density of states. Therefore, similar to a strain field, excess charge may contribute to a small extent to the measured potential wells but is not sufficient to explain fully their presence.

2. Positive line-charge density: In a p-type semiconductor, positive excess charge at the dislocation core would lead to increased average electrostatic potential, and not to potential wells. However, it is still important to estimate a possible influence of positive charge densities to the background noise of the measurement. According to Read [174], a positively charged dislocation line in a p-type material is screened by a depletion zone around the dislocation. The corresponding screening radius R results from the balance of the line charge density q_{L} and the ionized acceptor density N_{A} in the volume around the dislocation core:

$$R = \sqrt{\frac{q_{\mathrm{L}}}{\pi N_{\mathrm{A}}}}.$$

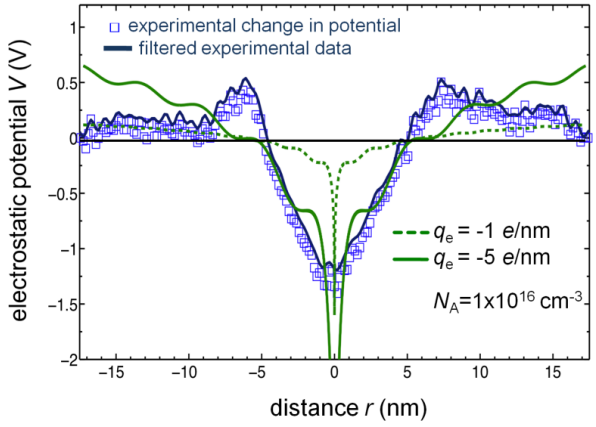

Figure 5.13: A negative, linear charge density in a p-type semiconductor leads to a negative screening potential (by free holes), see Eq. 5.5. This potential distribution is plotted for an acceptor density of 1×10^{16} cm^{-3} and for line charge densities of $q_{\mathrm{L}} = -1$ and -5 e/nm. For comparison, the measured change in potential Fig. 5.10b is given (blue graph). The position of dislocation core is set to the distance of $r = 0$. A band-pass filter with 0.01 nm^{-1} lower and 1.2 nm^{-1} upper cut-off frequency was used in the simulation to comply with the size of the objective aperture and with the information limit in the experimental setup.

The potential distribution can then be written as (with $|\overrightarrow{r}|^2 = x^2 + y^2$)

$$V_{\mathrm{charge}}(x,y) = \frac{q_{\mathrm{L}}}{4\pi\epsilon_0\epsilon_r}\left[\ln\left(\frac{|\overrightarrow{r}|^2}{R^2}\right) - \frac{|\overrightarrow{r}|^2}{R^2} + 1\right]. \tag{5.6}$$

If we set again $N_{\mathrm{A}} = 1 \times 10^{16}$ cm^{-3} in Eq. 5.6, the noise level for the potential measurements of 0.1 V would lead (as also given above for the negatively charged dislocations) to a maximum line charge density q_{L} of about 0.1 e/nm. Therefore, the corresponding potential distribution $V_{\mathrm{charge}}(x,y)$ has a negligible influence on the measured potential wells.
However, a value of $q_{\mathrm{L}} < 0.1$ e/nm can be translated into an average distance between free holes at the dislocation core of about 10 nm. From the net doping density of $N_{\mathrm{A}} = 1 \times 10^{16}$ cm^{-3}, an average distance between free holes within the bulk of the Cu(In,Ga)Se$_2$ crystal of about 46 nm can be calculated. This means, the possible charge densities at the dislocation core below the detection limit of the inline electron holography would be about 4 times larger than that in the volume of the Cu(In,Ga)Se$_2$ thin film. Therefore, this fact has to be taken into account when discussing electrical properties of dislocations in Cu(In,Ga)Se$_2$ further below.

Compositional changes at dislocations Finally, also changes in composition at or around the dislocation can influence average electrostatic potentials via the differences in MIP, i.e., Ω and $f_j^{\mathrm{el}}(0)$, in Eqs. 4.5 and 4.4. We have performed compositional measurements across dislocations in Cu(In,Ga)Se$_2$ thin films by (scanning) TEM, but have not yet succeeded in determining unambiguously the composition of dislocation cores. To date, the only results giving corresponding information have

been obtained by means of atom-probe tomography (APT), which is a mass spectroscopy providing three-dimensional insight into a specimen with high spatial resolutions of down to about 1-2 nm. In Fig. 5.14, a reconstructed, three-dimensional APT data cube is depicted, which gives the Na distribution within a section of a polycrystalline Cu(In,Ga)Se_2 thin film. Na typically segregates to extended structural defects, when diffusing from the soda-lime glass substrate into the Cu(In,Ga)Se_2 thin film (see, e.g., [175–177]). The Na signal is enhanced at various positions: within a planar feature, which is identified as a grain boundary, and within two lines, which can be related to dislocation cores.

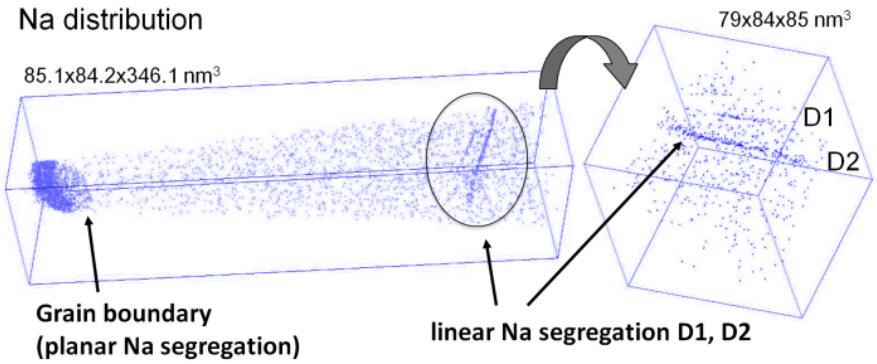

Figure 5.14: Reconstructed, three-dimensional APT data cube of a Cu(In,Ga)Se_2 crystal exhibiting the Na distribution across the crystal. The Na signal is enhanced within a plane, which is identified as a grain boundary, as well as within two linear features, which can be related to dislocation cores.

Fig. 5.15 shows linescans extracted from the APT data around one of the linear features (D1 in Fig. 5.14). Local maxima are visible in the Na and K signals, while the Cu signal is reduced considerably. Moreover, the Na and Cu signals exhibit different full widths at half maximum/minimum of 1.5 and 3 nm. In contrast, the In, Ga, and Se signals do not change substantially within the errors of measurement, and the O signal remains below the noise level throughout the measured specimen volume. We note that the elemental distributions around the linear feature D2 in Fig. 5.14 are similar.

It should be mentioned that up to date, only very few APT data cubes actually exhibit linear features with compositional changes. Therefore, the statistics on elemental distributions across dislocations is very poor. Nonetheless, these linear features can be distinguished well from stacking faults, microtwins, and grain boundaries, which are planar defects and hence exhibit changes in composition along a plane in the APT data cube.

The elemental concentrations for Cu, In, Ga, and Se in the volume of the Cu(In,Ga)Se_2 crystal were determined to 25, 20, 8, and 47 at.% by means of APT. We note here that these values differ slightly from the values measured by means of X-ray flurorescence analysis on the Cu(In,Ga)Se_2 thin film, which are 23, 18, 8, and 51 at.% (the differences between the compositional measurements show that corresponding errors can be estimated to 1-2 at.%, depending on the element). At the dislocation core, the Cu concentration is decreased to about 18 at.%. The corresponding change in MIP was calculated from the change in the Cu concentration across the dislocation core using Eq. 4.5, neglecting changes in the unit-cell volume Ω. Atomic scattering factors

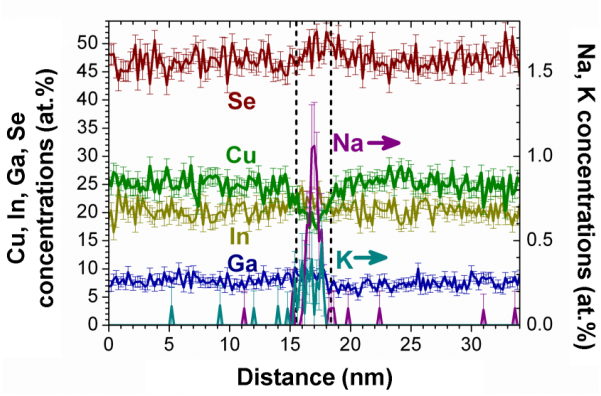

Figure 5.15: Elemental distribution across the linear Na segregation in a Cu(In,Ga)Se_2 thin film, marked as D1 in Fig. 5.14. Local maxima are visible in the Na and K signals, where also the Cu signal is reduced considerably. The local minimum in the Cu distribution exhibits a larger width than the maximum in the Na distribution. The In, Ga, and Se signals do not change substantially across the dislocation. The O signal remains below the noise level throughout the measured specimen volume.

reported by Refs. [178–180] were used. A band-pass filter with 0.01 nm^{-1} lower and 1.2 nm^{-1} upper cut-off frequency was applied in the simulation to comply with the size of the objective aperture and with the information limit in the experimental setup.

It should be noted at this point that no values for the scattering factor $f_j^{el}(0)$ of Se^{2-} are available in the literature. Therefore, only atomic and not ionic scattering was considered in the present work. However, one may still regard the influence on the MIP of the ionicity of Cu. A neutral Cu atom exhibits a scattering factor of 0.629 nm, while Cu^+ and Cu^{2+} ions of 0.312 and 0.265 nm [178–180]. This is, the calculated reduction in the MIP would be smaller the higher the ionicity of the Cu.

Assuming only scattering at neutral atoms, the resulting distribution of MIP agrees very well concerning the width and the depth with the measured variation in average electrostatic potential from Fig. 5.10b, see Fig. 5.16. In the calculation of the change in MIP, the variations in Na and K are neglected since these compositional changes are only about 1 at.% and lower.

Changes in composition, represented mainly by a depletion in Cu, give the best agreement with the measured local minima in the distributions in the average electrostatic potential. It is assumed that this depletion in Cu is related entirely to the presence of V_{Cu}. Presence of In_{Cu} and Ga_{Cu} can be neglected owing to not any considerable change in the In and Ga signals at what has been identified as the dislocation core. It should be mentioned that compositional properties of dislocations have also been analyzed by means of high-resolution STEM imaging and EELS mapping. However, unambiguous results have not been obtained by these techniques up to now.

In the following section, we will see how the results presented above are translated into a structural model for dislocations in Cu(In,Ga)Se_2 thin films.

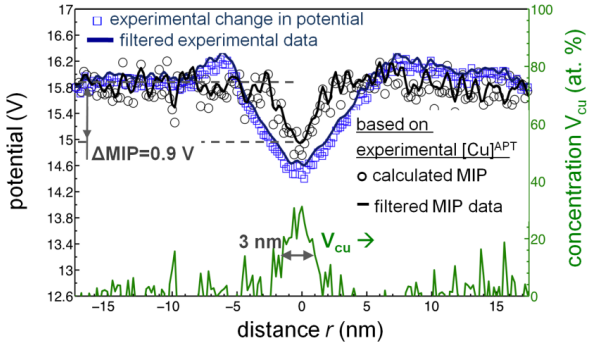

Figure 5.16: The MIP is calculated by use of Eq. 4.5 and of the elemental distributions obtained by means of APT (Fig. 5.15). The dislocation core is assumed to be at the minimum of the MIP (at r=0). For comparison, the measured change in potential (Fig. 5.10b) is given by open squares. A band-pass filter with 0.01 nm^{-1} lower and 1.2 nm^{-1} upper cut-off frequency was used in the simulation to comply with the size of the objective aperture and with the information limit in the experimental setup. The concentration of V_{Cu} is calculated by $(1 - [Cu]/25\ at.\%) \times 100\ at.\%$, assuming that the depletion in Cu is related entirely to the presence of V_{Cu} (and not, e.g., of In_{Cu}).

Proposed structural dislocation model and possible impact on photovoltaic device performance

As starting point, we take the structural representations of the inserted half planes given in Figs. 5.6a and b (termed cases a and b in the following). As outlined already above in Section 5.3.1, the dislocation cores in Cu(In,Ga)Se_2 thin films containing either cations (Cu^+, In^{3+}, and Ga^{3+}) or Se^{2-} ions exhibit positive or negative excess-charge densities. For cation-terminated and Se-terminated {112} surfaces of $CuInSe_2$ and $CuGaSe_2$ crystals, Persson and Zunger [181, 182] calculated by means of density-functional theory (DFT) that these excess-charge densities can be reduced by the formation of either Cu vacancies V_{Cu}^- (for cation termination) or by $In_{Cu}^{2+}/Ga_{Cu}^{2+}$ (for Se termination).

Such atomic reconstruction may also be assumed for the dislocation cores in Cu(In,Ga)Se_2 films, regarding them as "linear surfaces". The reconstruction only occurs either within the dislocation core (for cation termination), or in the line of cations neighboring the dislocation core (for Se termination), in analogy to Refs. [181, 182]. Apparently, that can not explain a Cu depletion with a width of a few nanometers and the measured potential wells.

Instead, the following mechanism is proposed (see Figs. 5.17a and b). As indicated by the APT results, the atomic reconstruction may be influenced by the presence of Na and K. We neglect the small concentration of K detected at the dislocation core for the following discussion. It is furthermore assumed that the reconstructions of the inserted half planes (Figs. 5.6a and b) are attended by Na segregation to the dislocation cores. We note that in Cu(In,Ga)Se_2 crystal, Na occupies preferably V_{Cu}^- and In_{Cu}^{2+} [183].

If we consider case (a) with a dislocation core containing only cations and V_{Cu}^- compensating the excess positive charge, Na is likely to occupy the Cu vacancies (because of similar ionic radii of Na and Cu), forming Na_{Cu} [183–185]. This process affects considerably the atomic reconstruction at the cation-containing dislocation core (case

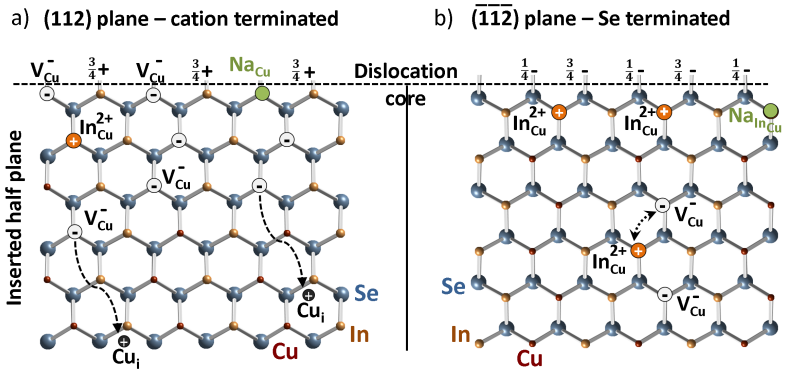

Figure 5.17: Structural models for the inserted half planes with dislocation cores in a $CuInSe_2$ lattice taking account atomic reconstruction, i.e., formation of either Cu vacancies V_{Cu} (for cation-containing) or by In_{Cu} (for Se-containing dislocation cores). In addition, Na (and K to minor extent) segregates to the dislocation core. (a) The reconstruction of the cation-containing dislocation core by formation of V_{Cu} is influenced by Na occupying Cu sites. This leads to excess positive charge and a field-induced Cu diffusion away from the dislocation. (b) The reconstruction of the Se-containing dislocation core by formation of In_{Cu} may be affected by Na occupying In_{Cu}. A similar scenario can be drawn for a $CuGaSe_2$ crystal.

(a)) and leads to a remaining positive line charge due to the dangling bonds (taking into account the concentrations of about 7 at.% of V_{Cu} and of about 1 at.% of Na measured by means of APT).

The positive excess charge is compensated by a field-driven Cu diffusion away from the dislocation core, resulting in a region of about 3 nm in width around the dislocation, within which Cu is depleted (see Fig. 5.17a). This proposed mechanism is probable because of the high mobility of Cu in the substoichiometric $Cu(In,Ga)Se_2$ compound [186], containing intrinsically a large concentration of V_{Cu} of up to few percentages.

The positive line charge density introduced by the presence of Na^+ ions (in addition to V_{Cu} compensating positive excess charge at the dislocation cores containing cations) should be sufficiently small to result in a negligible contribution to the average electrostatic potential. In Sec. 5.3.3, the corresponding value was estimated to $q_L < 0.1\ e/\mathrm{nm}$.

Regarding case (b) with a Se-containing dislocation core in Fig. 5.6b, the Cu sites in the cation line neighboring the dislocation are already occupied by In atoms. Although calculations by density-functional theory [183] suggest that Na is likely to reduce the density of $In_{Cu}^{2+}/Ga_{Cu}^{2+}$ defects by forming Na_{Cu} in the bulk of a $Cu(In,Ga)Se_2$ crystal, this is scenario would not explain a substantial decrease in the average electrostatic potential V_{av}.

If Na reduced all $In_{Cu}^{2+}/Ga_{Cu}^{2+}$ defects in the line of cations neighboring the Se-containing dislocation core, this would lead to a field-driven diffusion of In_{Cu}^{2+} defects away from the dislocation core. Regarding the resultant influences on the electrostatic potential of such an action, first, the ionic scattering factor of In_{Cu}^{2+} do not differ considerably from that of Cu (i.e., scattering factors of In^{3+} and of Cu are quite similar [178,180]). Secondly, the change in the atomic density by the substitution of Cu

by In would be negligible. Therefore, the measured potential wells do not correspond well to a scenario according to case (b) in Figs. 5.17b. Instead, the potential wells are explained best by the presence of a Cu depletion within a region of about 3 nm width around the dislocation core, which is related to the formation of Na_{Cu}, introducing a positive excess charge density, according to case (a).

We like to address again the result that out of 18 (not dissociated) dislocations, 10 exhibit electrostatic potential wells, all with depths of about -1.4 V and widths of 2-8 nm. Naturally, there may be various reasons why not any potential well is measured at the position of a dislocation. Based on the considerations in the previous paragraph, we propose the following scenario for dislocation cores in Cu(In,Ga)Se_2 thin films containing Na. The 10 dislocation cores with potential wells summarized in Table 5.3.3 contain only cations, according to case (a). For those 8 dislocations at which not any substantial change in average electrostatic potential was measured (within the resolution of about 0.8 nm), the cores contain only Se, see case (b).

Considering the two proposed structural dislocation models for Cu(In,Ga)Se_2 thin films, cases (a) and (b) depicted in Fig. 5.17, we briefly discuss possible influences on the power-conversion efficiency in the corresponding Cu(In,Ga)Se_2 solar cells. Regarding case (a), a Cu depletion as measured around the dislocation core by means of APT (possibly the origin of the measured potential wells) can be associated with a lowering of the valence-band maximum (VBM) in Cu(In,Ga)Se_2, as calculated by Persson and Zunger [181] by means of DFT. For this, we assume that the surface of a Cu(In,Ga)Se_2 crystal and the dislocation core, being the terminating atomic line of the inserted half plane, exhibit the same electronic properties and only differ in their dimensions (note that a grain boundary can be considered two surfaces connected one with the other, in a simplified model). The VBM of $CuInSe_2$ (and also of $CuGaSe_2$) consists of antibonding Se-*p* and Cu-*d* hybrid orbitals. The removal of Cu from the surface results in a lowering of the antibonding state and thus in a lowering of the VBM. For $CuInSe_2$, the VBM offset is calculated to be 0.22 eV, for $CuGaSe_2$ even 0.55 eV [182]. The lower VBM at the dislocation core with respect to the surrounding bulk Cu(In,Ga)Se_2 crystal acts as a barrier for holes, thus reducing recombination, which was confirmed for grain boundaries by two-dimensional device modelling [35, 187].

Indeed, electron-beam-induced current measurements (not shown here) conducted on a solar cell with a Cu(In,Ga)Se_2 layer containing dislocation densities of about 10^{10} to 10^{11} cm^{-2} [164] did not exhibit any substantial changes of the local short-circuit current. Also, two-dimensional device simulations of Cu(In,Ga)Se_2 solar cells with Cu(In,Ga)Se_2 layers containing such hole barriers at grain boundaries in the space-charge region [35, 38] indicate that power-conversion efficiencies of these solar cells are close to devices free of grain boundaries for VB offsets of larger than 0.2-0.3 eV. Taretto et al. [38] also raise the issue of tunnelling of charge carriers through the hole barriers to the grain boundaries, leading to tunnelling-enhanced recombination. These authors calculated the width of this barrier below which effective tunnelling-assisted recombination occurs to about 3 nm. This value is in good agreement with the full widths at half minima of the measured potential wells and of the Cu depletion detected by means of APT.

For Se-terminated {112} surfaces corresponding to case (b) in Fig. 5.17 with Se-containing dislocation core (i.e., Se-terminated {112} Cu(In,Ga)Se_2 surface in the DFT calculations), Persson and Zunger [182] report only a very small energy-band offset of about 40 meV for $CuInSe_2$ (for $CuGaSe_2$, there is even not any offset). However, the electronic band diagram at the dislocation core would not be similar to that of the grain interiors. Due to the increased density of point defects at this type of dislocation core,

it is expected that also the density of defect states within the band gap is larger, which should enhance recombination of charge carriers. To date, it remains unclear what the effect of the Se-containing dislocation core on the device performance of Cu(In,Ga)Se_2 solar cells is. The structural models for dislocation cores in Cu(In,Ga)Se_2 thin films in Fig. 5.17 would need also confirmation by means of ab-initio modelling.

Conclusions

Here, comprehensive insight was provided into the structural, compositional, and electrical properties of dislocations in Cu(In,Ga)Se_2 thin films. The 60° dislocations in Cu(In,Ga)Se_2 exhibit either a cation-containing or Se-containing core. Only at a part of the dislocations studied, the distributions of the average electrostatic potential, obtained by means of inline electron holography, show local minima with depths of about -1.4 V. Cu depletion within an about 3 nm wide region around dislocation cores, as indicated by APT, explains best the measured potential wells. The influences on these potential wells of the strain fields around the dislocations and of charge accumulations at the cores are rather small.
The structural model for dislocation core containing only cations comprises Na occupying partly Cu vacancies, leading to positive excess charge and field-induced Cu migration away from the dislocation. This Cu depletion is attended by the measured potential wells. The corresponding VB offsets at these type of dislocation may be one reason why still decent photovoltaic performance in spite of the presence of large dislocation densities in Cu(In,Ga)Se_2 thin-film solar cells. In contrast, for Se-containing dislocation cores, no Cu depletion and thus also no changes in the average electrostatic potential are predicted.

5.4 Planar defects: stacking faults and twin boundaries

5.4.1 Stacking faults

As stated in Section 5.3, the frequency of stacking faults bound to dissociated dislocations is rather low in Cu(In,Ga)Se_2 thin films. Also, these structural defects are not found frequently in corresponding transmission electron micrographs. This fact can be attributed to the rather high formation enthalpies (about 0.8-3 J/m^2 [163]), as compared with that in Si (about 50 mJ/m^2 [162]).

Yan et al. [137] reported that no deep-level defects generated by lamellar twins and stacking faults in Si, CdTe, and $CuInSe_2$, based on ab-initio density-functional theory calculations. Therefore, it is expected that, owing to the coherent nature of stacking faults, which does not involve the presence of dangling bonds, this planar lattice defect does not affect the electrical properties of the corresponding solar cells considerably.

5.4.2 Twin boundaries

The content of the present section is based on the following publications:
- D. Abou-Ras, B. Schaffer, M. Schaffer, S.S. Schmidt, R. Caballero, T. Unold, "Direct insight into grain boundary reconstruction in polycrystalline Cu(In,Ga)Se_2 with atomic resolution", Phys. Rev. Lett. 108 (2012) 075502-1-5, doi: 10.1103/PhysRevLett.108.075502.

- S.S. Schmidt, D. Abou-Ras, S. Sadewasser, W. Yin, C. Feng, Y. Yan, "Electrostatic potentials at Cu(In,Ga)Se_2 grain boundaries - experiment and simulations", Phys. Rev. Lett. 109 (2012) 095506-1-5, doi: 10.1103/PhysRevLett.109.095506.

Many analyses and simulations reported in the literature which refer to grain boundaries in Cu(In,Ga)Se_2 thin films actually only consider highly symmetric twin boundaries, which serve as model boundaries. All implications on structure-property relationships drawn at twin boundaries can, however, not be translated easily into those at general grain boundaries of low symmetry.

A good overview of possible twin constellations in Cu(In,Ga)Se_2 crystals is given by Krejci et al. [188]. It should be noted that the twin boundaries in this work (Krejci et al.) all exhibit a Σ value [52] of 3. Generally, the larger this quantity is, the lower is the symmetry of a grain boundary. Furthermore, a $\Sigma 3$ grain boundary is not necessarily a twin, and also grain boundaries with Σ values of higher than 3 may exhibit twin constellations.

It should be mentioned that the fraction of $\Sigma 3$ (twin) boundaries (with respect to the total density of grain boundaries) is generally high in Cu(In,Ga)Se_2 thin films, about 50-80% [189, 190] (see Fig. 5.18 for examples). Their frequencies were found to be dependent on the growth process of the thin film, particularly, on the stress imposed on the thin film during this process. For very fast Cu(In,Ga)$(S,Se)_2$ growth processes (e.g., rapid thermal processes) with holding durations at maximum temperature of few minutes, the relative frequencies of $\Sigma 3$ grain boundaries can reach values of up to about 80% [189]. This result gives rise to the assumption that the formation enthalpies of twin boundaries in Cu(In,Ga)Se_2 is rather low and that these planar defects are means of reducing strain in the thin films.

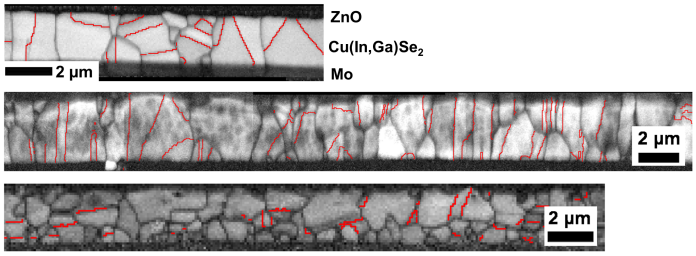

Figure 5.18: Pattern-quality maps from Cu(In,Ga)Se_2 thin films in various completed solar cells, with $\Sigma 3$ grain boundaries highlighted by red lines.

It is generally not possible by means of EBSD to determine the Σ values of grain boundaries in polycrystalline thin films for $\Sigma > 3$ unambiguously. This is owing to the fact that for a given Σ value (> 3), the misorientation between two neighboring grains in a polycrystalline thin film may deviate substantially from the expected orientation relationship corresponding to this misorientation.

Considering preferential orientations of twin boundaries with respect to the substrate, it was found [191] that they are not related to the integral textures in Cu(In,Ga)Se_2 thin films. For those grain boundaries which exhibit a twin configuration, it is possible to trace back how twinning occurred by evaluating the local orientations of adjacent grains. This is due to the fact that the rotation transformation of the twinning can be described by a unique rotation matrix (considering also corresponding symmetrically equivalent matrices). Starting from distinct crystal orientations such as

<100>/<001>, <110>/<201>, and <221>, it may be calculated using this matrix how these original orientations change after twinning. All grains which exhibit these resulting orientations can be highlighted in EBSD maps, and should be adjacent to grains with the original orientations for Σ3 grain boundaries. More detailed reports on this approach can be found in Refs. [192, 193].

Σ3 twin boundaries

Persson and Zunger [181, 182] proposed a lowering of the valence-band maximum (VBM) at grain boundaries (with twin constellations), acting as barrier for holes in the grain interiors, thus reducing recombination through defects at the GB. In their calculations by first principles density functional theory (DFT), these authors modeled twin boundaries in $CuInSe_2$ and $CuGaSe_2$ as being formed by two polar {112} surfaces, which are considered more stable than non-polar surfaces in $CuInSe_2$ and $CuGaSe_2$ because of the low formation energies for surface reconstruction. This reconstruction involves generation of either Cu vacancies at cation-cation terminated surfaces or In_{Cu} antisites at the subsurfaces of the Se-{112} planes (Se-Se termination). In case of a surface reconstructed by Cu vacancies, a lowering of the VBM is found. The VBM of $CuInSe_2$ consists of antibonding Se-p and Cu-d hybdrid orbitals. The removal of Cu from the surface results in a lowering of the antibonding state and thus in a lowering of the VBM. In contrast, the VBM is not changed substantially at Se-Se-terminated GBs [182].

Σ3 twin boundaries in Cu(In,Ga)Se_2 thin films in ZnO/CdS/ Cu(In,Ga)Se_2/Mo/glass solar-cell stacks were identified [194] in high-resolution scanning transmission electron microscopy (HR-STEM) images. By means of spatially resolved electron energy-loss spectrometry (EELS) measurements, the elemental occupations of the individual atomic columns were determined. The authors of Ref. [194] show that the twin boundaries can be divided into three categories: two with Se-Se terminated {112} lattice planes (type I and II), and one with a cation-containing {112} plane facing a Se {112} plane (type III), see Fig. 5.19 for an overview. Cation-cation terminated twin boundaries were not identified in the sample studied. It is apparent from the HR-STEM images in Fig. 5.19 that the distances between the atomic planes adjacent to the twin-boundary planes are larger for the type I and II twins (0.28±0.01 and 0.29±0.01 nm, while 0.20±0.01 nm at the type III twin boundary; the errors were estimated as systematic from various measurements). This difference in distance can be attributed to different Se-Se and Se-cation bonding lengths across the type I/II and III twin boundaries.

Elemental distribution maps composed of Cu, In, and Se signals extracted from individual EEL spectra acquired on an area containing a twin boundary of type I (Fig. 5.19) are given in Fig. 5.20. It was not possible to evaluate the Ga-$L_{2,3}$ edge since it was superimposed by the Cu-$L_{2,3}$ edge in the EEL spectrum. Na and oxygen signals do not exhibit intensities above the noise level. Also APT measurements have so far not given rise to accumulations of impurities at twin boundaries in Cu(In,Ga)Se_2 thin films [195].

While the Se signal distribution (Fig. 5.20b) corresponds well to the atomic lattice image given in Fig. 5.20a, the In and Cu distributions appear smeared out, suggesting interdiffusion of these atoms. Nevertheless, substantial Cu depletion and slight In enrichment is found at the position of the twin boundary (Figs. 5.20c and d), compared with the grain interiors, as illustrated by the linescan given in Fig. 5.20e.

Corresponding HR-STEM and EELS measurements at the type II twin boundary

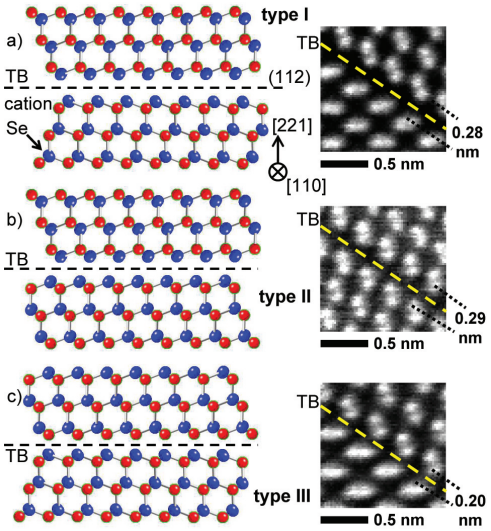

Figure 5.19: Structural representations of the twin boundaries (TBs) analyzed for the present work and the corresponding high-resolution STEM images (type I, II, and III). The positions of the Se and cation columns were determined from EELS measurements (by Figs. 5.20, 5.21, and 5.22.

(5.21) confirmed the results from the type I twin boundary. In contrast, no considerable In enrichment (as compared with the Se signal) but indeed also Cu depletion was detected at the type III twin boundary (Fig. 5.22). As found for the type I and II twin boundaries, Na and oxygen signals exceeding the noise level were not measured.

This result of Cu depletion and In enrichment at type I and II twin boundaries is a direct, experimental evidence for the model given by Persson and Zunger [181, 182], which assumes reconstruction of such twin boundaries by the formation of Cu vacancies and In_{Cu} antisite defects. Since {112} planes contain both, Cu and In (and Ga) atoms, the finding of reduced Cu and enhanced In signals can not be explained by geometrical aspects at the twin boundary but only by atomic reconstruction. As suggested by the reduced Cu signal at the type III twin boundary, reconstruction of internal surfaces via formation of Cu vacancies takes also place in case of oppositely charged polar surfaces (type III twin boundary).

It should be noted that the region of compositional changes at the twin boundaries is very narrow, only of approximately 0.7-0.8 nm in width, corresponding well to about twice the interplanar distances of {112} planes in Cu(In,Ga)Se_2 crystals (about 0.33 nm; for type I and II twin boundaries, taking into account also the gap between the Se-containing {112} planes, about 0.08-0.09 nm, see Fig. 5.19). In previous studies, Siebentritt et al. [196] as well as Hafemeister et al. [197] reported about the transport properties and local surface potentials across a $\Sigma 3$ twin boundary in $CuGaSe_2$. These authors found this twin boundary to be charge neutral. Furthermore, they were able to simulate conductivity and Hall measurements by taking into account tunneling of holes across a 2 nm wide and 170 meV deep barrier at the twin boundary, formed by a lowered VBM. The width of this suggested barrier is larger than the extensions of the regions at twin boundaries with compositional changes, as given in Figs. 5.20, 5.21, and 5.22. Nevertheless, tunneling of charge carriers to the twin boundary is very

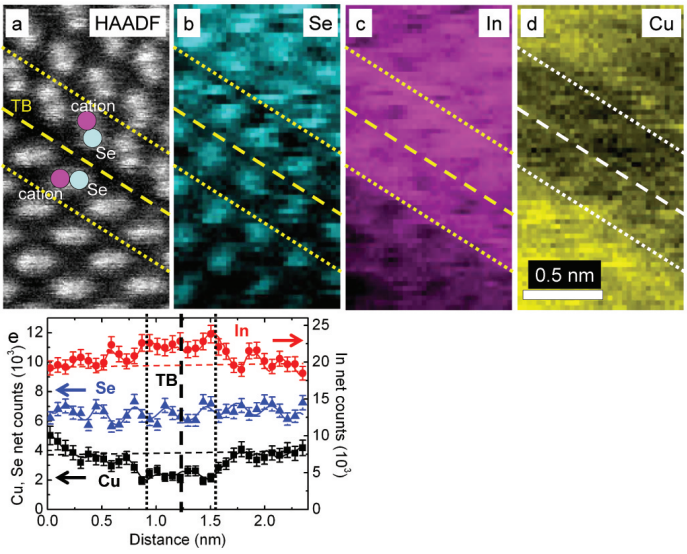

Figure 5.20: High-resolution STEM image (a) of the Se-Se-terminated twin boundary (TB) given in Fig. 5.19a, as well as Se, In, and Cu distribution maps (b, c, and d) extracted from EELS spectra acquired on the identical area as the STEM image. An EELS line scan acquired across this TB at yet a different position (e) exhibits substantial Cu depletion and slight In enrichment at the position of the TB. Dotted lines in a-e indicate the limits of the region around the TB where changes in composition were detected. Dashed horizontal lines in (e) give the level of the Se signal, which was taken as reference. The error bars were estimated from the systematic errors at 10% of the measured values.

probable for widths below 3 nm, as calculated by Taretto et al. [38].

Analyses of Σ3 twin boundaries by means of electron-beam-induced current (EBIC) [138, 198, 199], cathodoluminescence (CL) [77, 132], scanning Kelvin probe force microscopy (KPFM) [139], as well as scanning capacitance microscopy (SCM) [140], all combined with EBSD on the identical sample positions, showed no sign of considerably reduced short-circuit currents, radiative recombination, charge accumulations, or local doping level at most twins boundaries. These highly symmetric, planar defects exhibit small depths of electrostatic potential wells (obtained by electron holography) of not more than 200 mV, with widths of about 1-2 nm [191]. Although such extensions give rise to tunneling-enhanced recombination, (most) twin boundaries are considered not to affect substantially the device performance of the Cu(In,Ga)Se_2 thin-film solar cell. This result is not very astonishing since similar results have already been obtained on twins in Ge [46] and Si [47] more than 50 years ago.

The overall low electrical activity at Σ3 twin boundaries may be related to the small densities of dangling bonds at twin boundaries and the correspondingly similar density of states as within the grains. Also, Yan et al. [137], who performed ab-initio calculations for Σ3 twin boundaries with {114} twin boundary planes (exhibiting a dislocation core) compared density of states before and after lattice relaxation and show that after lattice relaxation, the density of deep defect levels in the band gap at these twin boundaries is very low.

It should be mentioned that for a small fraction of Σ3 twin boundaries, indeed,

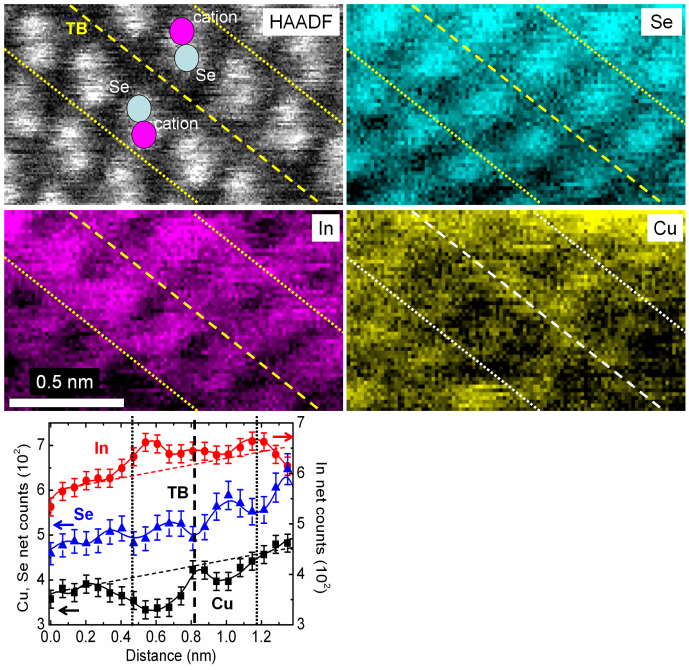

Figure 5.21: High-resolution STEM image of the Se-Se-terminated twin boundary (TB) given in Fig. 5.19b, as well as Se, In, and Cu distribution maps extracted from EELS spectra acquired on the identical area as the STEM image. An EELS line scan acquired across this TB at yet a different position exhibits substantial Cu depletion and slight In enrichment at the position of the TB. Dotted lines in a-e indicate the limits of the region around the TB where changes in composition were detected. Dashed horizontal lines in (e) give the level of the Se signal, which was taken as reference. The error bars were estimated from the systematic errors at 10% of the measured values.

changes in EBIC [77], CL [132], KPFM [139], and SCM measurement signals [140] were detected. For these rare cases, the twin constellation may be assumed incoherent (twin-boundary plane not identical with {112} symmetry plane).

Σ9 twin boundaries

Scientific reports about twin boundaries in Cu(In,Ga)Se_2 thin films with Σ values of larger than 3 are very rare. Hafemeister et al. [197] performed electrical transport studies combined with local charge measurements on a Σ9 twin boundary in a $CuGaSe_2$ bicrystal (see Fig. 5.23), which exhibits a lower symmetry compared with highly symmetric Σ3 twin boundaries treated in various recent reports [181,182,196,200,201].The results indicate the presence of a thin (few nm) and high (up to about 500 meV) transport barrier for majority carriers at the Σ9 twin boundary, which is considerably larger than the value given for a Σ3 twin boundary (170 meV [197], see above). Concerning possible effects of Σ9 twin boundaries on the device performance, it can be assumed that a barrier of 500 meV would reduce the hole transport substantially, which has an impact on the overall device performance.

Schmidt et al. [169] report on a combined ab-initio DFT calculation, multislice

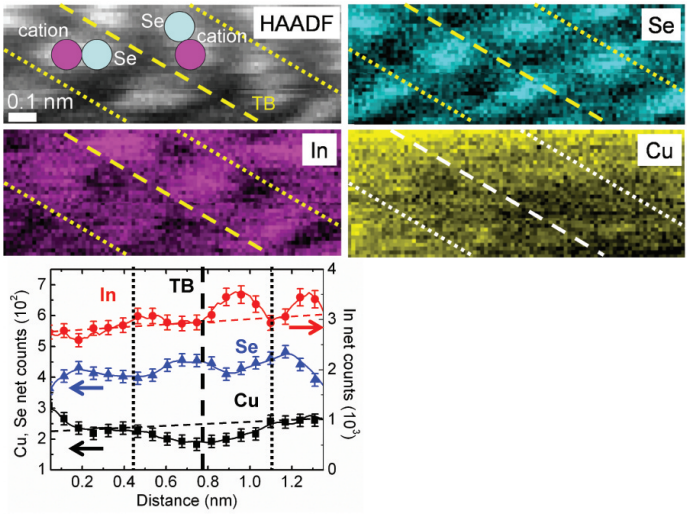

Figure 5.22: High-resolution STEM (HAADF) image of the Se-cation-terminated twin boundary (TB) given in Fig. 5.19c, as well as In, Se, and Cu distribution maps extracted from EELS spectra acquired on the identical area as the STEM image. The elemental distribution profiles were extracted from across the maps. Dotted lines in the STEM image, the maps, and the profiles indicate the limits of the region around the TB where changes in composition were detected. Dashed horizontal lines give the level of the Se signal, which was taken as reference. The error bars were estimated from the systematic errors at 10% of the measured values.

simulation, and electron holography study, conducted on the same $CuGaSe_2$ bicrystal sample with Σ9 twin boundary as studied by Hafemeister et al. [197]. The electrostatic potential obtained by means of electron holography is about 0.8 V lower at the Σ9 twin boundary core than in the grain interiors (Fig. 5.24). This value is larger than depths of potential well measured at Σ3 twin boundaries (about 0.2 V) [191]. The full width at half minimum of this potential well is about 1.5 nm (similar to the values found at Σ3 twin boundaries). By DFT calculations and multislice simulations, Schmidt et al. found that one major contribution to the potential well measured is the reduced density of atoms at the cation and anion GB cores, rather than the differences in charge density of individual atoms. Unfortunately, changes of composition have not yet been confirmed at Σ9 twin boundaries, although they would be quite probable,

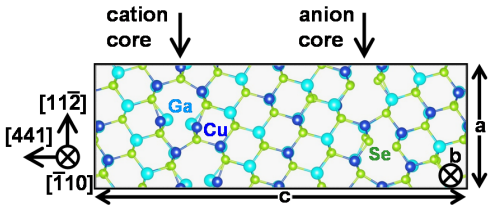

Figure 5.23: Crystal model of the $CuGaSe_2$ Σ9 twin boundary cores after ab-initio DFT calculations.

regarding corresponding results obtained at Σ3 twin boundaries and also random grain boundaries (see below).

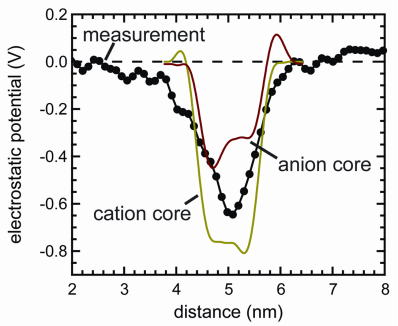

Figure 5.24: The measured potential profile, as well as multislice-simulated, electrostatic potential profiles across the anion and cation grain-boundary cores.

5.5 Grain boundaries

The content of the present section is based on the following publications:
- R. Baier, C. Leendertz, D. Abou-Ras, M.C. Lux-Steiner, S. Sadewasser, Properties of electronic potential barriers at grain boundaries in Cu(In,Ga)Se2 thin films, to be published in Sol. En. Mater. Sol. Cells (2014).
- M. Müller, D. Abou-Ras, T. Rissom, F. Bertram, J. Christen, "Symmetry dependent optoelectronic properties of grain boundaries in polycrystalline Cu(In,Ga)Se_2 thin films", J. Appl. Phys. 115 (2014) 023514-1-6, doi: 10.1063/1.4861149.
- J. Kavalakkatt, D. Abou-Ras, J. Haarstrich, C. Ronning, M. Nichterwitz, R. Caballero, T. Rissom, T. Unold, R. Scheer, H.W. Schock, "Electron-beam-induced current at absorber back surfaces of Cu(In,Ga)Se_2 thin-film solar cells", J. Appl. Phys. 115 (2014) 014504-1-10, doi: 10.1063/1.4858393.
- D. Abou-Ras, S.S. Schmidt, R. Caballero, T. Unold, H.-W. Schock, C.T. Koch, B. Schaffer, M. Schaffer, P. Choi, O. Cojocaru-MirÃ©din, "Confined and chemically flexible grain boundaries in polycrystalline compound semiconductors", Adv. En. Mater. 2 (2012) 992-998, doi: 10.1002/aenm.201100764.
- D. Abou-Ras, B. Schaffer, M. Schaffer, S.S. Schmidt, R. Caballero, T. Unold, "Direct insight into grain boundary reconstruction in polycrystalline Cu(In,Ga)Se_2 with atomic resolution", Phys. Rev. Lett. 108 (2012) 075502-1-5, doi: 10.1103/PhysRevLett.108.075502.
- O. Cojocaru-Mirédin, P.-P. Choi, D. Abou-Ras, S.S. Schmidt, R. Caballero, D. Raabe, "Characterization of Grain Boundaries in Cu(In,Ga)Se_2 films using Atom Probe Tomography", J. Photovolt. 1 (2011) 207-212, doi: 10.1109/JPHOTOV.2011.2170447.
- R. Baier, D. Abou-Ras, T. Rissom, M.C. Lux-Steiner, S. Sadewasser, "Symmetry-dependence of electronic grain boundary properties in polycrystalline $CuInSe_2$ thin films", Appl. Phys. Lett. 99 (2011) 172102-1-3, doi: 10.1063/1.3652915.
- S. Sadewasser, D. Abou-Ras, D. Azulay, R. Baier, I. Balberg, D. Cahen, S. Cohen, K. Gartsman, G. Karuppiah, J. Kavalakkatt, W. Li, O. Millo, Th. Rissom, Y. Rosenwaks, H.-W. Schock, A. Schwarzman, T. Unold, "Nanometer-scale electronic and microstructural properties of grain boundaries in Cu(In,Ga)Se_2", Thin Solid Films 519

(2011) 7341-7346, doi:10.1016/j.tsf.2010.12.227.
- M. Nichterwitz, D. Abou-Ras, K. Sakurai, J. Bundesmann, T. Unold, R. Scheer, H.W. Schock, "Influence of grain boundaries on current collection in Cu(In,Ga)Se_2 thin-film solar cells", Thin Solid Films 517, pp. 2554-2557 (2009), doi: 10.1016/j.tsf.2008.11.064.
- D. Abou-Ras, S. Schorr, H.-W. Schock, "Grain sizes and grain boundaries in chalcopyrite-type thin films", J. Appl. Cryst. 40 (2007) 841-848, doi:10.1107/S0021889807032220.

After having treated highly symmetrical twin boundaries, the present section deals with randomly oriented grain boundaries (GBs) of low symmetry. Note that in general, a GB does not resemble a straight plane but exhibits a certain curvature, in contrast to twin boundaries. As a consequence, there are not any specific crystal planes found at GBs for the neighboring grains, again in contrast to the atomic constellations of (coherent) twins. Therefore, it can be expected that the density of dangling bonds is high, which may result in an excess charge density, and also that the mass density is reduced only because of the spacings in between the atomic lattices of the neighboring grains.
As stated above (section 5.4.2), the relative frequency of $\Sigma 3$ (twin) boundaries in polycrystalline thin films is rather high (50-80%). This is, fewer than 50% of all GBs are random ones of low symmetry (for Cu(In,Ga)Se_2 thin films in solar cells with power-conversion efficiencies of more than 15%). Since $\Sigma 3$ (twin) boundaries do not affect the solar-cell performance substantially (section 5.4.2), influences on the photovoltaic device are expected mainly from the low-symmetrical (random) GBs, and to a small extent also from twin boundaries with Σ values of larger than 3.

In the following, an overview will be given on the various analyses which have been performed on GBs in polycrystalline thin films, and on the few efforts of combining the corresponding techniques with EBSD measurements on identical specimen positions, in order not only to determine positions of GBs unambiguously but also to distinguish between $\Sigma 3$ (twin) and random GBs. Only in case this information from EBSD maps is available, conclusions on electrical or optoelectronic properties of GBs can be drawn (else, one can not be sure whether a specific signal was really measured at the position of a GB).

In the following, correlative EBSD analyses on random GBs combined with other techniques applied in scanning electron (SEM) and scanning probe microscopy (SPM) are presented. Moreover, details are given also on the characterization of random GBs by means of atom-probe tomography (APT) as well as by high-resolution scanning transmission electron microscopy (HRSTEM), electron energy-loss spectrometry (EELS), and inline electron holography. An important issue are the different information depths of the techniques applied, as already outline in Chapter 4.5. This is to be considered when comparing the corresponding results and concluding on a consistent picture of GBs in Cu(In,Ga)Se_2 thin films.

5.5.1 Cathodoluminescence analyses at grain boundaries

All cathodoluminescence measurements on Cu(In,Ga)Se_2 GBs that are reported in the literature [131,202–206] were conducted at low temperatures of nominally 5-100 K. This is because the signal-to-noise ratio at ambient temperatures is very small. However, the optoelectronic properties of Cu(In,Ga)Se_2 GBs at low temperatures may not be the same as the ones for ambient temperatures (at which the solar cell is operated).

A further correlative EBSD/CL work was performed by Müller et al. [132]. Fig. 5.25 shows the EBSD pattern-quality images [207] of $CuInSe_2$, $CuGaSe_2$, and Cu(In,Ga)Se_2

thin films in complete solar cell stacks (Mo/glass substrates and ZnO/CdS window layers), together with spatial distributions of the CL intensity and the CL peak wavelength. The $CuInSe_2$ layer displays by far the largest grains compared to the other two samples. A detailed analysis of the spatial distribution of the grains and average grain sizes of the $CuInSe_2$, $CuGaSe_2$, and Cu(In,Ga)Se_2 thin films studied in the present work is discussed by Dietrich et al. [164].

In Fig. 5.25, Σ3 (introduced in section 3.4.1) GBs are highlighted by solid lines and non-Σ3 GBs by dashed lines in the EBSD pattern-quality maps. This information was transferred to CL intensity and CL peak wavelength maps acquired at identical positions. The CL images are compiled of three individual maps, with the intensity images showing the spectrally integrated intensity at a specific point, and the peak wavelength images displaying the corresponding wavelength of the local maximum in the CL spectrum.

Fig. 5.26 shows CL spectral linescans extracted across representative Σ3 and non-Σ3 GBs on the $CuGaSe_2$ sample. The corresponding positions are marked in Fig 1b by arrows. The spectral position of the luminescence is not influenced by the Σ3 GB (Fig. 5.26a), whereas at the non-Σ3 GB (Fig. 5.26b), a spectral shift of 4.2 meV to lower energies was detected.

The CL spectral images from a large number of GBs in $CuInSe_2$ and $CuGaSe_2$ thin films were evaluated, and their spectral shifts are summarized in Fig. 5.27. All analyzed Σ3 GBs in $CuInSe_2$ (Fig. 5.27a) and $CuGaSe_2$ (Fig. 5.27b) do not exhibit a spectral shift. In contrast, 10 out of 13 non-Σ3 GBs in $CuInSe_2$ layers and 11 out of 14 non-Σ3 GBs in $CuGaSe_2$ layers show a red shift of up to 9 meV, which agrees well with values published by Romero et al. [131, 206].

This result indicates that the generation of charge carriers and also the radiative recombination behavior does not change substantially across high-symmetry Σ3 GBs. Even though a spectral shift at non-Σ3 GBs was detected, the corresponding values are much smaller than the thermal energy $k_B T$. Thus, this effect may not have a considerable impact on the device performance of the solar cell operated at ambient temperature.

In addition, it should be noted that although the position of the impinging electron beam during the CL spectral imaging is known, it is unclear where the luminescence signal is emitted from in the sample. Diffusion of charge carriers generated by the electron has to be considered, as well as preferential CL emission depending on the band-gap energy in the specimen. For example, one possible scenario may be that the band-energy at GBs is larger, and that all charge carriers generated at the GBs first would diffuse to the grain interiors before recombining. However, within the scope of the present work, we were not able to verify a corresponding energy-band diagram at and around GBs.

In contrast to the $CuInSe_2$ and $CuGaSe_2$ layers, the results from CL spectral images obtained on the Cu(In,Ga)Se_2 thin film (containing In and Ga) are by far more difficult to interpret. This is mainly because of the fact that this layer does not exhibit homogeneous elemental distributions but In/Ga gradients perpendicular to the substrate. As a consequence, the assignment of the positions of the GBs to the CL signals was not as precise as for the $CuInSe_2$ and $CuGaSe_2$ layers, which is particularly severe because of the rather small average grain sizes in the Cu(In,Ga)Se_2 layer (about 0.5 μm, which substantially smaller than those if the $CuInSe_2$ and $CuGaSe_2$ thin films). The signals from neighboring GBs superimpose each other considerably. Therefore, we decided not to discuss the spectral shifts and intensity distributions across GBs in the Cu(In,Ga)Se_2 thin film studied in the present work. This issue will be subject to

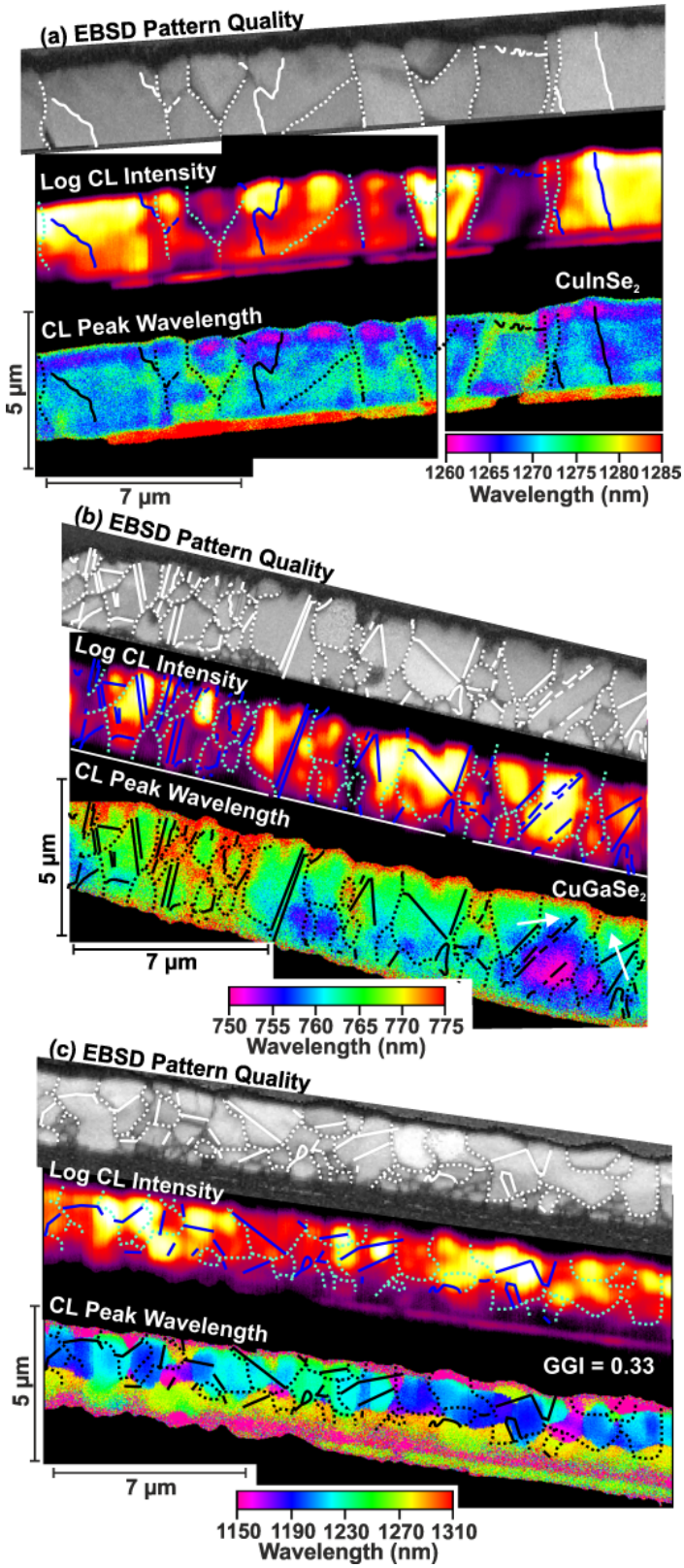

Figure 5.25: EBSD pattern-quality maps, CL intensity images and CL peak wavelength images of polished (a) $CuInSe_2$, (b) $CuGaSe_2$, and (c) $Cu(In,Ga)Se_2$ cross sections. The positions GBs, determined by the EBSD maps, are highlighted by solid lines for $\Sigma 3$ GBs and by dashed lines for non-$\Sigma 3$ GBs.

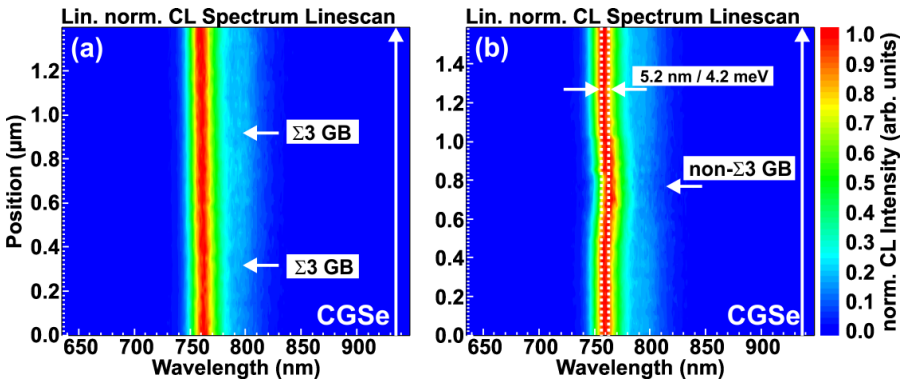

Figure 5.26: Exemplary spectral linescans across Σ3 GBs (a) and a non-Σ3 GB (b) acquired on a cross-section sample of a $CuGaSe_2$ solar cell.

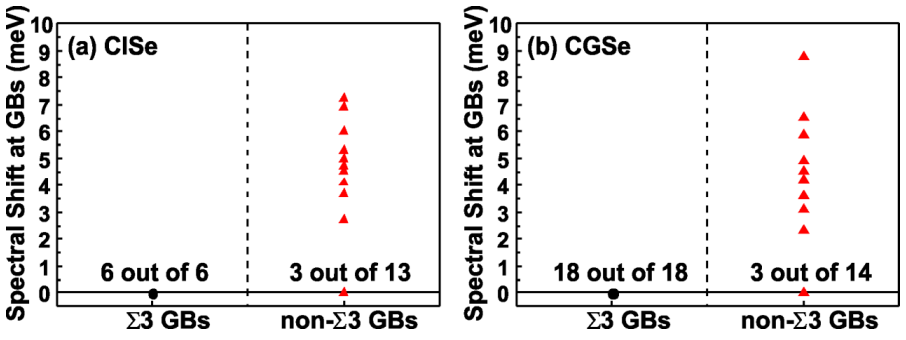

Figure 5.27: Spectral red shift of the luminescence at the GB separately for Σ3 GBs and non- Σ3 GBs for $CuInSe_2$ (a) and $CuGaSe_2$ (b). The black numbers display the count of GBs with no spectral shift.

future studies.

Another question is the behavior of the intensity at the GBs and its symmetry dependence. A reduction of the luminescence intensity at GBs has been reported in former CL studies [131,202,205,206]. Fig. 5.28 shows examples of spectrally integrated intensity profiles extracted from linescans across different GBs on the $CuInSe_2$ sample, which are representative also for the $CuGaSe_2$ and $Cu(In,Ga)Se_2$ thin films. As already visible in Fig. 5.25, there are Σ3 and non-Σ3 GBs which demonstrate a dip of the intensity (Figs. 5.28a and b). On the other hand, there are GBs which exhibit a step (Fig. 5.28c), representing the intensity difference between neighboring grains, and (Σ3) GBs with no substantial change in intensity (Fig. 5.28d).

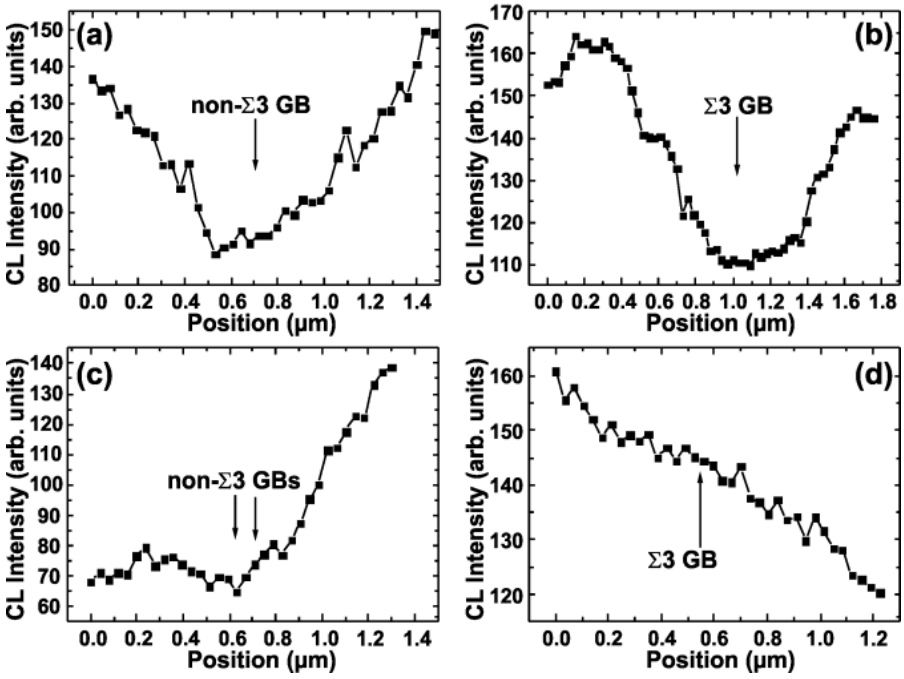

Figure 5.28: CL intensity profiles, extracted from linescans perpendicular to different Σ3 and non- Σ3 GBs on the $CuInSe_2$ sample.

Fig. 5.29 gives a summary of the intensity changes at GBs in the ternary layers. Here, again a symmetry dependence is clearly visible. Most of the Σ3 GBs in $CuInSe_2$ (Fig. 5.29a) and in $CuGaSe_2$ thin films (Fig. 5.29b) do not reveal a substantial change above the noise level in the CL intensity profiles across the GB. In contrast, most of the non-Σ3 GBs in $CuInSe_2$ and $CuGaSe_2$ layers exhibit steps or local minima in the CL signals. For the $CuInSe_2$ layer, the decreases of intensity were found to be down to about 55%, while at $CuGaSe_2$ GBs, these values were even down to 90%. We will see further below that these strongly varying CL signals at different GBs can be explained in terms of different changes in composition and the correspondingly different electronic band diagrams, leading to different radiative recombination behaviors.

Apart from the symmetry issue, it is apparent from the present work that CL signals change differently at different (non-Σ3) GBs. In addition, the CL intensities vary also between adjacent (Figs. 5.28c and 5.29) and inside individual grains substantially. Within 10 individual grains, the distributions CL intensity profiles were investigated.

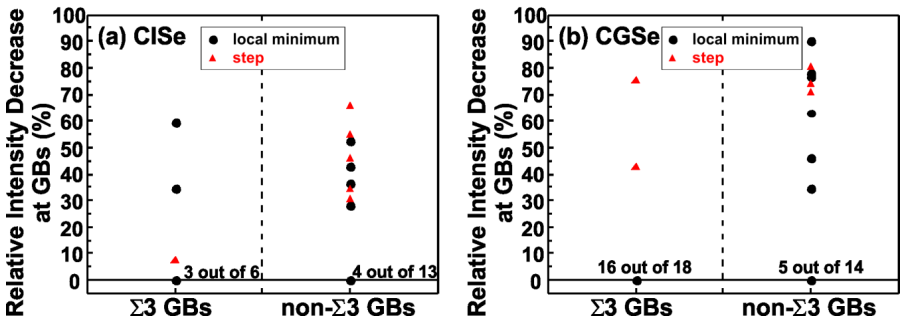

Figure 5.29: Relative intensity reduction at GBs separately for Σ3 GBs and non- Σ3 GBs for $CuInSe_2$ (a) and $CuGaSe_2$ thin films (b). The decreased intensity is divided into step-like features (steps) and local minima (dips). See Fig. 5.28 for examples.

The resulting maximum relative variations in CL intensity are summarized in Fig. 5.30. We find that the $CuInSe_2$ ($CuGaSe_2$) thin film exhibits variations in the range of 26 to 85% (8 to 50%). The Cu(In,Ga)Se_2 sample comprises either grains showing small fluctuations of around 10% or those with high variations of around 90%.

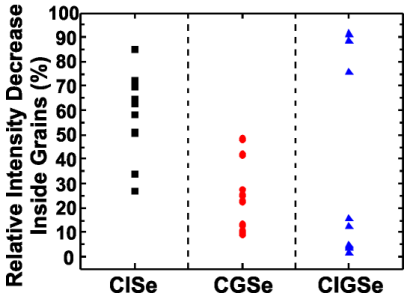

Figure 5.30: Relative intensity decreases (variations, normalized to the maximum CL intensity) extracted from intensity profiles acquired inside of 10 different grains within the $CuInSe_2$, $CuGaSe_2$, and Cu(In,Ga)Se_2 thin films.

In an effort to extract effective diffusion lengths for minority charge carriers and also recombination velocities at GBs, we have applied the approach suggested by Mendis et al. [208] for GBs in CdTe thin films. However both, the resulting diffusion lengths and the recombination velocities of about 100-300 nm and 1-10 cm/s, were smaller than values reported in the literature, which are typically in order of about 0.5-1.6 μm [198,209] and 10^3-10^4 cm/s [198,210]. A limiting issueis that constant CL signals over several micrometers within grains adjacent to a given GB are required for successful application of this approach, which is not provided for the Cu(In,Ga)Se_2 thin films studied in the present work. Thus, the approach suggested by Mendis et al. [208] is not applicable here.

5.5.2 Electron-beam-induced current analyses at grain boundaries

For these measurements, the electron-beam induced (short-circuit) current (EBIC) is detected as a function of the position of irradiation a [55]. A current line-profile perpendicular to the p-n junction $I(a)$ can be described by a convolution of the generation profile $g(x, a)$ and the collection function $\phi(x)$ [211]:

$$I_{\mathrm{EBIC}}(a) = \int g(x, a)\phi(x)\mathrm{d}x \tag{5.7}$$

where x is the spatial coordinate perpendicular to the p-n junction and a is the x coordinate of the position of irradiation. For this one dimensional expression, translation invariance parallel to the p-n junction is assumed, which means that, e.g., effects of GBs on charge carrier collection are not considered. Furthermore, low injection conditions are assumed (i.e., the charge-carrier density generated by the impinging electron beam is smaller than the net doping), and the collection function must not depend on the position of generation. The collection function of a solar cell with single p-n junction is maximum in the space charge region because of field assisted charge carrier collection and decreases in direction of the back contact in the quasi neutral region. The decrease is determined by the absorber layer minority charge-carrier diffusion length [209].
In a previous EBIC study, however, it was shown that in Cu(In,Ga)Se_2 solar cells, charge carrier collection is generation dependent [212]. Therefore, EBIC profiles cannot be described by Eq. 5.7 assuming a constant collection function. This behaviour was explained by assuming that the width of the space charge region depends on the position of generation due to charge carrier trapping in deep acceptor-type defect states close to the Cu(In,Ga)Se_2/CdS interface (p^+ layer). The space charge region is larger for generation close to the Cu(In,Ga)Se_2/CdS interface and smaller for generation in the Cu(In,Ga)Se_2 bulk [209, 213]. It was also shown that "intensive" electron beam irradiation of the interface region of the cross section of a Cu(In,Ga)Se_2 solar cell changes the shape of EBIC profiles: the maximum gets broader and it shifts to higher current values [55], which might be caused by a reduction of the space charge density due to the irradiation [55].
In the high injection regime, i.e., if the density of generated charge carriers is in the same range or larger than the equilibrium charge carrier density, charge-carrier collection is qualitatively different. This difference can have a significant impact on the shape of EBIC profiles.
Empirical descriptions of $g(x, a)$ can be found in Refs. [214, 215]. A solution for the collection function $\phi(x)$ obtained from the charge-carrier continuity equation for the neutral region of a semiconductor with a back contact under low injection conditions is:

$$\phi(x) = \frac{1/L\cosh\left((x - x_{\mathrm{Mo}})/L\right) - S_{\mathrm{Mo}}/D\sinh\left((x - x_{\mathrm{Mo}})/L\right)}{S_{\mathrm{Mo}}/D\cosh\left((x - x_{\mathrm{SCR}})/L\right) - 1/L\sinh\left((x_{\mathrm{Mo}} - x_{\mathrm{SCR}})/L\right)} \tag{5.8}$$

where L is the diffusion length of the electrons generated in the Cu(In,Ga)Se_2 layer, S_{Mo} is the recombination velocity at the Mo back contact, D is the electron diffusion constant, x_{Mo} is the position of the back contact and x_{SCR} is the position of the edge of the space-charge region (SCR).
If charge carriers are generated in the proximity of a surface or interface where enhanced recombination takes place, they can be attributed a reduced effective lifetime.

The modified collection function in case of the presence of such a surface can be desribed by replacing L in Eq.5.8 by a reduced effective diffusion length L_{eff} [4]

$$L_{\mathrm{eff}} = \sqrt{1 - [S_{\mathrm{SF}} L / S_{\mathrm{SF}}(L+1)] \int g(z) \exp(-z/L) dz} \tag{5.9}$$

where z is the coordinate perpendicular to the surface, S_{SF} is the charge-carrier recombination velocity at the surface and $g(z)$ is the generation profile. By deconvolution of the measured EBIC line profiles $I(a)$ and extraction of L_{eff} in dependence of E_{B} by fitting, the charge-carrier diffusion length L, the recombination velocity at the back contact S_{Mo} and the recombination velocity at the Cu(In,Ga)Se_2/vacuum-interface S_{SF} can be determined.
In a similar manner, GBs can be considered surfaces with recombination velocities S_{GB}, neglecting substantial accumulation of charges and also changes in composition, both affecting the energy-band diagram at the surface. An effective diffusion length $L_{\mathrm{eff}}^{\mathrm{GB}}$ can be determined depending on the distance y to the GB, instead of on the coordinate z, in analogy to Eq. 5.9:

$$L_{\mathrm{eff}}^{\mathrm{GB}}(y) = \sqrt{1 - [S_{\mathrm{GB}} L_{\mathrm{eff}} / S_{\mathrm{GB}}(L_{\mathrm{eff}}+1)] \int g(y) \exp(-y/L_{\mathrm{eff}}) dy} \tag{5.10}$$

Due to the lateral generation function $g(y)$, the diffusion length $L_{\mathrm{eff}}^{\mathrm{GB}}$ depends on the acceleration energy E_{B}. In the case of GBs, the collection function $\phi(y,z)$ depends also on the distance y to the GB.

Correlative EBIC/EBSD results from cross-sections of Cu(In,Ga)Se_2 solar-cell stacks

Fig. 5.31 shows a SEM image, an EBSD pattern-quality map and EBIC maps at different beam-energies E_{B} of a polished cross section of a Cu(In,Ga)Se_2 solar-cell at the same position. The brighter a pixel of an EBIC map is displayed the larger is the corresponding current. The EBIC maps were recorded after intensive irradiation of the ZnO layer close to the *p*-*n* junction. This is necessary in order to avoid the formation of a barrier impeding the electron flow at the Cu(In,Ga)Se_2/CdS interface as explained in Ref. [78] in terms of a persistent reduction of the negative charge density in a p^+ layer at the Cu(In,Ga)Se_2/CdS interface.

In Fig. 5.32, EBIC profiles across the GB indicated in Fig. 5.31 are shown together with simulated EBIC profiles parallel to the *p*-*n* junction for different recombination velocities S_{GB}. The position of the minimum was set to y=0. The model is based on the assumption of a reduced effective diffusion length L_{eff} in the proximity of a GB due to recombination at the Cu(In,Ga)Se_2/vacuum interface and at the GB as described by Eq. 5.10. It can only give a rough estimate for S_{GB} since for the description of the lateral generation profile, one-dimensional, empiric expressions [214,215] are used, which only describe charge-carrier generation at the position of irradiation correctly. For the simulation the following values were used: $D = 1$ cm^2/s, $L = 0.8$ μm, $S_{\mathrm{SF}} = 8{\times}10^4$ cm/s and $S_{\mathrm{SF}} = 8{\times}10^4$ cm/s. A comparison indicates that the EBIC contrast given in Fig. 5.31 may be caused by GB recombination with a velocity of about $S_{\mathrm{GB}} \approx 10^3 - 10^4$ cm/s.

It should be noted that by far not all EBIC profiles across random GBs in polycrystalline Cu(In,Ga)Se_2 thin films (acquired on cross-sections of high-efficiency solar

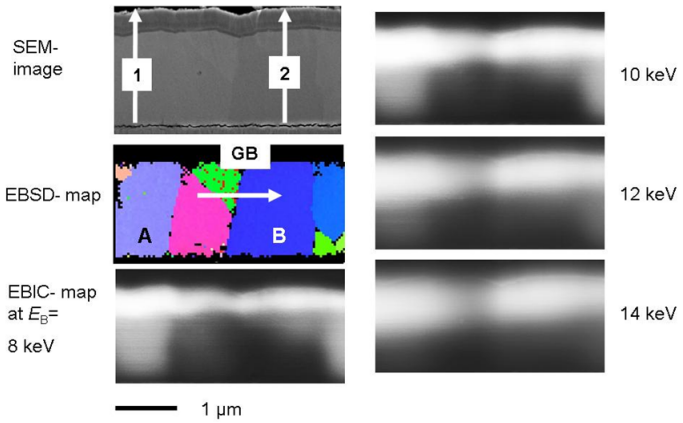

Figure 5.31: Cross-sectional SE image, EBSD map and EBIC images at different beam energies E_B at the same identical sample position of a Cu(In,Ga)Se_2 solar-cell. From Ref. [198].

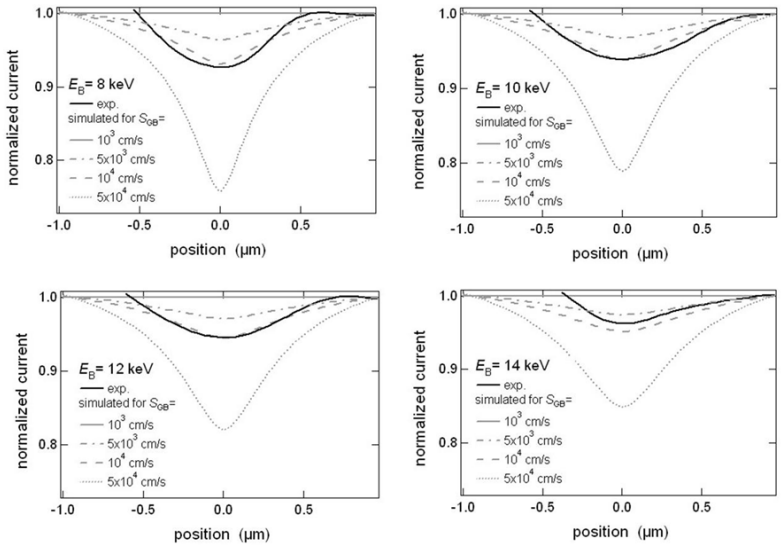

Figure 5.32: Measured EBIC line profiles parallel to the p-n junction extracted from the EBIC images in Fig. 5.31, as well as simulated curves for different GB recombination velocities S_{GB}. The GB is located at y=0. From Ref. [198].

cells) exhibit a local minimum at the position of the GB. Kawamura et al. [199] as well as Nichterwitz [216] found EBIC signals also to be enhanced at some (random) GBs. These results will be corroborated by combined EBSD/EBIC measurements at back surfaces of Cu(In,Ga)Se_2/CdS/ZnO stacks in the following section.

Different EBIC profiles across various GBs from the backsides of Cu(In,Ga)Se_2/CdS/ZnO stacks

The acquisition of correlative EBSD and EBIC data from backsurfaces of Cu(In,Ga)Se_2/CdS/ZnO stacks provides the advantage of analyzing large specimen areas with a high number of grains and GBs. However, owing to the different measurement geometry, the model by Donolato [4] used for the cross-section EBIC profiles can not be applied. Instead, EBIC images need to be acquired at various electron-beam energies E_B. Then, by use of empiric generation profiles [214, 215], the collection function in the direction of the depth coordinate z, $\phi(z)$, is calculated via $\xi I_{EBIC}(E_B) = \int_0^\infty \phi(z) g(E_B, z) \mathrm{d}z$. Here, ξ is a quantity containing the electron-beam current I_B, the electron-beam energy E_B, as well as the band-gap energy of the solar-cell absorber E_g (see also the collection efficiency further below in this subsection).
The following results are described more in detail in Ref. [77]. EBIC images were acquired on the backsurfaces of Cu(In,Ga)Se_2/CdS/ZnO stacks (see section 4.1.6 for details on the specimen preparation). In Fig. 5.33, various profiles extracted from EBIC images across GBs in Cu(In,Ga)Se_2 (Fig. 5 in Ref. [77]) and $CuInSe_2$ (Fig. 5.34b) thin films without irradiation by the electron beam are shown. There is no general behavior of the EBIC signal found for all the GBs investigated. At most GBs, the current exhibits a local minimum, with different minimum values. At some GBs, the EBIC is increased substantially with respect to the grain interiors. Asymmetric as well as symmetric EBIC distributions were found.
For GBs with enhanced EBIC signals with respect to the grain interiors (found at several GBs on both, $CuInSe_2$ and Cu(In,Ga)Se_2 backsurfaces), the current increases from both sides towards the GB, where the increase of the EBIC value starts in a distance of about 1000 nm from the GB. In addition, a local minimum in the EBIC signal is visible at the position of the GB, which exhibits a full width at half maximum of 50 to 100 nm. These shapes of the EBIC signals around GBs may be attributed to two effects on charge carriers with two different length scales (about 1 μm and 50-100 nm). While EBIC profiles across GBs with local minima at the position of the GB can be simulated by use of the theory introduced in Ref. [77], see also subsection "Quantification of EBIC signals at GBs" further below, it is currently not possible to provide an physical explanation for the increased EBIC at GBs.

EBIC, CL and EBSD data from identical positions SEM, EBIC, EBSD and CL data acquired on an identical position on the back surface of a $CuInSe_2$ thin film are shown in Fig. 5.34. The current values given by the EBIC images depend on the distance of the impinging electron beam to the contact wire and on whether the contact wire touches the back contact directly on the $CuInSe_2$ (also Cu(In,Ga)Se_2) surface or whether graphite is deposited on the absorber back contact. The EBIC signals acquired at 5 keV, 125 pA, and room temperature are higher with a graphite layer on the $CuInSe_2$ (Cu(In,Ga)Se_2) surface, likely because of the better conductivity and reduced surface recombination than for a $CuInSe_2$ (Cu(In,Ga)Se_2) thin film only. The monochromatic CL image (Fig. 5.34c) acquired at about 8 K, 8 keV, 1 nA, and at a wavelength of 1260 nm (band-gap energy of $CuInSe_2$) shows the spatial distribution

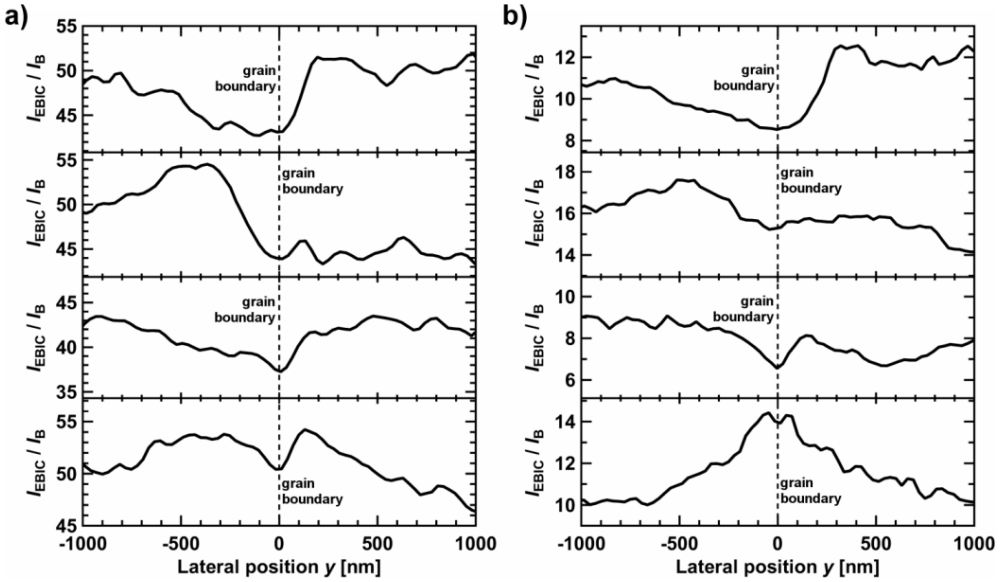

Figure 5.33: Profiles extracted from EBIC images recorded with an electron-beam energy of 8 keV at a) $Cu(In,Ga)Se_2$ and b) $CuInSe_2$ GBs on backsides of $Cu(In,Ga)Se_2$/CdS/ZnO stacks. All EBIC intensities were normalized by the beam current I_B.

of radiative recombination from the $CuInSe_2$ absorber. We note that up to date, we have not been able to acquire CL images from $CuInSe_2$ (also $Cu(In,Ga)Se_2$) thin films at room temperature with decent signal-to-noise ratios, which would be necessary for correlation of EBIC and CL images obtained at temperatures similar to working solar cells under sunlight.

The EBSD maps represent the diffraction pattern quality (Fig. 5.34d) and the orientation distribution (Fig. 5.34e) of the grains at the $CuInSe_2$ back surface. At the position of the grain boundaries, the pattern quality is very low (dark pixels) since EBSD patterns from neighboring grains superimpose. As a result, the added EBSD pattern cannot be indexed by the evaluation software. GBs can be classified by means of EBSD measurements, which provide the misorientations between all neighboring grains. The misorientation again is related to the symmetry of the GB. A highly symmetric type of GBs are those with a Σ value of 3 (the Σ value is explained in detail in Ref. [52] and in chapter 3.4.1). These $\Sigma 3$ GBs are highlighted in the pattern-quality map by white lines. Identifying unambiguously the Σ values of larger than 3 is not possible for GBs in polycrystalline $Cu(In,Ga)Se_2$ (or $CuInSe_2$) thin films. Thus, in the following, GBs are divided into $\Sigma 3$ (twin) and non-$\Sigma 3$ (random) GBs.
The EBIC and CL signals are not homogenous within the $CuInSe_2$ (also $Cu(In,Ga)Se_2$) thin films (disregarding effects at GBs). They are different for neighboring grains and also vary inside individual grains. The different orientations of the grains may influence the rates of backscattered electrons via channeling effects, i.e., the EBIC signal is reduced in case more electrons are backscattered. However, the EBSD data indicates that even for grains which exhibit similar orientations, the EBIC and the CL signals are different. We attribute the considerable variations of the EBIC and CL signals therefore rather to slight differences in net doping of the $CuInSe_2$ (also $Cu(In,Ga)Se_2$)

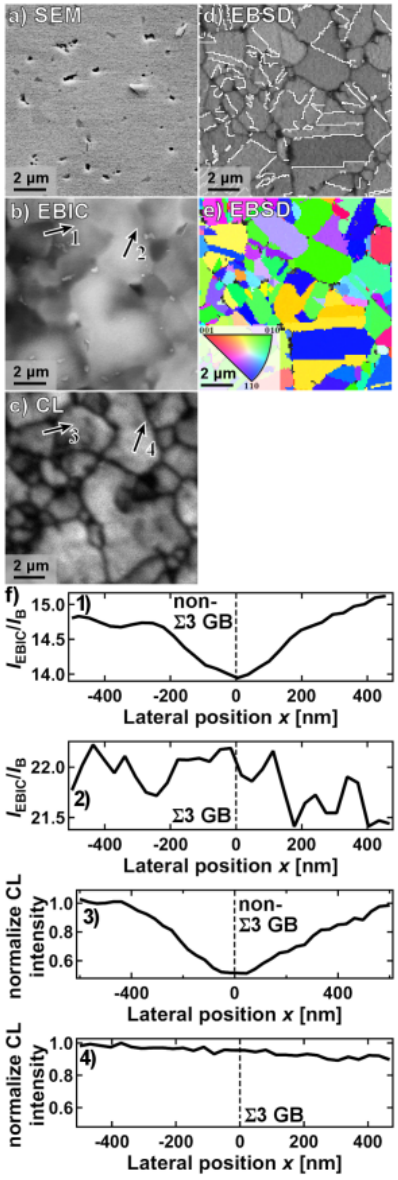

Figure 5.34: SE image (a), EBIC image at 5 keV, 125 pA, and room temperature (b), CL image at 8 keV, 1 nA, 8 K and at 1260 nm (c), EBSD pattern quality map (d) and EBSD orientation distribution map (e), all acquired at the identical position of backsurface of a $CuInSe_2$/CdS/ZnO stack as well as profiles across a non-Σ3 and a Σ3 GB (g). The white lines in the pattern-quality map (d) indicate the Σ3 GBs.

grain interiors.
From EBIC as well as from CL images obtained on the $CuInSe_2$ thin film, profiles (Fig. 5.34f) were extracted across a random and a $\Sigma 3$ GB. While EBIC signals were found to be reduced in some grains but enhanced in others (see Fig. 5.33), CL intensities were always found to be lower at random GBs (down to about 50 rel.%). $\Sigma 3$ GBs do not exhibit any significant influence on both the EBIC and CL signals. The EBIC and CL signals across $\Sigma 3$ and non-$\Sigma 3$ GBs in $CuInSe_2$ were found to be similar for other $Cu(In,Ga)Se_2$ thin films with different [Ga]/([Ga]+[In]) and [Cu]/([Ga]+[In]) ratios [217].

Quantification of EBIC signals at GBs In order to determine the diffusion length L and the recombination velocity S_{BC} at the back contact of a solar cell, EBIC measurements at different electron-beam energies E_{B} and thus different information depths are necessary. The procedure is described in Ref. [218]. In order to take losses via shunting paths and series resistances into account, a collection efficiency Σ can be defined as $\Sigma = c(E_{\mathrm{eh}} I_{\mathrm{EBIC}})/(E_{\mathrm{B}} I_{\mathrm{B}})$. The losses in the cell are described by a factor c, while E_{eh} is the energy to generate an electron-hole pair [1, 219], and I_{EBIC} is the measured or calculated current. Thus, together four variables influence the value of the current in dependence of the electron-beam energy E_{B}.
Measured and calculated collection efficiencies are shown in Fig. 5.35 for a $CuInSe_2$/CdS/ZnO stack, where EBIC images were acquired on the back surface of the $CuInSe_2$ layer. The width w_{SCR} of the SCR was estimated by a complementary capacitance measurement and using $w_{\mathrm{SCR}} = (\epsilon_0 \epsilon_{\mathrm{r}} A)/C$ (with ϵ_0 and $\epsilon_{\mathrm{r}} = 11.1$ [220] being the dielectrical permeabilities of vacuum and $CuInSe_2$, A the solar-cell area, and C the capacitance value) to about (570 ± 90) nm. The diffusion length L determined from the EBIC measurements is about 300 nm, the recombination velocity S_{BC} at the back contact about 8 $\times 10^4$ cm/s, and the factor for cell losses is $c = 0.26 \pm 0.04$. To show the influence of these parameters, each one of these is varied in Figs. 5.35a-d. The solid line in all graphs shows the best fit, which is not congruent with the measured data for all E_{B}. The higher slope of the measured data for $E_{\mathrm{B}} > 16$ keV, and the following bend of the curve can not be approximated well by the simulations. The higher slope is the result of the irradiation effect, as described in section 5.5.2.

Nevertheless, the extracted diffusion length L can be used as an approximation to estimate the effective diffusion length L_{eff} [4, 77] and finally to simulate the current distribution across a GB. The collection efficiency is calculated for both the simulation and the measured data. In Fig. 5.36, measured and simulated collection efficiencies are shown for one $CuInSe_2$ GB at $E_{\mathrm{B}} = 4$ and 6 keV. The estimated recombination velocity S_{GB} is in the range of about 10^3 cm/s, but the width of the simulated collection efficiencies is wider than the measured. Thus, with this simple model applied, it is not possible to provide a decent fit of simulation and experiment.

One approach for a better fit of the simulated and measured current distributions across $CuInSe_2$ GBs may be to assume a lower generation at the GB, as already suggested in the discussions given in the subsection "Discussion of EBIC and CL results" above. A corresponding width has to be assumed for the GB region as further parameter. For recombination velocities of larger than 0 cm/s, the decrease in EBIC at the GB would be higher assuming a band-gap energy of $E_{\mathrm{g}} = 1.3$ eV at the GB than assuming E_{g} =1.04 eV (band-gap energy of $CuInSe_2$ [116]). Thus, the simulation corresponds better to the measured data in Fig. 5.36. The estimated recombination velocity at this GB, assuming its width to be 20 nm, is in the range of $S_{\mathrm{GB}} = 2.5 \times 10^3$

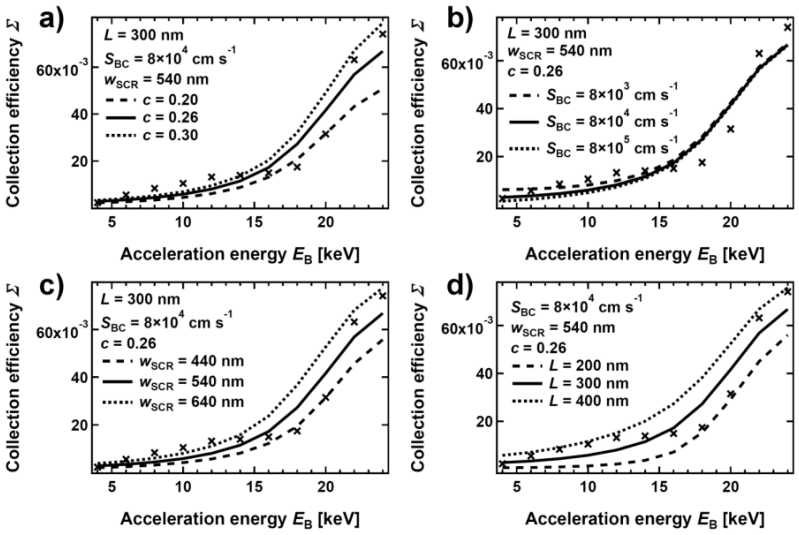

Figure 5.35: Measured (marked with cross) and calculated collection efficiencies for a $CuInSe_2$ solar cell investigated from the back contact with varied (a) diffusion length L, (b) recombination velocity at the back contact S_{BC}, (c) width of the SCR and (d) cell losses (c). The solid line in all diagrams represents the best fit to the measured data.

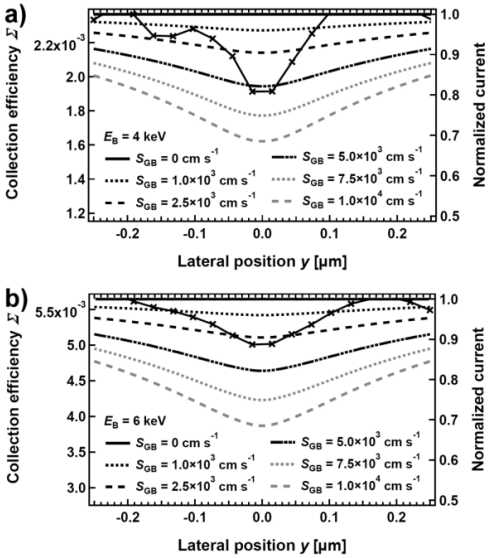

Figure 5.36: Measured (marked by crosses) and simulated collection efficiency Σ for various s_{GB} at a $CuInSe_2$ GB for $E_B = 4$ keV (a) and 6 keV (b).

cm/s, which agrees well with results from EBIC studies on cross-sectional solar-cell specimens (see subsection above). The comparison between the widths of measured and the simulated EBIC profiles around the GB in Fig. 5.37 suggests that the spatial resolution in the EBIC experiment is not better than about 50 nm.

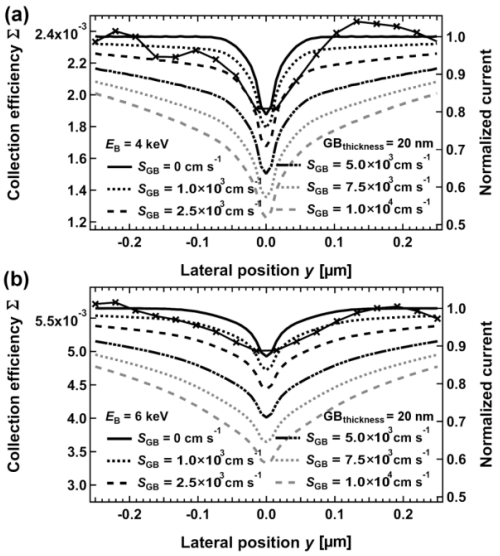

Figure 5.37: Measured (marked by crosses) and simulated collection efficiency Σ for various S_{GB} at one $CuInSe_2$ GB for $E_{\mathrm{B}} = 4$ keV (a) and 6 keV (b).

However, with the additional parameters band-gap energy at the GB (and thus change in the generation rate of electron-hole pairs) as well as the width of the GB, a total number of six simulation parameters have to be varied to fit the simulated curves to the ones given in Fig. 5.36. Even taking these additional parameters into account, it was not possible to reproduce the experimental data satisfactorily in the present work. Also, the model presented above is not able to simulate decently all EBIC profiles across non-Σ3 GBs obtained in the present work (see, e.g., those in Fig. 5.34). Especially for the EBIC profiles with local maxima at the GBs, no physically reasonable model can be provided by the authors. Thus, the one-dimensional model applied in the present work seems not to be appropriate entirely for simulating the EBIC profiles across non-Σ3 GBs in $Cu(In,Ga)Se_2$ thin films. Two-dimensional or even three-dimensional device simulations need to be conducted in future work.

5.5.3 Kelvin-probe force microscopy at grain boundaries

Kelvin-probe force microscopy (KPFM) is a technique applied in atomic force microscopy (AFM). The electrostatic force between the AFM tip and the sample is compensated by applying a dc bias to the sample, which corresponds to the contact potential difference (CPD). The CPD is given by the work function difference between the tip and sample material. To detect the CPD, an additional ac bias is applied. This bias induces an oscillation of the cantilever, which results from the electrostatic force between tip and sample. The induced oscillation of the cantilever at the frequency of the ac bias is reduced to zero, when the dc bias is controlled to match the CPD. The work function of the tip can be calibrated on a reference sample with a known

work function (e.g., highly oriented pyrolytic graphite). Thus, the work function of the sample can be determined [221].
A more detailed description of the following results is given in Ref. [139]. Fig. 5.38 shows an identical surface location on the $CuInSe_2$ film studied, obtained by the different techniques applied. The size of all images is 9.0 μm×11.3 μm. EBSD maps and KPFM images were re-calibrated based on the SEM micrograph, since the original images were distorted due to non-normal incidence of the electron beam on the surface, a non-linear expansion of the KPFM-piezos, and thermal drift.

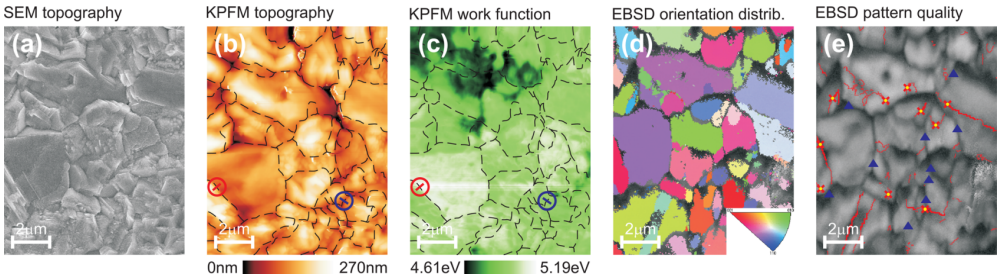

Figure 5.38: 9.0 μm×11.3 μm images from an identical location on a $CuInSe_2$ thin film. (a) SEM image, (b) KPFM topography image, (c) KPFM work function image, (d) EBSD orientation distribution map, and (e) EBSD pattern quality map. In (b) and (c) the position of GBs is indicated by dashed lines, as deduced from the EBSD orientation distribution map. In (e), Σ3 GBs are highlighted by red lines. The positions of Σ3 GBs analyzed in Fig. 3 are indicated by red crosses with yellow dots. The positions of the non-Σ3 GBs analyzed in Fig. 5.39 are marked by blue triangles. From Ref. [139].

Ultimately, it was possible to evaluate 10 different Σ3 GBs and analyze their charge states by extracting profiles from the work function image. The positions of these GBs are indicated in Fig. 5.38(e) by red crosses. In addition, the charge states of 10 non-Σ3 GBs were evaluated as well. In both cases, the symmetry information was obtained from the EBSD measurement. Fig. 5.39 shows a summary of this evaluation, displaying the electronic properties of Σ3 GBs and non-Σ3 GBs. 9 out of 10 Σ3 GBs are charge-neutral; only one Σ3 GB exhibits a negative potential barrier of -45 mV (the measurement errors are about ± 5 mV). For non-Σ3 GBs, in contrast, only 4 out of 10 GBs do not show any evidence for charges. The remaining 6 GBs exhibit both positive and negative potential barriers, in a range from -90 to +37 mV. Note that the finding of both positive and negative potential barriers is typical for Cu(In,Ga)Se_2 GBs [141]. In this respect, one has to consider that nanoscale potential variations measured by KPFM are subject to an averaging effect through the tip and the cantilever. At a tip-sample distance of d≈10 nm, as used for the given experiments, only about 25% of the full potential barrier is detected [222].

5.5.4 Scanning capacitance microscopy at grain boundaries

EBSD was also combined with scanning capacitance microscopy (SCM) on same identical positions [140]. The authors showed that most Σ3 (twin) boundaries did not exhibit substantial signal changes, whereas the spatial variations in dC/dV suggested p-to-n type inversion at all non-Σ3 grain boundaries.

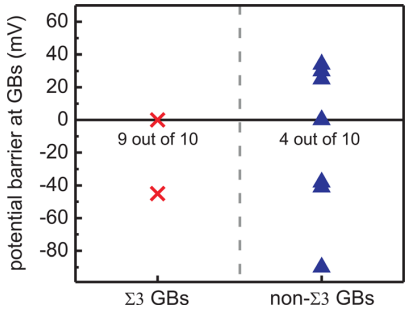

Figure 5.39: Electronic properties of GBs in $CuInSe_2$, shown separately for Σ3 GBs and for non-Σ3 GBs. The symmetry information was obtained from the EBSD measurement. The black numbers indicate the number of electronically inactive GBs. From Ref. [139].

5.5.5 Atom-probe tomography at grain boundaries

Atom-probe tomography (APT) offers analysts the opportunity to examine inorganic and organic materials with a three-dimensional image made up of detected atoms or small molecules (up to 60% detection efficiency) with high spatial resolution (in principle, better than 0.3 nm achievable in all directions) and high analytical sensitivity (as good as 1 ppm) over volumes of greater than 10^6 nm^3 (100 nm × 100 nm × 100 nm). The reader is referred to Refs. [223, 224] for overviews on this technique. It should be noted that for semiconductors as $Cu(In,Ga)Se_2$ thin films, laser-enhanced APT is not able to resolve elemental distributions at the subnanometer scale. To our experience, lateral resolutions are in the range of about 1-2 nm for $Cu(In,Ga)Se_2$ (1 nm has been reported for Si heterostructures [225]).
The following results were taken from Ref. [93]. Fig. 5.40 gives elemental distribution profiles acquired by APT across a GB in a $Cu(In,Ga)Se_2$ thin film. Being a mass spectrometry technique, APT allows for the detection of also trace elements apart from the matrix elements in $Cu(In,Ga)Se_2$. The Cu signal is enhanced at this GB, whereas that of In is reduced. The Ga and Se concentrations exhibit minima, and Na, K, H as well as O are apparently enriched at the GB. While Na enrichments at GBs in $Cu(In,Ga)Se_2$ have already been published by several other authors [175,176,226] only one previous work [177] as shown so far additionally also enhanced O and K signals. Na, O and K are present as Na_2O and K_2O in the soda-lime glass used as substrate for the solar-cell stack, probably diffusing into $Cu(In,Ga)Se_2$ during the growth process, whereas H and again O may also stem from the residual gas in the APT instrument.

Further APT analyses at GBs in $Cu(In,Ga)Se_2$ thin films with various compositions and growth conditions (data not given in the present work) were performed. It was found that the Se concentration is sometimes increased, sometimes decreased or does not change significantly. The Ga signal does not always show the same behavior as the In signal, and for some GBs, it does not change significantly. At most GBs analyzed, Na and O are enriched. Based on numerous measurements by APT (see also Ref. [227]), we can exclude that the variety of compositional changes at GBs is due to measurement artefacts.
Although there is no clear trend for the compositional changes at different GBs, APT results have one detail in common. If the Cu signal is increased at the GB, the In signal is reduced, and vice versa (see also Ref. [228]). This anticorrelation of the Cu and the

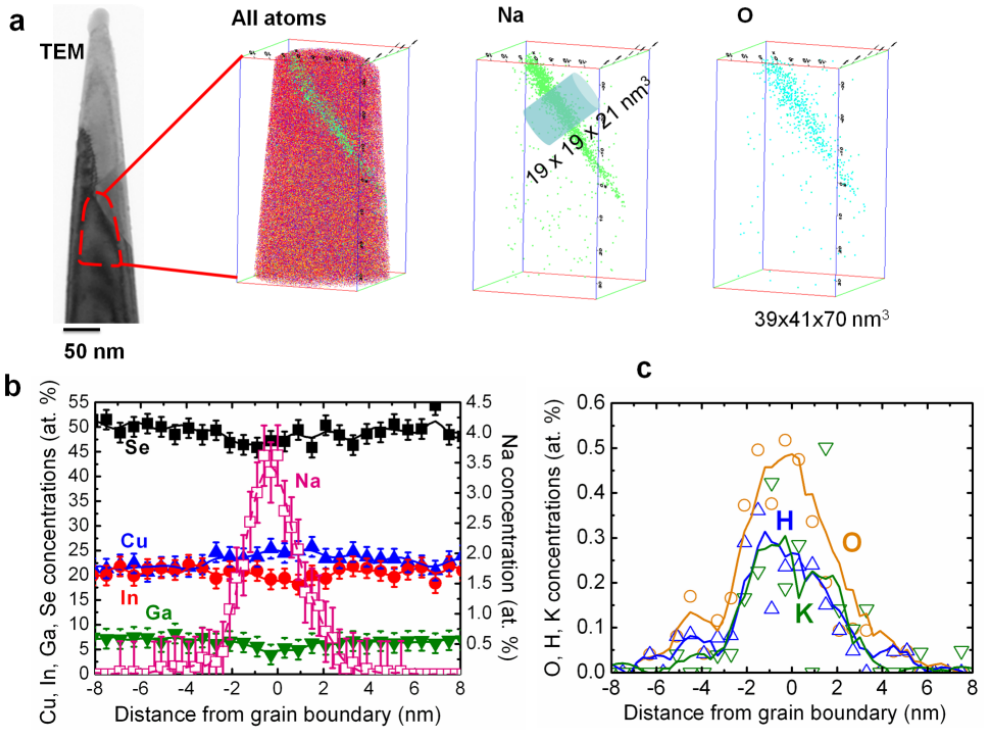

Figure 5.40: Results from atom-probe tomography performed on Cu(In,Ga)Se_2 thin-film. a) Bright-field TEM image of the tip containing a GB (identified by diffraction contrast), as well as corresponding reconstructed, three-dimensional data cube giving the elemental distributions by false colors. Extracted elemental distribution profiles from this data cube are given in b) for Cu (blue up triangles), In (red circles), Ga (green down triangles), Se (black full squares), and Na (pink open squares), as well as in c) for O (yellow open circles), H (blue open triangles), and K (green open triangles). All lines are guides for the eyes. The errors of the concentrations in b) were estimated to about 2 at.% (Cu, In, Ga, Se) and to about 0.5 at.% (Na). In c), no error bars are given to provide better visibility of the data. However, the scattering of the raw data in this viewgraph is apparent. From Ref. [93].

In concentrations gives strong indication for atomic redistribution at the GBs; this is because almost all atomic planes in the tetragonal Cu(In,Ga)Se_2 crystal structure are occupied by Cu and In (and Ga) (only the {101} planes contain either only Cu or only In (and Ga) atoms).
It should be noted that for so far the only APT analysis at GBs in Cu(In,Ga)$(S,Se)_2$ thin films, the mentioned anticorrelation was not confirmed for all GBs. Probably, this result may be due to the presence of sulfur in the crystal structure.

5.5.6 Electron energy-loss spectrometry and electron holography at grain boundaries

As already lined out in section 4.4, correlative analysis of compositional and electrical properties of extended structural defects can be conducted by means of electron energy-loss spectrometry (EELS) and inline electron holography in a transmission electron microscope. First of all, high-resolution scanning TEM imaging and EELS analysis can be combined to determine structural and compositional properties of (random) GBs at the subnanometer scale. Details on this study can be found in Ref. [194]. In contrast to the Σ3 TBs, the EELS result obtained at the random GB shown in Fig. 5.41a shows Cu and O enrichments as well as In depletion at the position of the GB (Fig. 5.41b). The Se signal does not change significantly. The region around the GB where compositional changes are detected (about 0.7 nm full width at half maximum) is very narrow. By comparison with the HR-STEM image in Fig. 5.41a, this region corresponds well to the two atomic planes closest to the GB (dashed lines).
At yet another (random) GB in the identical Cu(In,Ga)Se_2 thin film (see Supplemental Results of Ref. [194]), copious Se depletion was found, while the Cu, In, and oxygen signals behave similarly as in Fig. 5.41b. Especially in these elemental distribution profiles, the anticorrelations of Cu and In signals as well as of Se and oxygen signals are apparent.

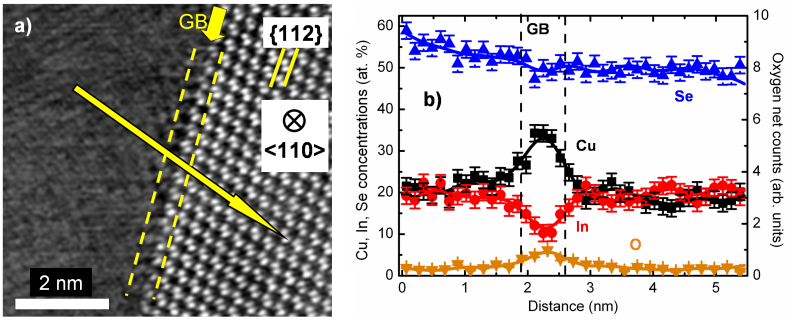

Figure 5.41: High-resolution STEM image (a) of a random (non-twin) GB (indicated by small arrow). EEL spectra were acquired along the large arrow given in (a), and elemental distribution profiles were extracted from these spectra (b). The region where compositional changes are detected are highlighted by dashed lines. Cu and O enrichments as well as In depletion are found at the position of the GB, while the Se signal does not change significantly. The, Cu, In, and Se signals were quantified by relating the average net counts in the grain interiors to the integral concentrations determined by X-ray fluorescence analysis. The error bars were estimated from the systematic errors at 10% of the measured values.

EELS measurements at random GBs in several further Cu(In,Ga)Se_2 thin films with various [Cu]/([In]+[Ga]) ratios confirmed these results, also showing changed compositions at these GBs, with Cu and In signals always being anticorrelated, while Se depletion and O enrichment have been measured only in some cases. Except for these anticorrelations of Cu/In and of Se/O signals, there is not any general trend in compositional changes found at Cu(In,Ga)Se_2 GBs. We have found them to be in part enriched (depleted), and in part also depleted (enriched) in Cu (In). The anticorrelation of Cu and In signals always present at Cu(In,Ga)Se_2 GBs indicates a preferential site exchange of Cu and In atoms, leading to the formation of In_{Cu}^{2+} and Cu_{In}^{2-} antisites. However, also the formation of V_{Cu}^{-} (Cu vacancies) and neutral defect complexes as $(2V_{Cu}^{-} + In_{Cu}^{2+})$ and $(Cu_{In}^{2-} + In_{Cu}^{2+})$ have to be considered [229].
From the EELS data acquired, we did not detect enhanced Na and O signals at TBs down to the detection limit of about 1 at.%. Enhanced O signals were, in contrast, detected at random GBs by means of EELS. EELS analyses of GBs can be correlated with electron holography data in order to obtain information on the electrical properties of GBs. Details on this study can be found in Ref. [93]. It is possible to correlate the electrostatic potential wells at Cu(In,Ga)Se_2 GBs directly to changes in composition. Profiles of $\Delta V_{av}(V)$ and profiles evaluated from EELS measurements in a scanning TEM, both obtained across the identical GB in a Cu(In,Ga)Se_2 thin-film, are given in Fig. 5.42. It can be seen that the In and O signals are enhanced, whereas the Cu and Se signals exhibit minima at the position of the GB (note that O may also be introduced in part during the TEM specimen preparation). The Ga-L edge in the EEL spectrum was superimposed by the Cu-L edge, and was therefore not evaluated. The widths of the minima and maxima in the EELS signals match the width of the electrostatic potential wells (1-2 nm). Using the concentrations of Cu, In, and Se (Fig. 5.42) as well as the resulting concentration of Ga (assuming [Cu]+[In]+[Ga]+[Se]=1 integrally in the Cu(In,Ga)Se_2 layer, which is not given at the GB in view of the O signal and other impurities possibly being present), their corresponding scattering factors [179], as well as the lattice constants for the tetragonal crystal structures of $CuInSe_2$ [230] and of $CuGaSe_2$ [231], the resulting change in MIP was calculated by use of Eq. 4.5. With the compositional changes given in Figure 5.42, we are able to estimate a lowering of the MIP of about 3.3 V, which is in good agreement with the depths of the measured potential wells of about 1.6-1.8 V. The discrepancy can be explained by assuming that additional O, which was not considered in the estimation, and other impurities increase the MIP such that the depth of the potential wells becomes about 1.6-1.8 V.
By combined EELS and electron holography measurements on the same identical position of a Cu(In,Ga)Se_2 GB (Fig. 5.42), it was shown that the averaged electrostatic potential wells can be explained best by a change in composition. The regions of the GBs in Cu(In,Ga)Se_2 thin films where changes in composition occur are strongly confined to only about 1 nm in width, i.e., to the atomic planes nearest to the GB core.

5.5.7 Further investigations at grain boundaries

In the following, further results from investigations of various GB properties are detailed. In most of these investigations, the positions of the GBs were determined by means of contrasts in scanning electron or atomic force micrographs, which may be misleading owing to imaging artifacts by surface roughnesses or impurities.

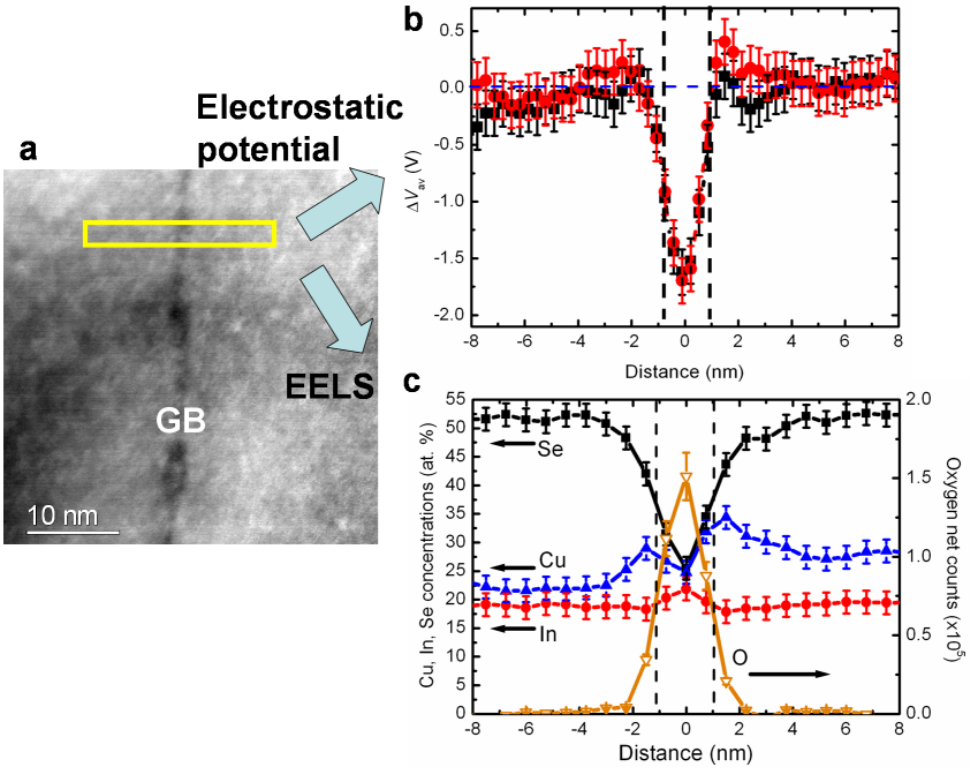

Figure 5.42: a) High-angle annular dark-field image of a position containing a random (non-twin) GB (the dark spots are related to carbon contaminations). Across this GB, distributions of the electrostatic potentials (b) were obtained (where these two profiles were acquired at two different positions on this GB), as well as elemental distribution profiles by means of EELS (c). The region of change in electrostatic potential and in composition is confined to 1-2 nm. The measured potential wells can be attributed directly to a change in composition. Enrichment of In and O as well as depletion of Cu and Se were detected. The errors of measurement for the electrostatic potential were assumed to be about 0.2 V, those of the Cu, In, and Se concentrations, quantified by integral X-ray fluorescence analysis of the Cu(In,Ga)Se_2 thin-film, to about 2 at.%, and the errors for the oxygen net counts about 10 rel.% of the corresponding values.

Surface composition by scanning Auger-electron microscopy

Hetzer et al. [203, 204] analyzed GBs in Cu(In,Ga)Se_2 thin films by means of scanning Auger-electron microscopy (SAEM) in a scanning electron microscope. Linescans by SAEM showed Cu depletion and In enrichment at GBs with reductions of the [Cu]/([In]+[Ga]) compositional ratio in the order of up to 50%. It should be noted that SAEM detects these compositional variations only at the very surface (about 1 nm depth) of the analyzed Cu(In,Ga)Se_2 thin film. No information of bulk compositions at or around GBs is provided.

Work function by Kelvin-probe force microscopy and scanning electron threshold measurements

The following analyses probe also only the surface of the polycrystalline Cu(In,Ga)Se_2 thin film. Until today, numerous studies have been conducted using Kelvin-probe force microscopy [133–135, 139, 140, 143, 201, 232–234]. A difference in contact potential can be translated into a difference in work function, which again may be equivalent to the bending of the valence band, if due to a redistribution of free charges (according to Poisson's equation). It should be mentioned that until about 2010, consistently, only down-bending of the bands at Cu(In,Ga)Se_2 GBs has been detected. Then, the influence of surface oxidation on the KPFM signal has been identified, and a KCN treatment of Cu(In,Ga)Se_2 surfaces prior to KPFM measurements was proposed, in order to reduce the surface oxidation [235]. From 2011 on, down- and up-bending as well as no band bending has been reported [138–140, 143, 234], with values of up to about ± 400 meV, which is in good agreement with values obtained by scanning electron threshold measurements [203, 204]. On Na-free Cu(In,Ga)Se_2 layers, the changes in work function measured by KPFM are substantially reduced [134, 201, 236].

Transport by Hall measurements, conductive atomic force and electron-beam-assisted scanning tunneling microscopy

Temperature-dependent transport measurements have given indications of grain-boundary barriers for electron diffusion of about 30-100 meV in height [237–241]. It should be mentioned that these barrier heights reach values of up to 350 meV for Na-free Cu(In,Ga)Se_2 thin film [238]. By means of electron-beam-assisted scanning tunneling microscopy, Romero et al. [242] found substantial electron barriers present at GBs in polycrystalline $CuGaSe_2$ but not in $CuInSe_2$. Results from conductive atomic force microscopy [243, 244] have shown higher dark current at GBs, which is interpreted in terms of p-to-n type inversion. It should be noted that for transport measurements in general, it is not always clear which path the current takes (surface versus bulk). Also, when contacting a surface by a tip (in scanning probe microscopy), the transport is influenced by the surface condition, which is mostly not considered nor discussed (see also the issue of surface oxidation mentioned above).

Local doping concentrations by scanning capacitance microscopy

Changes of $\mathrm{d}C/\mathrm{d}V$ signals obtained by scanning capacitance microscopy at GBs [140, 244], as compared with the grain interiors in Cu(In,Ga)Se_2 thin films, indicate p-type to n-type inversion at GBs. Again, a possible influence of the surface condition is not discussed by the authors, although the measurement is influenced substantially by the contact of the tip with the surface.

Density of states by scanning tunneling spectroscopy

Moenig et al. [245] calculated dI/dU characteristics from scanning tunneling spectra, giving direct evidence for a reduced density of deep level defects at Cu(In,Ga)Se_2 GBs. These authors show also simulations of this data which point to a high density of defect levels in resonance with the bottom end of the conduction band, which do not extend into the band gap. Reduced densities of states at GBs as compared with the grain interiors was confirmed by Azulay et al. [246], who also demonstrated p-type to n-type inversion and band bending only at GBs in Cu(In,Ga)Se_2 layers with [Ga]/([Ga]+[In]) ≤ 0.33 but not for thin films with [Ga]/([Ga]+[In]) ≥ 0.75. As for other scanning probe techniques, the measurement is influenced substantially by the contact of the tip with the surface.

Different doping levels in neighboring grains

When discussing the properties of GBs in Cu(In,Ga)Se_2 thin films, it should be mentioned that the doping distribution within these thin films is not at all uniform. Measurements by scanning spreading resistance microscopy [199], EBIC [77] and CL [132] give indications for different doping levels in neighboring grains. This fact is equivalent to the presence of electrical fields across GBs and therefore needs to be taken into account when concluding on their electrical properties.

5.5.8 Two-dimensional device modeling of the roles of grain boundaries

Influences of GBs on the device performance of Cu(In,Ga)Se_2 solar cells were treated in terms of two-dimensional device modeling by various publications [35–38, 187]. It should be noted that such device simulations have so far not accounted for the complex nature of GBs in Cu(In,Ga)Se_2 thin films, which was outlined in the preceding subsections in terms of, e.g., always different changes in composition and electrical/optoelectronic properties.
Consistently, these simulations can not identify any possible scenario of enhanced solar-cell performance in devices with polycrystalline Cu(In,Ga)Se_2 thin films than in case of layers without GBs. It was found that the band bending around a GB confines the short-circuit current density j_{sc} towards the GB [36, 38], a situation also found in experiments [243]. However, this fact does by no means imply that the average j_{sc} is increased by the GB. In most situations, the recombination losses that occur if the minority carriers travel along the GB lead to an overall decrease of j_{sc} [247].
Down-bending of the bands, leading to a hole barrier of larger than 0.4 eV indeed increases the short-circuit current density j_{sc}, however, at the expense of photovoltage and the overall power-conversion efficiency [35,36]. A reduced valence-band maximum ΔVBM at the GB [181,182], representing to a hole barrier, would lead to similar device performances as in GB-free solar cells for values of ΔVBM ≥ 0.4 eV. A comparable result is obtained when assuming a combination of a large valence-band offset (≥ 0.3 eV) and modest hole-repulsive band bending (0.1 eV) [35]. It was pointed out by Taretto et al. [38] that the width of the hole barrier needs a thickness of at least 3 nm in order to prevent holes from effective tunneling to the GB, which would increase again the probability of recombination.

5.5.9 Summary on grain-boundary properties in Cu(In,Ga)Se_2

This subsection may be divided into considerations concerning charge densities and changes in atomic (mass) density at GBs in Cu(In,Ga)Se_2 thin films, and corresponding consequences on the optoelectronic properties of GBs. Evidence on charged GBs have only been given by techniques sensitive to the surface of a Cu(In,Ga)Se_2 thin film. Electron holography has not shown any dominant contributions of charge densities at GBs in the bulk of the Cu(In,Ga)Se_2 layer. Moreover, the published band bending of up to 400 meV needs to be regarded in connection with different doping levels in neighboring grains. We may conclude that charged GBs are features present mainly at the surfaces of Cu(In,Ga)Se_2 thin films (which may be understood in terms of higher densities of dangling bonds at surfaces). Especially in view of that in order to complete solar cells, buffer/window layers as CdS/ZnO are deposited on top of these surfaces, the question is to which extent charge densities remain at GBs after these depositions. On the other hand side, compositional changes have been detected by various techniques at GBs. The result of different changes in composition with anticorrelated Cu and In signals at various GBs in Cu(In,Ga)Se_2 thin films gives rise to a structural GB model, which is outlined in the following. It is important at this point to note that for high-efficient, thin-film solar cells, non-stoichiometric Cu(In,Ga)Se_2 layers are used, with typical concentration ratios of [Cu]/([In]+[Ga])=0.8-0.9. A certain fraction of the Cu sites in the chalcopyrite-type lattice (depending on the deposition recipe of the Cu(In,Ga)Se_2 thin film under investigation) are vacancies (see Fig. 5.43). This is one reason why Cu exhibits a high mobility in Cu(In,Ga)Se_2 thin-films [186], which also promotes the formation of In_{Cu}^{2+} and Ga_{Cu}^{2+} point defects.
As listed in Fig. 5.43, the number of intrinsic and impurity-induced defects is rather large. V_{Cu}^{-}, Cu_{In}^{2-}, and Cu_{Ga}^{2-} may lead to acceptor states in the electronic band gap, whereas V_{Se}^{2+}, In_{Cu}^{2+}, and Ga_{Cu}^{2+} give rise to donors. Moreover, it was shown [229] that the defect pairs ($2V_{Cu}^{-}$ + In_{Cu}^{2+}) and (Cu_{In}^{2-} + In_{Cu}^{2+}) have particularly low formation enthalpies. Considering the striking anticorrelation of all Cu and In signals at Cu(In,Ga)Se_2 GBs found in numerous measurements, it may be that the concentrations of these neutral defect complexes are particularly high at Cu(In,Ga)Se_2 GBs.
Segregation of the impurities Na, K, and O at GBs implies the formation of the impurity-induced point defects Na_{Cu}, K_{Cu}, and O_{Se}, which are quasi-neutral but result in the formation of weak donors and weak acceptors because of the different electronegativities of O and Se as well as of Na, K, and Cu. The overall GB energy can be lowered by atomic or ionic redistribution in atomic planes adjacent to the GB core. Since different growth conditions and different densities of segregated impurities (due to different glass substrates used or due to different growth recipes applied) can result in various situations at GBs in Cu(In,Ga)Se_2 layers, the atomic/ionic redistribution is not equal for all GBs. Therefore, the GBs differ in general in their compositions, i.e., for differently grown and also within identical Cu(In,Ga)Se_2 thin films.

Consequences for an electronic band diagram in the vicinity of a Cu(In,Ga)Se_2 GB are difficult to be detailed. The point defects V_{Cu}^{-}, Cu_{In}^{2-} and Cu_{Ga}^{2-} as well as V_{Se}^{2+}, In_{Cu}^{2+}, and Ga_{Cu}^{2+} are also present in the grain interiors [248, 249] forming acceptor and donor states in the band gap, making Cu(In,Ga)Se_2 a highly compensated semiconductor. According to the considerations given above, their densities are increased at the GBs. Assuming varying compositional changes at different GBs, the band diagrams are expected to exhibit various "band offsets" in conduction and valence bands at the positions of the GBs.
The structural model of confined and chemically flexible GBs in the present work can

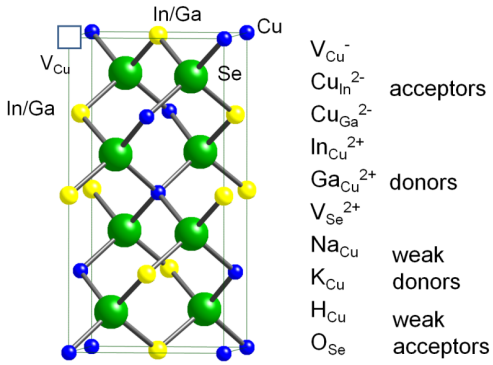

Figure 5.43: Unit cell of the tetragonal, chalcopyrite-type crystal structure of Cu(In,Ga)Se_2, comprising vacancies on the Cu sites. Intrinsic point defects and those induced by impurities are listed, indicating whether they are expected to form donor or acceptor states.

not exclude any of the various other GB models for Cu(In,Ga)Se_2 thin films reported in the literature. Charge accumulation at Cu(In,Ga)Se_2 GBs [59,133,135,232,233,240] has to be considered, however, a dominant role can be excluded.
Atomic reconstruction at Cu(In,Ga)Se_2 GBs has already been suggested by Persson and Zunger [181,182] based on density functional theory (DFT) calculations on highly symmetric $\Sigma 3$ twin GBs. However, these authors predict the formation of Cu vacancies or In_{Cu}^{2+} antisite defects, while we found various changes in Cu and In concentrations, and also further compositional variations. The confinement of the GB to only about 1 nm in width is closely related to the neutral (tunnelling) barrier proposed by Azulay et al. [243] as well as by Hafemeister et al. [197], only that the negative valence-band offset proposed by these authors is again most probably not found at all GBs. A (quasi) charge-neutral GB without (or with hardly) any band bending or band offset was suggested by Yan et al. [137]. From DFT calculations, these authors suggest very low densities of deep defects in the band gap (for which experimental evidence has been provided by Moenig et al. and Azulay et al. [245,246]) due to lattice relaxations, which can be related to the atomic/ionic redistributions found by the present work. This would be a good explanation for the low recombination velocities of about $10^3 - 10^4$ cm/s measured at Cu(In,Ga)Se_2 GBs [198]. Although atomic redistibution may compensate for charge at the GBs, it can not be concluded from the results given in the present work that charge neutrality is a general feature of a Cu(In,Ga)Se_2 GB.

5.6 Macrostrain/macrostress and microstrain in polycrystalline Cu(In,Ga)Se_2 thin films

Up to now, only very few reports are available concerning investigations of strain/stress contained in the microstructure of Cu(In,Ga)Se_2 thin films, although, apparently, all other extended structural defects are connected with this three-dimensional feature. We may divide the present section into results from measurements of residual macrostress/macrostrain obtained on large areas (over large number of grains) within Cu(In,Ga)Se_2 thin films, and microstrain contained within individual grains.

5.6.1 Residual macrostress and macrostrain

First values for strain/stress in Cu(In,Ga)Se_2 thin films were determined by Chakrabarti et al. [239, 250] by evaluation of subgap absorption. Macrostresses were determined to be in the order of 1 GPa, with corresponding macrostrain of about 10^{-3}. For $CuInS_2$ thin films, Thomas [251] determined macrostress values of about 50 MPa. Recently, X-ray diffraction analyses were performed on $CuInSe_2$ layers (M. Klaus, C. Genzel, Helmholtz-Zentrum Berlin, Germany, unpublished data) using the $\sin^2\psi$ method [252]. Values of about 100 MPa for the macrostress and about 10^{-4} for the macrostrain were found.

5.6.2 Microstrain

First microstrain measurements within individual grains of $CuInSe_2$ and $CuGaSe_2$ thin films were performed [253] by evaluating the EBSD patterns obtained on these layers, using the software CrossCourt (BLG Productions, Bristol, UK, http://www.blgproductions.co.uk), which is based on the work by Wilkinson et al. [66]. See Figs. 5.44 and 5.45 for examples. As visible in the distributions of the strain components ϵ_{11}, ϵ_{22}, and ϵ_{33} in these images, strain values are in the order of 10^{-4}. Especially in the data shown in Fig. 5.45, the strain distributions seem to be related to the presence of certain linear and/or planar structural defects.

Since the $CuInSe_2$ thin film was the same as analyzed by means of the $\sin^2\psi$ method (see above), the result means a good agreement of the macrostrain and the microstrain by the X-ray diffraction and electron microscopy methods. In addition, also on this $CuInSe_2$ thin film, X-ray microdiffraction was performed on individual grains showed similar microstrain values, again in the order of 10^{-4} (Thomas Schülli, ESRF Grenoble, unpublished data).

In contrast to microstrain in $CuInSe_2$ and $CuGaSe_2$ thin films (in the order of 10^{-4}), the strain values associated with Ga gradients within individual Cu(In,Ga)Se_2 grains (see section 5.3.2) are in the order of 10^{-2} (few %). The threshold between the regimes for elastic and plastic deformation was determined to a change of the Ga concentration of 12-13 at.%/μm or a corresponding strain value of about 1%. This means, the microstrain determined within individual grains in $CuInSe_2$ and $CuGaSe_2$ thin films is far below this threshold and entirely elastic deformation of the atomic lattice.

To date, there have been no investigations on the influences of strain distributions on the photovoltaic performances. However, strain fields are in connection with other extended structural defects, i.e., dislocations, stacking faults, twins, and grain boundaries, whose impact on the solar-cell operation has been discussed in the previous sections above. Also, especially when the strain values are in the order of few %, the mobility of charge carriers may be affected substantially, as reported for microelectronic devices (see, e.g, Ref. [254]). The effect can be attributed to larger interatomic distances for compressive or tensile stress applied, allowing for faster switching of the corresponding semiconductor devices. In general terms, a strained atomic lattice implies changes in the electronic band diagram. Systematic analyses of this matter are needed in order to determine possible consequences for the collection or recombination of charge carriers.

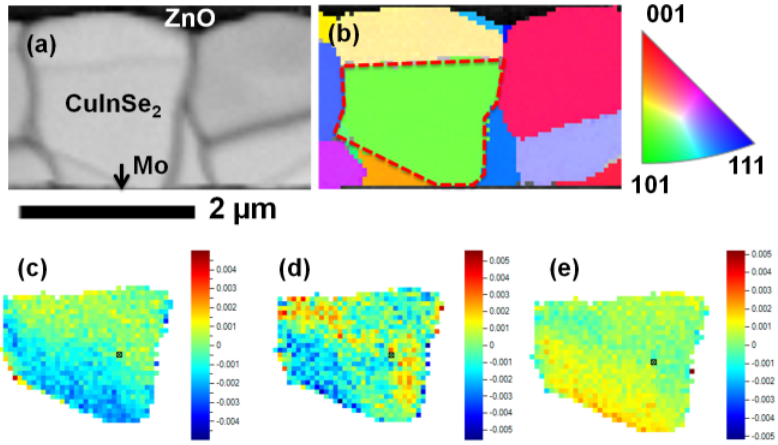

Figure 5.44: EBSD pattern-quality (a) and orientation-distribution maps (b), acquired on a cross-section of a ZnO/CdS/$CuInSe_2$/Mo/glass stack, with the local orientations given as false colors, see legend. Spatial distributions of the train components ϵ_{11} (c), ϵ_{22} (d), and ϵ_{33}, across the grain highlighted by dashed line in (b). Data by courtesy of N. Schäfer, HZB, Berlin.

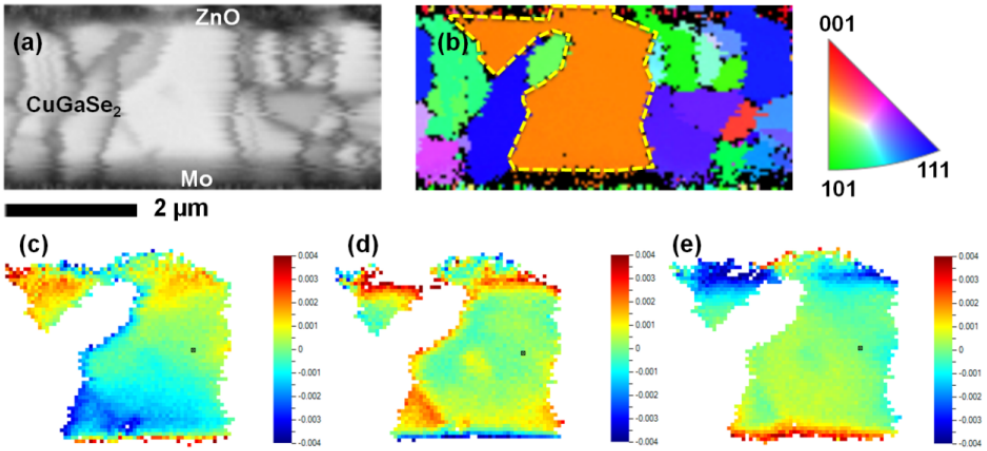

Figure 5.45: EBSD pattern-quality (a) and orientation-distribution maps (b), acquired on a cross-section of a ZnO/CdS/$CuGaSe_2$/Mo/glass stack, with the local orientations given as false colors, see legend. Spatial distributions of the train components ϵ_{11} (c), ϵ_{22} (d), and ϵ_{33}, across the grain highlighted by dashed line in (b). Data by courtesy of N. Schäfer, HZB, Berlin.

5.7 Conclusions of the present chapter

The application of microscopy techniques to extended structural defects in semiconductor devices and their possible impact on the device performance was discussed using the example of polycrystalline Cu(In,Ga)Se_2 thin-film solar cells. It was demonstrated that especially the combination of various techniques on same identical specimen areas provides insight into various properties of extended structural defects. This correlative microscopy approach is particularly important for complex material systems such as polycrystalline Cu(In,Ga)Se_2 thin-film solar cells, with a microstructure on the submicrometer level, a large number of matrix and impurity elements (and correspondingly a large number of point defects in a highly compensated semiconductor), as well as various extended structural defects possibly influencing the device performance. It was shown that it is of advantage to probe the various properties on different scales, for appropriate (subnanometer) resolutions at interfaces and extended structural defects, as well as, for good statistics, on areas in the order of hundreds of micrometers to millimeters.

For dislocations in Cu(In,Ga)Se_2 thin films, a structural model was proposed, which is based on atomic reconstruction of the dislocation core and the neighboring atomic lines of the inserted half plane, in order to (at least partly) compensate for excess charge densities. Similar reconstruction was also found when studying twin boundaries. Since these planar defects are special cases of stacking faults, reconstructed atomic lines and planes at and around extended structural defects can be expected at all linear and highly symmetric, planar defects in polycrystalline Cu(In,Ga)Se_2 layers. As for most twin boundaries, various electrical and optoelectronic analyses showed not any substantial changes of the measurement signals, as compared with those in the grain interiors. The assessment of electrical properties of (partial) dislocations and stacking faults as well as the calculation of the corresponding electronic band diagrams around linear and highly symmetric, planar defects is still work in progress.

The issue of low-symmetrical, random GBs is more complicated. It was demonstrated that in contrast to multicrystalline Si, the GBs in Cu(In,Ga)Se_2 thin films do not reduce the short-circuit current substantially (only 5-10%). At several random GBs, the EBIC signals even were found to be enhanced. This result agrees well with the fact that highest short-circuit current densities of Cu(In,Ga)Se_2 solar cells are very close (94%) to the radiative Shockley-Queisser limit (see Table 5.1). On the other hand, the signals measurement by means of CL at random GBs are substantially reduced, which can be explained by enhanced nonradiative (SRH) recombination, but also by reduced generation (e.g., for a smaller band-gap energy at the position of the GB). In the scope of the present work, it was not yet possible to identify unambiguously the reason for the reduced CL signals. Thus, a direct link between (possibly) enhanced nonradiative (SRH) recombination at GBs (and generally at extended structural defects) and the limited open-circuit voltage of Cu(In,Ga)Se_2 solar cells (Table 5.1) was not assessed.

First microstrain distribution measurements within individual $CuInSe_2$ and $CuGaSe_2$ grains show values in the order of 10^{-4}, i.e., well in the elastic deformation regime. Plastic deformation associated with high densities of dislocations in the order of $10^{10} - 10^{11}$ cm^{-2} is expected for Cu(In,Ga)Se_2 grains containing substantial Ga gradients larger than about 12-13 at.%/μm (about 1% strain). Possible impacts of microstrain (or macrostrain) on the photovoltaic performances of Cu(In,Ga)Se_2 solar cells are still under investigation.

Overall, it remains challenging to relate the local electrical and optoelectronic prop-

erties of all extended structural defects to the performance of Cu(In,Ga)Se_2 thin-film solar cells. For highly symmetrical, coherent twin boundaries, the present work is able to show that their impact on the solar-cell efficiency is negligible. However, for the other types of extended structural defects, it is still not clear whether and how the electronic band diagram changes across them. While stacking faults and dislocations exhibit distinct atomic structures, which imply specific electrical properties, at different random GBs, also different structural, compositional, electrical and optoelectronic properties were measured. This means, it is not possible to identify a specific structural GB model Cu(In,Ga)Se_2 thin films and relate this directly to the device performance of corresponding solar cells. Thus, direct relationships between the microscopic structure and macroscopic properties can not be obtained for this quite complex material system. Nevertheless, by application of correlative microscopy on extended structural defects, it was possible to get access to structure-property relationships on the microscopic level, highlighting the electrical and optoelectronic properties of extended structural defects in Cu(In,Ga)Se_2 thin films.

Chapter 6

General conclusions and outlook

In the scope of the present work, it has been shown at the example of $Cu(In,Ga)Se_2$ solar cells that extended structural defects influence the microscopic electrical and optoelectronic properties of functional thin films, which may impact substantially the performance of corresponding semiconductor devices. It is essential to analyze the properties of these defects on various spatial extensions ranging from several hundreds of micrometers down to subnanometer scales. It was also shown how this analysis can be performed by correlative microscopy, employing various electron microscopy and scanning probe techniques all on the identical region of interest of a specimen, in order to maximize the information output. In view of small average grain sizes in polycrystalline, active layers, which are often at the submicrometer level, available characterization techniques need to be adapted to reach appropriately high spatial resolutions.

In comparison with multicrystalline Si solar cells, for which enhanced recombination at extended structural defects can be related directly to a deterioration of the photovoltaic performance, this direct structure-property relationship, including both, photocurrent and photovoltage, has turned out to be challenging for $Cu(In,Ga)Se_2$ solar cells. Only in case of the short-circuit current density j_{sc}, a correlation with microscopic properties was highlighted. On the other hand, nonradiative recombination at extended structural defects has not yet been identified as main reason for the limited open-circuit voltage V_{oc}. Therefore, the present work focuses on "microscopic" rather than "macroscopic" stucture-property relationships, discussing the structral, compositional, electrical, and optoelectrical properties of structural defects in $Cu(In,Ga)Se_2$ thin films in detail.

While (highly) symmetric, structural defects such as stacking faults, twins, and in some respect also (partial) dislocations exhibit clearly defined, crystallographic constellations, the case of (random) GBs is much more complicated. The various measurements performed at these low-symmetric, structural defects revealed different signal changes for different GBs, even within the same identical $Cu(In,Ga)Se_2$ thin film. Such a situation makes it very difficult to determine a representative energy-band diagram for a (random) GB in $Cu(In,Ga)Se_2$. Even if possible energy-band diagrams can be provided for highly symmetrical twins (and in near future probably also for stacking faults and dislocations), the number of possible point defects present at these struc-

tural defects is large, including also those based on the impurities mainly from the used substrates. And the relative frequencies of these point defects is always different, leading probably to different signal changes for the various techniques (particularly at GBs). Thus, an entirely consistent device model describing the influence of the various extended structural defects with different changes in composition and correspondingly different electronic properties on the solar-cell performance can not be expected.

The complex material system of $Cu(In,Ga)Se_2$ solar cells also demonstrates that even in order to correlate the microstructural and compositional with electrical and optoelectronic properties of extended structural defects on the micro- or nanoscale, extensive studies applying various techniques are mandatory, if possible on the same identical specimen positions. Moreover, it is always required that a sufficient number of extended structural defects are analyzed, in order to provide good statistics of the result.

Such a complex scenario is also found when dealing with other state-of-the-art semiconductor devices, such as solar cells based on CdTe, $Cu_2ZnSn(S,Se)_4$ (kesterites), or $CH_3NH_3PbI_{3-x}Cl_x$ (perovskites). For all these materials, highest power-conversion efficiencies have been achieved when using polycrystalline, not monocrystalline, thin films or bulk materials. This means, extended structural defects are an inherent part of the devices, and for their research and development, it is indispensible to study the microstructural, compositional, electrical, and optoelectronic properties of these defects on the microscopic level. This systematic work is often neglected, therefore, for many material systems, only poor knowledge has been gathered so far. Since for the complex material systems mentioned above also complex scenarios at extended structural defects can be expected, similar to what has been found for $Cu(In,Ga)Se_2$, it is recommended to restrict, as first approach, also to the analysis of "microscopic" structure-property relationships in these cases.

While up to now, we have considered only microstructures in completed devices, the ultimate goal would be to find means in order to control the microstructure during the growth process of a functional thin film, and to relate changes in microstructure to influences on the device performance. Using again the example of $Cu(In,Ga)Se_2$ solar cells, growth processes can be monitored by means of energy-dispersive X-ray diffraction (EDXRD) and fluorescence analysis (EDXRF) when connecting growth chambers to a synchrotron source, allowing the polychromatic X-ray beam interacting with the growing layer [255–257]. From these analyses, structural and compositional information during the growth of thin films can be recorded, and the distribution of chemical phases can be determined as a function of the growth-process duration. In order to study the layers at various stages of the growth in-depth, the processes can be broken off, and the layers can be studied by various microscopy techniques. Especially those based on electron microscopy are useful for this purpose.

Once the development of extended structural defects has been highlighted by the various experimental techniques, a solid basis is provided for corresponding simulations, which may be conducted by molecular dynamics (atomistic approach) and by phase-field simulations (continuum approach). Thus, growth processes may be simulated, given that a specific growth recipe and corresponding process parameters (e.g., elemental partial pressures, substrate temperature) are applied. This step is essential for a feedback loop leading back to the growth processing, with the goal of predicting the formation of a specific microstructure for a given set of growth parameters.

For example, this described strategy for controlled microstructure is currently being applied within the Helmholtz Virtual Institute "Microstructure Control for Thin Film Solar Cells" [258], which is coordinated by the author of the present work and

dealing with the development of thin-film solar cells based on polycrystalline Si and $Cu(In,Ga)Se_2$ solar cells. In a similar way, the described approach may be applied also to other semiconductor devices with polycrystalline functional layers. It should be noted eventually that correlative microscopy provides the means to direct "microscopic" structure-property relationships in semiconductor devices on multiple scales, playing a major role in the corresponding research and development.

References

[1] Holt, D. B. and Joy, D. C. (1989) *SEM microcharacterization of semiconductors*. Academic Press.

[2] Yacobi, B. and Holt, D. (1990) *Cathodoluminescence microscopy of inorganic solids*. Plenum Press, New York.

[3] Holt, D. and Yacobi, B. (2007) *Extended defects in semiconductors*. Cambridge Univ Press.

[4] Donolato, C. A. (1983) Theory of beam induced characterization of grain boundaries in polycrystalline solar cells. *J. Appl. Phys.*, **54**, 1314–1322.

[5] Donolato, C. and Bell, R. (1983) Characterization of grain boundaries in polycrystalline solar cells using a computerized electron beam induced current system. *Rev. Sci. Instrum.*, **54**, 1005–1009.

[6] Donolato, C., Niponi, R., Govoni, D., Egeni, G., Rudello, V., and Rossi, P. (1996) Images of grain boundaries in polycrystalline silicon solar cells by electron and ion beam induced charge collection. *Mater. Sci. Eng. B*, **42**, 306–310.

[7] Chen, J., Sekiguchi, T., Xie, R., Ahmet, P., Chikyo, T., Yang, D., Ito, S., and Yin, F. (2005) Electron-beam-induced current study of small-angle grain boundaries in multicrystalline silicon. *Scripta Materialia*, **52**, 1211–1215.

[8] Chen, J., Yuan, X., and Sekiguchi, T. (2008) Advanced semiconductor diagnosis by multidimensional electron-beam-induced current technique. *Scanning*, **30**, 347–353.

[9] Chen, J., Chen, B., Sekiguchi, T., Fukuzawa, M., and Yamada, M. (2008) Correlation between residual strain and electrically active grain boundaries in multicrystalline silicon. *Applied Physics Letters*, **93**, 112105.

[10] Lee, W., Chen, J., Chen, B., Chang, J., and Sekiguchi, T. (2009) Cathodoluminescence study of dislocation-related luminescence from small-angle grain boundaries in multicrystalline silicon. *Applied Physics Letters*, **94**, 112103.

[11] Repins, I., Contreras, M. A., Egaas, B., DeHart, C., Scharf, J., Perkins, C. L., To, B., and Noufi, R. (2008) 19.9%-efficient ZnO/CdS/$CuInGaSe_2$ solar cell with 81.2% fill factor. *Prog. Photovolt: Res. Appl.*, **16**, 235–239.

[12] Chirilă, A., Reinhard, P., Pianezzi, F., Bloesch, P., Uhl, A. R., Fella, C., Kranz, L., Keller, D., Gretener, C., Hagendorfer, H., Jaeger, D., Erni, R., Nishiwaki, S., Buecheler, S., and Tiwari, A. N. (2013) Potassium-induced surface modification

of Cu(In,Ga)Se_2 thin films for high-efficiency solar cells. *Nature Materials*, **12**, 1107–1111.

[13] Jackson, P., Hariskos, D., Wuerz, R., Wischmann, W., and Powalla, M. (2014) Compositional investigation of potassium doped Cu(In,Ga)Se_2 solar cells with efficiencies up to 20.8%. *phys. stat. sol. (RRL)*, doi: 10.1002/pssr.201409040.

[14] http://www.solar-frontier.com/eng/news/2014/C031367.html. Accessed on April 2, 2014.

[15] Kirchartz, T. and Rau, U. (2011) Introduction to thin-film photovoltaics. In *Advanced characterization techniques for thin-film solar cells,* Abou-Ras, D., Kirchartz, T., and Rau, U. (eds.), chap. 1, pp. 3–32, Wiley VCH, Weinheim.

[16] Shockley, W. (1949) The theory of p-n junctions in semiconductors and p-n junction transistors. *Bell System Techn. J.*, **28**, 435–489.

[17] Planck, M. (1906) *Vorlesungen über die Theorie der Wärmestrahlung*. Verlag von Johann Ambrosius Barth, Leipzig.

[18] Ruppel, W. and Würfel, P. (1980) Upper limit for the conversion of solar energy. *IEEE Transactions on Electron Devices*, **27**, 877–882.

[19] Rau, U. (2007) Reciprocity relation between photovoltaic quantum efficiency and electroluminescent emission of solar cells. *Phys. Rev. B*, **76**, 085303–1–8.

[20] Shockley, W. and Queisser, H. J. (1961) Detailed Balance Limit of Efficiency of p-n Junction Solar Cells. *J. Appl. Phys.*, **32**, 510–519.

[21] Kirchartz, T. (2009) *Generalized detailed balance theory of solar cells*. Ph.D. thesis, RWTH Aachen, http://darwin.bth.rwth-aachen.de/opus3/volltexte/2009/2700/ (accessed on May 12, 2013).

[22] http://rredc.nrel.gov/solar/spectra/am1.5/ (accessed on May 12, 2013).

[23] Rau, U. and Werner, J. H. (2004) Radiative efficiency limits of solar cells with lateral band-gap fluctuations. *Appl. Phys. Lett.*, **84**, 3735–3737.

[24] Meitner, L. (1922) Über die γ-Strahl-Spektra und ihren Zusammenhang mit der β-Strahlung. *Z. Phys.*, **11**, 35–54.

[25] Auger, P. (1925) Sur l'effet photoélectrique composé. *J. Phys. Radium*, **6**, 205–208.

[26] Shockley, W. and Read, W. T. (1952) Statistics of the recombinations of holes and electrons. *Phys. Rev.*, **87**, 835–842.

[27] Hall, R. N. (1952) Electron-Hole Recombination in Germanium. *Phys. Rev.*, **87**, 387–387.

[28] Pankove, J. (1971) *Optical processes in semiconductors*. Dover Publications, New York.

[29] Siebentritt, S. (2011) What limits the efficiency of chalcopyrite solar cells? *Sol. En. Mater. Sol. Cells*, **95**, 1471–1476.

[30] Donolato, C. (1998) Modeling the effect of dislocations on the minority carrier diffusion length of a semiconductor. *J. Appl. Phys.*, **84**, 2656–2664.

[31] Donolato, C. (1998) Analysis of Minority Carrier Diffusion in the Presence of a Dislocation Array: Effective Diffusion Length, Luminescence Efficiency and Dark Current. *Solid State Comm.*, **63-64**, 45–52.

[32] Kieliba, T., Riepe, S., and Warta, W. (2006) Effect of dislocations on open circuit voltage in crystalline silicon solar cells. *J. Appl. Phys.*, **100**, 093708.

[33] Nakamura, S. (1998) The Roles of Structural Imperfections in InGaN-Based Blue Light-Emitting Diodes and Laser Diodes. *Science*, **281**, 956–961.

[34] Stringfellow, G., Lindquist, P., Cass, T. R., and Burmeister, R. A. (1974) Dislocations in vapor phase epitaxial GaP. *J. Electron. Mater.*, **3**, 497–515.

[35] Gloeckler, M., Sites, J. R., and Metzger, W. K. (2005) Grain-boundary recombination in Cu(In,Ga)Se_2 solar cells. *J. Appl. Phys.*, **98**, 113704–1–10.

[36] Metzger, W. K. and Gloeckler, M. (2005) The impact of charged grain boundaries on thin-film solar cells and characterization. *J. Appl. Phys.*, **98**, 063701.

[37] Taretto, K., Rau, U., and Werner, J. (2005) Numerical simulation of grain boundary effects in Cu(In,Ga)Se_2 thin-film solar cells. *Thin Solid Films*, **480-481**, 8–12.

[38] Taretto, K. and Rau, U. (2008) Numerical simulation of carrier collection and recombination at grain boundaries in Cu(In,Ga)Se_2 solar cells. *J. Appl. Phys.*, **103**, 094523–1–11.

[39] Balluffi, R., Allen, S., and Carter, W. (2005) *Kinetics of Materials*. John Wiley & Sons, Inc.

[40] Mishin, Y. and Herzig, C. (1999) Grain boundary diffusion: recent progress and future research. *Mater. Sci. Eng. A*, **260**, 55 – 71.

[41] You, J. and Johnson, H. (2009) *Effect of Dislocations on Electrical and Optical Properties in GaAs and GaN*, vol. 61 of *Solid State Physics*, chap. 3, pp. 143 – 261. Academic Press.

[42] Bollmann, W. (1970) *Crystal defects and crystalline interfaces*. Springer, Berlin.

[43] Alexander, H. (1979) Models of the dislocation structure. *Journal de Physique*, **40**, 1–6.

[44] Li, C., Poplawsky, J., Wu, Y., Lupini, A. R., Mouti, A., Leonard, D. N., Paudel, N., Jones, K., Yin, W., Al-Jassim, M., Yan, Y., and Pennycook, S. J. (2013) From atomic structure to photovoltaic properties in CdTe solar cells. *Ultramicroscopy*, **134**, 113 – 125.

[45] Jagodzinski, H. (1949) Eindimensionale Fehlordnung in Kristallen und ihr Binfluss auf die Röntgeninterferenzen. I. Berechnung des Fehlordnungsgrades aus den Röntgenintensitäten. *Acta Cryst.*, **2**, 201–207.

[46] Billig, E. and Ridout, M. S. (1954) Transmission of Electrons and Holes Across a Twin Boundary in Germanium. *Nature*, **173**, 496–497.

[47] Queisser, H. J. (1963) Properties of Twin Boundaries in Silicon. *J. Electrochem. Soc.*, **110**, 52–56.

[48] Wang, Z.-J., Tsurekawa, S., Ikeda, K., Sekiguchi, T., and Watanabe, T. (1999) Relationship between Electrical Activity and Grain Boundary Structural Configuration in Polycrystalline Silicon. *Interface Science*, **7**, 197–205.

[49] Sekiguchi, T., Shen, B., Watanabe, T., and Sumino, K. (1996) EBIC study on the electrical activity of stacking faults in silicon. *Mater. Sci. Eng. B*, **42**, 235 – 239.

[50] Maurice, J. (1991) Microstructure and electrical properties of grain boundaries in elemental semiconductors. In *Polycrystalline Semiconductors II,* Werner, J. and Strunk, H. (eds.), vol. 54 of *Springer Series in Physics*, pp. 166–177.

[51] Randle, V. (2001) The coincidence site lattice and the 'sigma enigma'. *Materials Characterization*, **47**, 411 – 416.

[52] Grimmer, H., Bollmann, W., and D.H. Warrington (1974) Coincidence-site lattices and complete pattern-shift lattices in cubic crystals. *Acta Cryst. A*, **30**, 197–207.

[53] Hornstra, J. (1958) Dislocations in the diamond lattice. *J. Phys. Chem. Solids*, **5**, 129–141.

[54] Balluffi, R. (ed.) (1980) *Grain-Boundary Structure and Kinetics, Papers presented at the 1979 ASM Materials Science Seminar, Milwaukee, Wisconsin, September 15-16, 1979*. American Society for Metals, Metals Park, Ohio.

[55] Leamy, H., Pike, G., and Seager, C. (eds.) (1982) *Grain boundaries in semiconductors*, vol. 5 of *MRS Proceedings*, North-Holland, New York.

[56] Möller, H. J., Strunk, H., and Werner, J. (eds.) (1989) *Polycrystalline Semiconductors*, vol. 35 of *Springer Proceedings in Physics*, Grain Boundaries and Interfaces, Proceedings of the International Symposium, Malente, Germany, August 29-September 2, 1988.

[57] Werner, J. and Strunk, H. (eds.) (1990) *Polycrystalline Semiconductors II*, vol. 54 of *Springer Proceedings in Physics*, Proceedings of the Second International Conference, Schwäbisch Hall, Germany, July 30-August 3, 1990.

[58] Sutton, A. P. and Balluffi, R. W. (1995) *Interfaces in Crystalline Materials*. Oxford University Press.

[59] Seto, J. Y. W. (1975) The electrical properties of polycrystalline silicon films. *J. Appl. Phys.*, **46**, 5247–5254.

[60] Balluffi, R. (2012) *Introduction to Elasticity Theory for Crystal Defects*. Cambridge University Press, New York.

[61] Steeds, J. (1973) *Anisotropic elasticity theory of dislocations*. Clarendon Press, Oxford.

[62] Krill, C., Haberkorn, R., and Birringer, R. (2000) *Handbook of Nanostructured Materials and nanotechnonano, Volume 2: Spectroscopy and Theory*, chap. 3, in: H.S. Nalwa (Ed.), *Specification of microstructure and characterization by scattering techniques*, pp. 155–211. Academic Press.

[63] Williamson, G. and Hall, W. (1953) X-ray line broadening from filed aluminium and wolfram. *Acta Metall.*, **1**, 22 – 31.

[64] Hytch, M., Snoeck, E., and Kilaas, R. (1998) Quantitative measurement of displacement and strain fields from HREM micrographs. *Ultramicroscopy*, **74**, 131–146.

[65] Genzel, C. (2005) X-ray residual stress analysis in thin films under grazing incidence: basic aspects and applications. *Mater. Sci. Technol.*, **21**, 10–18.

[66] Wilkinson, A. J., Meaden, G., and Dingley, D. J. (2006) High resolution mapping of strains and rotations using electron backscatter diffraction. *Mater. Sci. Technol.*, **22**, 1271–1278.

[67] Hytch, M., Houdellier, F., Hue, F., and Snoeck, E. (2008) Nanoscale holographic interferometry for strain measurements in electronic devices. *Nature*, **453**, 1086–U5.

[68] Abou-Ras, D., Kirchartz, T., and Rau, U. (eds.) (2011) *Advanced Characterization Techniques for Thin-Film Solar Cells*. WILEY-VCH Verlag, Weinheim.

[69] Ayache, J., Beaunier, L., Boumendil, J., Ehret, G., and Laub, D. (2010) *Sample Preparation Handbook for Transmission Electron Microscopy*. Springer.

[70] Abou-Ras, D., Nichterwitz, M., Romero, M. J., and Schmidt, S. S. (2011) *Electron microscopy on thin films for solar cells*, chap. 12, in: D. Abou-Ras, T. Kirchartz, and U. Rau (Ed.), *Advanced Characterization Techniques for Thin-Film Solar Cells*, pp. 299–346. Wiley VCH, Weinheim.

[71] Giannuzzi, L. and Stevie, F. (eds.) (2005) *Introduction to Focused Ion Beams: Instrumentation, Theory, Techniques and Practice*. Springer, Berlin.

[72] Mayer, J., Giannuzzi, L., Kamino, T., and J., M. (2007) TEM sample preparation and FIB-induced damage. *MRS Bulletin*, **32**, 400–407.

[73] Schaffer, M., Schaffer, B., and Ramasse, Q. (2012) Sample preparation for atomic-resolution STEM at low voltages by FIB. *Ultramicroscopy*, **114**, 62–71.

[74] Lechner, L., Biskupek, J., and Kaiser, U. (2012) Improved Focused Ion Beam Target Preparation of (S)TEM Specimen: A Method for Obtaining Ultrathin Lamellae. *Microsc. Microanal.*, **18**, 379–384.

[75] Shimizu, K. and Mitani, T. (2010) *New Horizons of Applied Scanning Electron Microscopy*, vol. 45 of *Springer Series in Surface Science*. Springer, Berlin.

[76] Fuertes Marrón, D., Meeder, A., Sadewasser, S., Würz, R., Kaufmann, C. A., Glatzel, T., Schedel-Niedrig, T., and Lux-Steiner, M. C. (2005) Lift-off process and rear-side characterization of $CuGaSe_2$ chalcopyrite thin films and solar cells. *J. Appl. Phys.*, **97**, 094915–1–7.

[77] Kavalakkatt, J., Abou-Ras, D., Haarstrich, J., Ronning, C., Nichterwitz, M., Caballero, R., Rissom, T., Unold, T., Scheer, R., and Schock, H. W. (2014) Electron-beam-induced current at absorber back surfaces of Cu(In,Ga)Se_2 thin-film solar cells. *J. Appl. Phys.*, **115**, 014504–1–10.

[78] Kniese, R., Powalla, M., and Rau, U. (2007) Characterization of the CdS/Cu(In,Ga)Se_2 interface by electron beam induced currents. *Thin Solid Films*, **515**, 6163–6167.

[79] Fossum, J. and Burgess, E. (1978) Silicon solar cell designs based on physical behaviour in concentrated sunlight. *Solid State Electronics*, **21**, 729–737.

[80] Schmid, D., Jäger-Waldau, G., and Schock, H. (1991) Diffusion length measurement and modeling of $CuInSe_2$-(Zn,Cd)S solar cells. In *Proceedings of the 10th European Photovoltaic Solar Energy Conference, Lisbon, Portugal, April 8-12, 1991,* Luque, A., Sala, G., Palz, W., dos Santos, G., and Helm, P. (eds.), pp. 935–938, Kluwer Academic, Dordrecht.

[81] Cavalcoli, D. and Cavallini, A. (1994) Evaluation of diffusion length at different excess carrier concentrations. *Mat. Sci. Engin. B*, **24**, 98–100.

[82] Galloway, S., Edwards, P., and Durose, K. (1999) Characterization of thin film CdS/CdTe solar cells using electron and optical beam induced current. *Solar En. Mat. Sol. Cells*, **57**, 61–74.

[83] Röll, K. (1980) The temperature distribution in a thin metal film exposed to an electron beam. *Appl. Surf. Sci.*, **5**, 388–397.

[84] Matson, R.J., Noufi, R., Ahrenkiel, R.K., Powell, R.C., and Cahen, D. (1986) EBIC investigations of junction activity and the role of oxygen in CdS/$CuInSe_2$ devices. *Solar Cells*, **16**, 495–519.

[85] Hakimzadeh, R. and Bailey, S. (1993) Minority carrier diffusion length and edge surface recombination velocity in InP. *J. Appl. Phys.*, **74**, 1118–1123.

[86] Bhattacharyya, S., Koch, C. T., and Rühle, M. (2006) Projected potential profiles across interfaces obtained by reconstructing the exit face wave function from through focal series. *Ultramicroscopy*, **106**, 525–538.

[87] Koch, C. (2008) A flux-preserving non-linear inline holography reconstruction algorithm for partially coherent electrons. *Ultramicroscopy*, **108**, 141–150.

[88] Dietrich, J. (2013) *Mikrostrukturanalyse von Cu(In,Ga)Se_2 Dünnschichtsolarzellen mittels Transmissionslektronenmikroskopie*. Ph.D. thesis, TU Berlin.

[89] Reimer, L. (1997) *Transmission Electron Microscopy*. Springer-Verlag, 4th edn.

[90] Egerton, R. F. (1996) *Electron Energy-Loss Spectroscopy in the Electron Microscope*. Plenum Press, New York.

[91] Williams, D. B. and Carter, C. B. (2009) *Transmission Electron Microscopy*. Springer.

[92] Ibers, J. A. (1958) Atomic scattering amplitudes for electrons. *Acta Cryst.*, **11**, 178–183.

[93] Abou-Ras, D., Schmidt, S., Caballero, R., Unold, T., Schock, H.-W., Koch, C., Schaffer, B., Schaffer, M., Choi, P., and Cojocaru-Mirédin, O. (2012) Confined and chemically flexible grain boundaries in polycrystalline semiconductors. *Adv. En. Mater.*, **2**, 992–998.

[94] Klie, R. F., Beleggia, M., Zhu, Y., Buban, J. P., and Browning, N. D. (2003) Atomic-scale model of the grain boundary potential in perovskite oxides. *Phys. Rev. B*, **68**, 214101.

[95] Varela, M., Lupini, A., Benthem, K. v., Borisevich, A., Chisholm, M., Shibata, N., Abe, E., and Pennycook, S. (2005) Materials characterization in the aberration-corrected scanning transmission electron microscope. *Annu. Rev. Mater. Res.*, **35**, 539–569.

[96] Prabhumirashi, P., Dravid, V. P., Lupini, A. R., Chisholm, M. F., and Pennycook, S. J. (2005) Atomic-scale manipulation of potential barriers at $SrTiO_3$ grain boundaries. *Applied Physics Letters*, **87**, 121917–1–4.

[97] Klie, R. F., Zhao, Y., Yang, G., and Zhu, Y. (2008) High-resolution Z-contrast imaging and {EELS} study of functional oxide materials. *Micron*, **39**, 723 – 733.

[98] Rühle, M. and Sass, S. L. (1984) The detection of the change in mean inner potential at dislocations in grain-boundaries in NiO. *Phil. Mag. A*, **49**, 759–782.

[99] Weiss, J., de Ruijter, W., Gajdardziska-Josifovska, M., McCartney, M., and Smith, D. J. (1993) Applications of electron holography to the study of interfaces. *Ultramicroscopy*, **50**, 301–311.

[100] Schofield, M. A., Beleggia, M., Zhu, Y., Guth, K., and Jooss, C. (2004) Direct Evidence for Negative Grain Boundary Potential in Ca-Doped and Undoped $YBa_2Cu_3O_{7-x}$. *Phys. Rev. Lett.*, **92**, 195502–1–4.

[101] Houben, L., Luysberg, M., and Brammer, T. (2004) Illumination effects in holographic imaging of the electrostatic potential of defects and pn junctions in transmission electron microscopy. *Phys. Rev. B*, **70**, 165313.

[102] Koch, C. T. (2009) Using dynamically scattered electrons for three-dimensional potential reconstruction. *Acta Cryst. A*, **65**, 364–370.

[103] von Alfthan, S., Benedek, N. A., Chen, L., Chua, A., Cockayne, D., Dudeck, K. J., Elsasser, C., Finnis, M. W., Koch, C. T., Rahmati, B., Ruhle, M., Shih, S. J., and Sutton, A. P. (2010) The Structure of Grain Boundaries in Strontium Titanate: Theory, Simulation, and Electron Microscopy. *Annu. Rev. Mater. Res.*, **40**, 557–599.

[104] Spence, J. C. H., Kolar, H. R., Hembree, G., Humphreys, C. J., Barnard, J., Datta, R., Koch, C., Ross, F. M., and Justo, J. F. (2006) Imaging dislocation cores: the way forward. *Philos. Mag.*, **86**, 4781–4796.

[105] Jackson, P., Hariskos, D., Lotter, E., Paetel, S., Wuerz, R., Menner, R., Wischmann, W., and Powalla, M. (2011) New world record efficiency for Cu(In,Ga)Se_2 thin-film solar cells beyond 20%. *Prog. Photovolt: Res. Appl.*, **19**, 894–897.

[106] Chirilă, A., Buecheler, S., Pianezzi, F., Bloesch, P., Gretener, C., Uhl, A., Fella, C., Kranz, L., Perrenoud, J., Seyrling, S., Verma, R., Nishiwaki, S., Romanyuk, Y., Bilger, G., and Tiwari, A. (2011) Highly efficient Cu(In,Ga)Se_2 solar cells grown on flexible polymer films. *Nat. Mater.*, **10**, 857–861.

[107] Haarstrich, J., Metzner, H., Oertel, M., Ronning, C., Rissom, T., Kaufmann, C., Unold, T., Schock, H., Windeln, J., Mannstadt, W., and Rudigier-Voigt, E. (2011) Increased homogeneity and open-circuit voltage of Cu(In,Ga)Se_2 solar cells due to higher deposition temperature. *Sol. En. Mater. Sol. Cells*, **95**, 1028–1030.

[108] Contreras, M. A., Tuttle, J., Gabor, A., Tennant, A., Ramanathan, K., Asher, S., Franz, A., Keane, J., Wang, L., Scofield, J., and Noufi, R. (1994) High efficiency Cu(In,Ga)Se_2-based solar cells: Processing of novel absorber structures. In *Conference Record of the 1994 IEEE 1st World Conference on Photovoltaic Energy Conversion, Waikoloa, HI, U.S.A., December 5-9, 1994*, pp. 68–75, IEEE, Piscataway, NJ.

[109] Powalla, M., Voorwinden, G., Hariskos, D., Jackson, P., and Kniese, R. (2009) Highly efficient CIS solar cells and modules made by the co-evaporation process. *Thin Solid Films*, **517**, 2111–2114.

[110] Kaufmann, C. A., Caballero, R., Unold, T., Hesse, R., Klenk, R., Schorr, S., Nichterwitz, M., and Schock, H.-W. (2009) Depth profiling of Cu(In,Ga)Se_2 thin films grown at low temperatures. *Sol. Energy Mater. Sol. Cells*, **93**, 859–863.

[111] Shafarman, W. N., Klenk, R., and McCandless, B. E. (1996) Device and material characterization of Cu(InGa)Se_2 solar cells with increasing band gap. *J. Appl. Phys.*, **79**, 7324–7328.

[112] Herberholz, R., Nadenau, V., Rühle, U., Köble, C., Schock, H., and Dimmler, B. (1997) Prospects of wide-gap chalcopyrites for thin film photovoltaic modules. *Sol. En. Mat. Sol. Cells*, **49**, 227–237.

[113] Herberholz, R., Rau, U., Schock, H., Haalboom, T., Gödecke, T., Ernst, F., Beilharz, C., Benz, K., and Cahen, D. (1999) Phase segregation, Cu migration and junction formation in Cu(In,Ga)Se_2. *Eur. Phys. J. Appl. Phys.*, **6**, 131–139.

[114] Vegard, L. (1921) Die Konstitution der Mischkristalle und die Raumfüllung der Atome. *Z. Phys.*, **5**, 17–27.

[115] Suri, D. K., Nagpal, K. C., and Chadha, G. K. (1989) X-ray study of $CuGa_xIn_{1-x}Se_2$ solid solutions. *J. Appl. Crystallogr.*, **22**, 578–583.

[116] Alonso, M. I., Wakita, K., Pascual, J., Garriga, M., and Yamamoto, N. (2001) Optical functions and electronic structure of $CuInSe_2$, $CuGaSe_2$, $CuInS_2$, and $CuGaS_2$. *Phys. Rev. B*, **63**, 075203–.

[117] Wei, S.-H. and Zunger, A. (1995) Band offsets and optical bowings of chalcopyrites and Zn-based II-VI alloys. *J. Appl. Phys.*, **78**, 3846–3856.

[118] Jackson, P., Würz, R., Rau, U., Mattheis, J., Kurth, M., Schlötzer, T., Bilger, G., and Werner, J. H. (2007) High quality baseline for high efficiency, $Cu(In_{1-x},Ga_x)Se_2$ solar cells. *Prog. Photovolt.: Res. Appl.*, **15**, 507–519.

[119] Abou-Ras, D., Caballero, R., Kaufmann, C. A., Nichterwitz, M., Sakurai, K., Schorr, S., Unold, T., and Schock, H. W. (2008) Impact of the Ga concentration on the microstructure of $CuIn_{1-x}Ga_xSe_2$. *phys. stat. sol. (RRL)*, **2**, 135–137.

[120] Cahen, D. and Noufi, R. (1992) Free energies and enthalpies of possible gas phase and surface reactions for preparation of $CuInSe_2$. *J. Phys. Chem. Solids*, **53**, 991–1005.

[121] Abou-Ras, D., Gibmeier, J., Nolze, G., Gholinia, A., and Konijnenberg, P. (2008) On the capability of revealing the pseudosymmetry of the chalcopyrite-type crystal structure. *Crystal Research and Technology*, **43**, 234–239.

[122] Hedström, J., Ohlsen, H., Bodegård, M., Kylner, A., Stolt, L., Hariskos, D., Ruckh, M., and Schock, H. W. (1993) ZnO/CdS/Cu(In,Ga)Se_2 thin film solar cells with improved performance. In *Conference Record of the 23rd IEEE Photovoltaic Specialists Conference, Louisville, Kentucky, May 10-14, 1993*, pp. 364–371, IEEE, New York, NY.

[123] Rudmann, D. (2004) *Effects of sodium on growth and properties of Cu(In,Ga)Se_2 thin films and solar cells*. Ph.D. thesis, ETH Zürich.

[124] Hariskos, D., Menner, R., Jackson, P., Paetel, S., Witte, W., Wischmann, W., Powalla, M., Bürkert, L., Kolb, T., Oertel, M., Dimmler, B., and Fuchs, B. (2012) New reaction kinetics for a high-rate chemical bath deposition of the Zn(S,O) buffer layer for Cu(In,Ga)Se_2-based solar cells. *Prog. Photovolt.: Res. Appl.*, **20**, 534–542.

[125] http://www.zsw-bw.de/en/support/news/news-detail/zsw-stellt-weltrekord-solarzelle-her.html, accessed on October 24, 2013.

[126] Malmström, J., Lundberg, O., and Stolt, L. (2003) Potential for light trapping in Cu(In,Ga)Se_2 solar cells. In *Proceedings of the 3rd World Conference on Photovoltaic Energy Conversion, Osaka, Japan, May 11-18, 2003,* Kurokawa, K., Kazmerski, L.L., McNelis, B., Yamaguchi, M., Wronski, C., and Sinke, W.C. (ed.), pp. 344–347.

[127] Burgelman, M., Nollet, P., and Degrave, S. (2000) Modelling polycrystalline semiconductor solar cells. *Thin Solid Films*, **361-362**, 527–532.

[128] Scheer, R. and Schock, H.-W. (2011) *Chalcogenide Photovoltaics: Physics, Technologies, and Thin Film Devices*. Wiley-VCH.

[129] Orgis, T., Maiberg, M., and Scheer, R. (2013) Influence of band gradients on Cu(In,Ga)Se_2 solar cell diode factors. *J. Appl. Phys.*, **114**, 214506–1–8.

[130] Gütay, L., Lienau, C., and Bauer, G. H. (2010) Subgrain size inhomogeneities in the luminescence spectra of thin film chalcopyrites. *Appl. Phys. Lett.*, **97**, 052110.

[131] Contreras, M. A., Repins, I., Metzger, W. K., Romero, M., and Abou-Ras, D. (2009) Se activity and its effect on Cu(In,Ga)Se_2 photovoltaic thin films. *Phys. Stat. Sol. A*, **206**, 1042–1048, 16th International Conference on Ternary and Multinary Compounds, Berlin, Germany, September 15-19, 2008.

[132] Müller, M., Abou-Ras, D., Rissom, T., Bertram, F., and Christen, J. (2014) Symmetry dependent optoelectronic properties of grain boundaries in polycrystalline Cu(In,Ga)Se_2 thin films. *J. Appl. Phys.*, **115**, 023514–1–6.

[133] Jiang, C.-S., Noufi, R., Ramanathan, K., AbuShama, J. A., Moutinho, H. R., and Al-Jassim, M. M. (2004) Does the local built-in potential on grain boundaries of Cu(In,Ga)Se_2 thin films benefit photovoltaic performance of the device? *Appl. Phys. Lett.*, **85**, 2625–2627.

[134] Jiang, C.-S., Noufi, R., AbuShama, J. A., Ramanathan, K., Moutinho, H. R., Pankow, J., and Al-Jassim, M. M. (2004) Local built-in potential on grain boundary of Cu(In,Ga)Se_2 thin films. *Appl. Phys. Lett.*, **84**, 3477–3479.

[135] Fuertes Marrón, D., Sadewasser, S., Meeder, A., Glatzel, T., and Lux-Steiner, M. C. (2005) Electrical activity at grain boundaries of Cu(In,Ga)Se_2 thin films. *Phys. Rev. B*, **71**, 033306–1–4.

[136] Sadewasser, S. (2007) Microscopic characterization of individual grain boundaries in Cu-III-VI_2 chalcopyrites. *Thin Solid Films*, **515**, 6136–6141.

[137] Yan, Y., Jones, K., Jiang, C., Wu, X., Noufi, R., and Al-Jassim, M. (2007) Understanding the defect physics in polycrystalline photovoltaic materials. *Physica B: Cond. Matter*, **401-402**, 25–32.

[138] Sadewasser, S., Abou-Ras, D., Azulay, D., Baier, R., Balberg, I., Cahen, D., Cohen, S., Gartsman, K., Ganesan, K., Kavalakkatt, J., Li, W., Millo, O., Rissom, T., Rosenwaks, Y., Schock, H.-W., Schwarzman, A., and Unold, T. (2011) Nanometer-scale electronic and microstructural properties of grain boundaries in Cu(In,Ga)Se_2. *Thin Solid Films*, **519**, 7341–7346.

[139] Baier, R., Abou-Ras, D., Rissom, T., Lux-Steiner, M., and Sadewasser, S. (2011) Symmetry-dependence of electronic grain boundary properties in polycrystalline $CuInSe_2$ thin films. *Appl. Phys. Lett.*, **99**, 172102–1–3.

[140] Jiang, C.-S., Contreras, M. A., Repins, I., Moutinho, H. R., Yan, Y., Romero, M. J., Mansfield, L. M., Noufi, R., and Al-Jassim, M. M. (2012) How grain boundaries in Cu(In,Ga)Se_2 thin films are charged: Revisit. *Appl. Phys. Lett.*, **101**, 033903–1–4.

[141] Baier, R., Lehmann, J., Lehmann, S., Rissom, T., Kaufmann, C. A., Schwarzmann, A., Rosenwaks, Y., Lux-Steiner, M. C., and Sadewasser, S. (2012) Electronic properties of grain boundaries in Cu(In,Ga)Se_2 thin films with various Ga-contents. *Sol. En. Mater. Sol. Cells*, **103**, 86 – 92.

[142] Werner, J. H., Mattheis, J., and Rau, U. (2005) Efficiency limitations of polycrystalline thin film solar cells: case of Cu(In,Ga)Se_2. *Thin Solid Films*, **480-481**, 399 – 409.

[143] Zhang, Z., Tang, X., Kiowski, O., Hetterich, M., Lemmer, U., Powalla, M., and Holscher, H. (2012) Reevaluation of the beneficial effect of Cu(In,Ga)Se_2 grain boundaries using Kelvin probe force microscopy. *Appl. Phys. Lett.*, **100**, 203903–1–4.

[144] Cahen, D. (1987) Some thoughts on defect chemistry of ternaries. In *Proceedings of the 7th International Conference on Ternary and Multinary Compounds, Snowmass, CO, U.S.A., September 10-12, 1986,* Deb, S. and Zunger, A. (eds.), pp. 433–442, Materials Research Society, Pittsburgh, PA.

[145] Burgelman, M., Engelhardt, F., Guillemoles, J.F., Herberholz, R., Igalson, M., Klenk, R., Lampert, M., Meyer, T., Nadenau, V., Niemegeers, A., Parisi, J., Rau, U., Schock, H.W., Schmitt, M., Seifert, O., Walter, T., and Zott, S. (1997) Defects in Cu(In, Ga)Se_2 semiconductors and their role in the device performance of thin-film solar cells. *Prog. Photovolt.: Res. Appl.*, **5**, 121–130.

[146] Zunger, A., Zhang, S.B., and Wei, S.H. (1997) Revisiting the defect physics in $CuInSe_2$ and $CuGaSe_2$. In *Conference Record of the 26th IEEE Photovoltaic Specialists Conference, Anaheim, CA, USA, September 29-October 3, 1997*, pp. 313–318, IEEE, Piscataway, NJ.

[147] Rau, U. and Schock, H. W. (1999) Electronic properties of Cu(In,Ga)Se_2 heterojunction solar cells-recent achievements, current understanding, and future challenges. *Appl. Phys. A*, **69**, 131–147.

[148] Rockett, A. (2000) The Electronic effects of point defects in Cu(In_xGa_{1-x})Se_2. *Thin Solid Films*, **361-362**, 330–337.

[149] Siebentritt, S., Igalson, M., Persson, C., and Lany, S. (2010) The electronic structure of chalcopyrites–bands, point defects and grain boundaries. *Prog. Photovolt: Res. Appl.*, **18**, 390–410.

[150] Migliorato, P., Shay, J. L., Kasper, H. M., and Wagner, S. (1975) Analysis of the electrical and luminescent properties of $CuInSe_2$. *J. Appl. Phys.*, **46**, 1777–1782.

[151] Noufi, R., Axton, R., Herrington, C., and Deb, S. K. (1984) Electronic properties versus composition of thin films of $CuInSe_2$. *Appl. Phys. Lett.*, **45**, 668–670.

[152] Rau, U., Braunger, D., Herberholz, R., Schock, H. W., Guillemoles, J. F., Kronik, L., and Cahen, D. (1999) Oxygenation and air-annealing effects on the electronic properties of Cu(In,Ga)Se_2 films and devices. *J. Appl. Phys.*, **86**, 497–505.

[153] Kronik, L., Cahen, D., and Schock, H. W. (1998) Effects of Sodium on Polycrystalline Cu(In,Ga)Se_2 and Its Solar Cell Performance. *Adv. Mater.*, **10**, 31–36.

[154] Pasemann, M., Klimanek, P., and Oettel, H. (1974) Superdislocations in chalcopyrite structure. *Phys. Stat. Sol. A*, **22**, K1–K4.

[155] Monfort, Y., Vizot, J., and Deschanvres, A. (1975) Faults in chalcopyrite structures. *Phys. Stat. Sol. A*, **29**, 551–561.

[156] Murr, L. E. and Lerner, S. L. (1977) Transmission electron-microscopic study of defect structure in natural chalcopyrite ($CuFeS_2$). *J. Mater. Sci.*, **12**, 1349–1354.

[157] Murr, L. E. and Hiskey, J. B. (1981) Kinetic effects of particle-size and crystal dislocation density on the dichromate leaching of chalcopyrite. *Metall. Trans. B*, **12**, 255–267.

[158] Couderc, J. J. and Hennigmichaeli, C. (1986) Transmission electron microscopy of experimentally deformed chalcopyrite single crystals. *Phys. Chem. Minerals*, **13**, 393–402.

[159] Kiely, C., Pond, R., Kenshole, G., and Rockett, A. (1991) A TEM study of the crystallography and defect structures of single crystal and polycrystalline copper indium diselenide. *Phil. Mag. A*, **63**, 1249–1273.

[160] Hinks, J. and Donnely, S. (2011) Copper indium diselenide: crystallography and radition-induced dislocation loops. *Phil. Mag.*, **91**, 517–536.

[161] Dietrich, J., Abou-Ras, D., Schmidt, S. S., Rissom, T., Unold, T., Cojocaru-Mirédin, O., Niermann, T., Lehmann, M., Koch, C. T., and Boit, C. (2014) Origins of electrostatic potential wells at dislocations in polycrystalline Cu(In,Ga)Se_2 thin films. *J. Appl. Phys.*, **115**, 103507–1–12.

[162] Ray, I. and Cockayne, D. (1971) The Dissociation of Dislocations in Silicon. *Proc. R. Soc. Lond. A*, **325**, 543–554.

[163] Medvedeva, N. I., Shalaeva, E. V., Kuznetsov, M. V., and Yakushev, M. V. (2006) First-principles study of deformation behavior and structural defects in $CuInSe_2$ and Cu(In,Ga)Se_2. *Phys. Rev. B*, **73**, 035207–1–6.

[164] Dietrich, J., Abou-Ras, D., Rissom, T., Unold, T., and Schock, H.-W. (2012) Compositional Gradients in Cu(In,Ga)Se_2 Thin Films for Solar Cells and Their Effects on Structural Defects. *IEEE Journal of Photovoltaics*, **2**, 364–370.

[165] Steeds, J. W. (1966) Dislocation arrangement in copper single crystals as a function of strain. *Proc. R. Soc. London Series A*, **292**, 343–373.

[166] Balboul, M. R., Schock, H. W., Fayak, S. A., Abdel El-Aal, A., Werner, J. H., and Ramadan, A. A. (2008) Correlation of structure parameters of absorber layer with efficiency of Cu(In,Ga)Se_2 solar cell. *Appl. Phys. A*, **92**, 557–563.

[167] Müller, E., Gerthsen, D., Brückner, P., Scholz, F., Gruber, T., and Waag, A. (2006) Probing the electrostatic potential of charged dislocations in n-GaN and n-ZnO epilayers by transmission electron holography. *Phys. Rev. B*, **73**, 245316–1–9.

[168] http://elim.physik.uni-ulm.de?page_id=834, accessed on May 27, 2013.

[169] Schmidt, S., Abou-Ras, D., Sadewasser, S., Yin, W., Feng, C., and Yan, Y. (2012) Electrostatic Potentials at Cu(In,Ga)Se_2 Grain Boundaries: Experiment and Simulations. *Phys. Rev. Lett.*, **109**, 095506–1–5.

[170] Puech, K., Zott, S., Leo, K., Ruckh, M., and Schock, H.-W. (1996) Determination of minority carrier lifetimes in $CuInSe_2$ thin films. *Appl. Phys. Lett.*, **69**, 3375–3377.

[171] Heath, J., Cohen, J., and Shafarman, W. (2004) Bulk and metastable defects in $CuIn_{1-x}Ga_xSe_2$ thin films using drive-level capacitance profiling. *J. Appl. Phys.*, **95**, 1000–1010.

[172] Yakushev, M. V., Luckert, F., Faugeras, C., Karotki, A. V., Mudryi, A. V., and Martin, R. W. (2010) Excited states of the free excitons in $CuInSe_2$ single crystals. *Appl. Phys. Lett.*, **97**, 152110–1–3.

[173] Ophus, C. and Ewalds, T. (2012) Guidelines for quantitative reconstruction of complex exit waves in HRTEM. *Ultramicroscopy*, **113**, 88–95.

[174] Read, W. (1954) Theory of dislocations in germanium. *Philos. Mag.*, **45**, 775–796.

[175] Cadel, E., Barreau, N., Kessler, J., and Pareige, P. (2010) Atom probe study of sodium distribution in polycrystalline $Cu(In,Ga)Se_2$ thin film. *Acta Mater.*, **58**, 2634–2637.

[176] Schlesiger, R., Oberdorfer, C., Wurz, R., Greiwe, G., Stender, P., Artmeier, M., Pelka, P., Spaleck, F., and Schmitz, G. (2010) Design of a laser-assisted tomographic atom probe at Münster University. *Rev. Sci. Instrum.*, **81**, 043703–1–8.

[177] Cojocaru-Mirédin, O., Choi, P.-P., Abou-Ras, D., Schmidt, S., Caballero, R., and Raabe, D. (2011) Characterization of Grain Boundaries in $Cu(In,Ga)Se_2$ Films Using Atom-Probe Tomography. *IEEE Journal of Photovoltaics*, **1**, 207–212.

[178] Doyle, P. and Turner, P. (1968) Relativistic Hartree-Fock X-ray and electron scattering factors. *Acta Cryst. A*, **24**, 390–397.

[179] Rez, D., Rez, P., and Grant, I. (1994) Dirac–Fock calculations of X-ray scattering factors and contributions to the mean inner potential for electron scattering. *Acta Cryst. A*, **50**, 481–497.

[180] Peng, L.-M. (1998) Electron Scattering Factors of Ions and their Parameterization. *Acta Cryst. A*, **54**, 481–485.

[181] Persson, C. and Zunger, A. (2003) Anomalous Grain Boundary Physics in Polycrystalline $CuInSe_2$: The Existence of a Hole Barrier. *Phys. Rev. Lett.*, **91**, 266401–1–4.

[182] Persson, C. and Zunger, A. (2005) Compositionally induced valence-band offset at the grain boundary of polycrystalline chalcopyrites creates a hole barrier. *Appl. Phys. Lett.*, **87**, 211904–1–3.

[183] Wei, S., Zhang, S., and Zunger, A. (1999) Effects of Na on the electrical and structural properties of $CuInSe_2$. *J. Appl. Phys.*, **85**, 7214–7218.

[184] Klein, A., Loher, T., Pettenkofer, C., and Jaegermann, W. (1996) Chemical interaction of Na with cleaved (011) surfaces of $CuInSe_2$. *J. Appl. Phys.*, **80**, 5039–5043.

[185] Niles, D. W., Al-Jassim, M., and Ramanathan, K. (1999) Direct observation of Na and O impurities at grain surfaces of $CuInSe_2$ thin films. *J. Vac. Sci. Technol. A*, **17**, 291–296.

[186] Gartsman, K., Chernyak, L., Lyahovitskaya, V., Cahen, D., Didik, V., Kozlovsky, V., Malkovich, R., Skoryatina, E., and Usacheva, V. (1997) Direct evidence for diffusion and electromigration of Cu in $CuInSe_2$. *J. Appl. Phys.*, **82**, 4282–4285.

[187] Taretto, K. and Rau, U. (2007) Can Grain Boundaries Improve the Performance of Cu(In,Ga)Se_2 Solar Cells? In *Thin-Film Compound Semiconductor Photovoltaics 2007,* Durose, K., Gessert, T., Heske, C., Marsillac, S., and Wada, T. (eds.), vol. 1012 of *Mat. Res. Soc. Symp. Proc.*, pp. Y09–01–1–6, MRS, Warrendale, PA.

[188] Krejci, M., Tiwari, A. N., Zogg, H., Schwander, P., Heinrich, H., and Kostorz, G. (1997) Rotational twins in heteroepitaxial $CuInSe_2$ layers on Si(111). *J. Appl. Phys.*, **81**, 6100–6106.

[189] Abou-Ras, D., Schorr, S., and Schock, H. W. (2007) Grain-size distributions and grain boundaries of chalcopyrite-type thin films. *Journal of Applied Crystallography*, **40**, 841–848.

[190] Abou-Ras, D., Caballero, R., Kavalakkatt, J., Nichterwitz, M., Unold, T., Schock, H. W., Buecheler, S., and Tiwari, A. N. (2010) Electron Backscatter Diffraction: Exploring the Microstructure in Cu(In,Ga)$(S,Se)_2$ and CdTe Thin-Film Solar Cells. In *Conference Record of the 35th IEEE Photovoltaic Specialists Conference, Honolulu, HI, U.S.A., June 20-25, 2010*, pp. 418–423, IEEE, Piscataway, NJ.

[191] Abou-Ras, D., Koch, C. T., Küstner, V., van Aken, P. A., Jahn, U., Contreras, M. A., Caballero, R., Kaufmann, C. A., Scheer, R., Unold, T., and Schock, H.-W. (2009) Grain-boundary types in chalcopyrite-type thin films and their correlations with film texture and electrical properties. *Thin Solid Films*, **517**, 2545 – 2549.

[192] Abou-Ras, D. and Pantleon, K. (2007) The impact of twinning on the local texture of chalcopyrite-type thin films. *Phys. Stat. Sol.(RRL)*, **1**, 187–189.

[193] Abou-Ras, D., Contreras, M. A., Noufi, R., and Schock, H. W. (2009) Impact of the Se evaporation rate on the microstructure and texture of Cu(In,Ga)Se_2 thin films for solar cells. *Thin Solid Films*, **517**, 2218–2221.

[194] Abou-Ras, D., Schaffer, B., Schaffer, M., Schmidt, S., Caballero, R., and Unold, T. (2012) Direct Insight into Grain Boundary Reconstruction in Polycrystalline Cu(In,Ga)Se_2 with Atomic Resolution. *Phys. Rev. Lett.*, **108**, 075502–1–5.

[195] Cojocaru-Mirédin, O. Private communication.

[196] Siebentritt, S., Sadewasser, S., Wimmer, M., Leendertz, C., Eisenbarth, T., and Lux-Steiner, M. C. (2006) Evidence for a Neutral Grain-Boundary Barrier in Chalcopyrites. *Phys. Rev. Lett.*, **97**, 146601–1–4.

[197] Hafemeister, M., Siebentritt, S., Albert, J., Lux-Steiner, M. C., and Sadewasser, S. (2010) Large Neutral Barrier at Grain Boundaries in Chalcopyrite Thin Films. *Phys. Rev. Lett.*, **104**, 196602–1–4.

[198] Nichterwitz, M., Abou-Ras, D., Sakurai, K., Bundesmann, J., Unold, T., Scheer, R., and Schock, H.-W. (2009) Influence of grain boundaries on current collection in Cu(In,Ga)Se_2 thin-film solar cells. *Thin Solid Films*, **517**, 2554–2557.

[199] Kawamura, M., Yamada, T., Suyama, N., Yamada, A., and Konagai, M. (2010) Grain Boundary Evaluation of $Cu(In_{1-x}Ga_x)Se_2$ Solar Cells. *Jpn. J. Appl. Phys.*, **49**, 062301–1–3.

[200] Yan, Y., Noufi, R., and Al-Jassim, M. M. (2006) Grain-Boundary Physics in Polycrystalline $CuInSe_2$ Revisited: Experiment and Theory. *Phys. Rev. Lett.*, **96**, 205501–.

[201] Yan, Y., Jiang, C.-S., Noufi, R., Wei, S.-H., Moutinho, H. R., and Al-Jassim, M. M. (2007) Electrically Benign Behavior of Grain Boundaries in Polycrystalline $CuInSe_2$ Films. *Phys. Rev. Lett.*, **99**, 235504–1–4.

[202] Romero, M. J., Ramanathan, K., Contreras, M. A., Al-Jassim, M. M., Noufi, R., and Sheldon, P. (2003) Cathodoluminescence of $Cu(In,Ga)Se_2$ thin films used in high-efficiency solar cells. *Appl. Phys. Lett.*, **83**, 4770–4772.

[203] Hetzer, M. J., Strzhemechny, Y. M., Gao, M., Contreras, M. A., Zunger, A., and Brillson, L. J. (2005) Direct observation of copper depletion and potential changes at copper indium gallium diselenide grain boundaries. *Appl. Phys. Lett.*, **86**, 162105–3.

[204] Hetzer, M. J., Strzhemechny, Y. M., Gao, M., Goss, S., Contreras, M. A., Zunger, A., and Brillson, L. J. (2006) On microscopic compositional and electrostatic properties of grain boundaries in polycrystalline $CuIn_{1-x}Ga_xSe_2$. *J. Vac. Sci. Techn. B*, **24**, 1739–1745.

[205] Hanna, G., Glatzel, T., Sadewasser, S., Ott, N., Strunk, H. P., Rau, U., and Werner, J. H. (2006) Texture and electronic activity of grain boundaries in $Cu(In,Ga)Se_2$ thin films. *Appl. Phys. A*, **82**, 1–7.

[206] Romero, M. J., Du, H., Teeter, G., Yan, Y., and Al-Jassim, M. M. (2011) Comparative study of the luminescence and intrinsic point defects in the kesterite Cu_2ZnSnS_4 and chalcopyrite $Cu(In,Ga)Se_2$ thin films used in photovoltaic applications. *Phys. Rev. B*, **84**, 165324.

[207] Wright, S. I. and Nowell, M. M. (2006) Image Quality Mapping. *Microsc. Microanal.*, **12**, 72–84.

[208] Mendis, B. G., Bowen, L., and Jiang, Q. Z. (2010) A contactless method for measuring the recombination velocity of an individual grain boundary in thin-film photovoltaics. *Appl. Phys. Lett.*, **97**, 092112–1–4.

[209] Kniese, R., Powalla, M., and Rau, U. (2009) Evaluation of electron beam induced current profiles of $Cu(In,Ga)Se_2$ solar cells with different Ga-contents. *Thin Solid Films*, **517**, 2357 – 2359.

[210] Metzger, W., Repins, I., Romero, M., Dippo, P., Contreras, M., Noufi, R., and Levi, D. (2009) Recombination kinetics and stability in polycrystalline $Cu(In,Ga)Se_2$ solar cells. *Thin Solid Films*, **517**, 2360 – 2364.

[211] Kniese, R. (2005) *Ladungstransport in Cu(In,Ga)Se_2-Solarzellen mit unterschiedlichen Bandlückenenergien*. Ph.D. thesis, University of Karlsruhe, Germany.

[212] Nichterwitz, M., Caballero, R., Kaufmann, C. A., Schock, H.-W., and Unold, T. (2013) Generation-dependent charge carrier transport in $Cu(In,Ga)Se_2$/CdS/ZnO thin-film solar-cells. *J. Appl. Phys.*, **113**, 044515–1–16.

[213] Donolato, C. (1989) An alternative proof of the generalized reciprocity theorem for charge collection. *J. Appl. Phys.*, **66**, 4524–4525.

[214] Everhart, T. E. and Hoff, P. H. (1971) Determination of Kilovolt Electron Energy Dissipation vs Penetration Distance in Solid Materials. *J. Appl. Phys.*, **42**, 5837–5846.

[215] Rechid, J., Kampmann, A., and Reineke-Koch, R. (2000) Characterising superstrate CIS solar cells with electron beam induced current. *Thin Solid Films*, **361**, 198–202.

[216] Nichterwitz, M. Unpublished data.

[217] Kavalakkatt, J. (2010) *Elektrische Eigenschaften von Korngrenzen in Chalkopyrithalbleitern*. Master's thesis, Technische Universität Berlin.

[218] Scheer, R. (1999) Qualitative and Quantitative Analysis of Thin Film Heterostructures by Electron Beam Induced Current. In *Polycrystalline Semiconductors V,* Werner, J., Strunk, H., and Schock, H. (eds.), vol. 67-68 of *Solid State Phenomena*, pp. 57–68, Trans Tech Publications, Switzerland.

[219] Ehrenberg, W. and Gibbson, D. (1981) *Electron bombardment induced conductivity and its applications*. Academic Press.

[220] Rincón, C., Wasim, S., and Ochoa, J. (1995) Shallow Donors, Metallic Conductivity, and Metal-Insulator Transition in n-type $CuInSe_2$. *phys. stat. sol. (a)*, **148**, 251–258.

[221] Sadewasser, S. and Visoly-Fisher, I. (2011) *Scanning Probe Microscopy on Inorganic Thin Films for Solar Cells*, chap. 11, in: D. Abou-Ras, T. Kirchartz, and U. Rau (Ed.), *Advanced Characterization Techniques for Thin-Film Solar Cells*, pp. 275–298. Wiley VCH, Weinheim.

[222] Leendertz, C., Streicher, F., Lux-Steiner, M. C., and Sadewasser, S. (2006) Evaluation of Kelvin probe force microscopy for imaging grain boundaries in chalcopyrite thin films. *Appl. Phys. Lett.*, **89**, 113120–3.

[223] Seidman, D. N. and Stiller, K. (2009) An Atom-Probe Tomography Primer. *MRS Bulletin*, **34**, 717–724.

[224] Kelly, T. F. and Larson, D. J. (2012) Atom Probe Tomography 2012. *Annu. Rev. Mater. Res.*, **42**, 1–31.

[225] Shimizu, Y., Kawamura, Y., Uematsu, M., Tomita, M., Kinno, T., Okada, N., Kato, M., Uchida, H., Takahashi, M., Ito, H., Ishikawa, H., Ohji, Y., Takamizawa, H., Nagai, Y., and Itoh, K. (2011) Depth and lateral resolution of laser-assisted atom probe microscopy of silicon revealed by isotopic heterostructures. *J. Appl. Phys.*, **109**, 036102–1–4.

[226] Cojocaru-Mirédin, O., Choi, P., Wuerz, R., and Raabe, D. (2011) Atomic-scale distribution of impurities in $CuInSe_2$-based thin-film solar cells. *Ultramicroscopy*, **111**, 552–556.

[227] Keller, J., Schlesiger, R., Riedel, I., Parisi, J., Schmitz, G., Avellan, A., and Dalibor, T. (2013) Grain boundary investigations on sulfurized Cu(In,Ga)(S,Se)$_2$ solar cells using atom probe tomography. *Sol. En. Mat. Sol. Cells*, **117**, 592 – 598.

[228] Choi, P., Cojocaru-Miredin, O., Wuerz, R., and Raabe, D. (2011) Comparative atom probe study of Cu(In,Ga)Se$_2$ thin-film solar cells deposited on soda-lime glass and mild steel substrates. *J. Appl. Phys.*, **110**, 124513–1–8.

[229] Zhang, S., Wei, S.-H., Zunger, A., and Katayama-Yoshida, H. (1998) Defect physics of the CuInSe$_2$ chalcopyrite semiconductor. *Phys. Rev. B*, **57**, 9642–9656.

[230] Knight, K. S. (1992) The crystal structures of CuInSe$_2$ and CuInTe$_2$. *Mater. Res. Bull.*, **27**, 161–167.

[231] Abrahams, S. C. and Bernstein, J. L. (1974) Piezoelectric nonlinear optic CuGaSe$_2$ and CdGeAs$_2$: Crystal structure, chalcopyrite microhardness, and sublattice distortion. *J. Chem. Phys.*, **61**, 1140–1146.

[232] Siebentritt, S. and Schuler, S. (2003) Defects and transport in the wide gap chalcopyrite CuGaSe$_2$. *J. Phys. Chem. Solids*, **64**, 1621–1626.

[233] Sadewasser, S., Glatzel, T., Schuler, S., Nishiwaki, S., Kaigawa, R., and Lux-Steiner, M. C. (2003) Kelvin probe force microscopy for the nano scale characterization of chalcopyrite solar cell materials and devices. *Thin Solid Films*, **431-432**, 257–261.

[234] Zhang, Z., Tang, X., Lemmer, U., Witte, W., Kiowski, O., Powalla, M., and Holscher, H. (2011) Analysis of untreated cross sections of Cu(In,Ga)Se$_2$ thin-film solar cells with varying Ga content using Kelvin probe force microscopy. *Appl. Phys. Lett.*, **99**, 042111–3.

[235] Lehmann, J. (2010) *Oberflächenpräparation zur Untersuchung von elektronischen Korngrenzeneigenschaften in Cu(In,Ga)Se$_2$*. Master's thesis, Freie Universität Berlin.

[236] Azulay, D., Balberg, I., Millo, O., and Abou-Ras, D. The effect of Na doping on the electronic properties of CuIn$_{1-x}$Ga$_x$Se$_2$ thin films: A local-probe study, unpublished.

[237] Datta, T., Noufi, R., and Deb, S. K. (1985) Electrical conductivity of p-type CuInSe$_2$ thin films. *Appl. Phys. Lett.*, **47**, 1102–1104.

[238] Holz, J., Karg, F., and von Philipsborn, H. (1994) The effect of substrate impurities on the electronic conductivity in CIS thin films. In *Proceedings of the 12th European Photovoltaic Solar Energy Conference, Amsterdam, The Netherlands, April 11-15, 1994,* Hill, R., Palz, W., and Helm, P. (eds.), pp. 1592–1595, Stephens & Associates, Bedford.

[239] Chakrabarti, R., Maiti, B., Chaudhuri, S., and Pal, A. (1996) Photoconductivity of Cu(In, Ga)Se$_2$ films. *Sol. Energy Mater. Sol. Cells*, **43**, 237–247.

[240] Schuler, S., Nishiwaki, S., Beckmann, J., Rega, N., Brehme, S., Siebentritt, S., and Lux-Steiner, M. C. (2002) Charge carrier transport in polycrystalline $CuGaSe_2$ thin films. In *Conference Record Of The 29th IEEE Photovoltaic Specialists Conference, New Orleans, LA, U.S.A., May 19-24, 2002*, pp. 504–507, IEEE, Piscataway, NJ.

[241] Virtuani, A., Lotter, E., Powalla, M., Rau, U., Werner, J. H., and Acciarri, M. (2006) Influence of Cu content on electronic transport and shunting behavior of $Cu(In,Ga)Se_2$ solar cells. *J. Appl. Phys.*, **99**, 014906–11.

[242] Romero, M. J., Jiang, C.-S., Noufi, R., and Al-Jassim, M. (2005) Lateral electron transport in $Cu(In,Ga)Se_2$ investigated by electro-assisted scanning tunneling microscopy. *Appl. Phys. Lett.*, **87**, 172106–3.

[243] Azulay, D., Millo, O., Balberg, I., Schock, H.-W., Visoly-Fisher, I., and Cahen, D. (2007) Current routes in polycrystalline $CuInSe_2$ and $Cu(In,Ga)Se_2$ films. *Sol. En. Mater. Sol. Cells*, **91**, 85–90.

[244] Li, W., Cohen, S. R., Gartsman, K., and Cahen, D. (2012) Ga Composition Dictates Macroscopic Photovoltaic and Nanoscopic Electrical Characteristics of $Cu(In_{1-X}Ga_X)Se_2$ Thin Films via Grain-Boundary-Type Inversion. *IEEE J. Photovolt.*, **2**, 191–195.

[245] Moenig, H., Smith, Y., Caballero, R., Kaufmann, C. A., Lauermann, I., Lux-Steiner, M. C., and Sadewasser, S. (2010) Direct Evidence for a Reduced Density of Deep Level Defects at Grain Boundaries of Cu(In, Ga)Se-2 Thin Films. *Phys. Rev. Lett.*, **105**, 116802–1–4.

[246] Azulay, D., Balberg, I., and Millo, O. (2012) Microscopic Evidence for the Modification of the Electronic Structure at Grain Boundaries of $Cu(In_{1-x}, Ga_x)Se_2$ Films. *Phys. Rev. Lett.*, **108**, 076603–1–4.

[247] Rau, U., Taretto, K., and Siebentritt, S. (2009) Grain boundaries in $Cu(In,Ga)(Se,S)_2$ thin-film solar cells. *Applied Physics A*, **96**, 221–234.

[248] Dagan, G., Abou-Elfotouh, F., Dunlavy, D. J., Matson, R. J., and Cahen, D. (1990) Defect level identification in copper indium selenide ($CuInSe_2$) from photoluminescence studies. *Chemistry of Materials*, **2**, 286–293.

[249] Dirnstorfer, I., Wagner, M., Hofmann, D. M., Lampert, M. D., Karg, F., and Meyer, B. K. (1998) Characterization of $CuIn(Ga)Se_2$ Thin Films. *phys. stat. sol. (a)*, **168**, 163–175.

[250] Chakrabarti, R., Maity, A. B., Pal, R., Bhattacharyya, D., Chaudhuri, S., and Pal, A. K. (1997) Estimation of Stress in Polycrystalline $CuInSe_2$ Films Deposited on Mo-Coated Glass Substrates. *phys. stat. sol. (a)*, **160**, 67–76.

[251] Thomas, D. (2012) *In situ Spannungs- und Strukturanalyse von Molybdän- und $CuInS_2$-Dünschichten mittels Röntgendiffraktion*. Ph.D. thesis, TU Berlin.

[252] Macherau, E. and Müller, P. (1961) Das $\sin^2\phi$-Verfahren der röntgenographischen Spannungsmessung. *Z. angew. Physik*, **13**, 305–312.

[253] Schaefer, N., Klaus, M., Genzel, C., Schuelli, T., and Abou-Ras, D. Unpublished.

[254] Wee, C., Maikop, S., and Yu, C. Y. (2005) Mobility-enhancement technologies. *Circuits and Devices Magazine, IEEE*, **21**, 21–36.

[255] Rodriguez-Alvarez, H., Mainz, R., Marsen, B., Abou-Ras, D., and Schock, H. W. (2010) Recrystallization of Cu-In-S thin films studied in situ by energy-dispersive X-ray diffraction. *J. Appl. Crystallogr.*, **43**, 1053–1061.

[256] Thomas, D., Mainz, R., Rodriguez-Alvarez, H., Marsen, B., Abou-Ras, D., Klaus, M., Genzel, C., and Schock, H. W. (2011) In-situ studies of the recrystallization process of CuInS2 thin films by energy dispersive X-ray diffraction. *Thin Solid Films*, **519**, 7193–7196.

[257] Rodriguez-Alvarez, H., Mainz, R., Caballero, R., Abou-Ras, D., Klaus, M., Gledhill, S., Weber, A., Kaufmann, C., and Schock, H.-W. (2013) Real-time study of Ga diffusion processes during the formation of Cu(In,Ga)Se_2: The role of Cu and Na content. *Sol. En. Mat. Sol. Cells*, **116**, 102–109.

[258] http : //www.helmholtz − berlin.de/forschung/oe/magma/kristallographie/projekte/virtuellesinstitut/index_en.html.